

**Momentum Images of Continuum Electrons from
the Molecular Ionization and Dissociation of H_2
Induced by Slow He^{2+} Ions**

Dissertation
zur Erlangung des Doktorgrades
der Naturwissenschaften

vorgelegt beim Fachbereich Physik
der Johann Wolfgang Goethe–Universität
in Frankfurt am Main

von
Feras Afaneh
aus
Amman (Jordanien)

Frankfurt am Main 2001

vom Fachbereich Physik der

Johann Wolfgang Goethe-Universität als Dissertation angenommen.

Dekan:

1. Gutachter:

2. Gutachter:

Datum der Disputation:

To Sawsan & Malak
To Sawsan & Malak

Zusammenfassung

Rückstoßionen-Impuls-Spektroskopie ist verwendet worden, um die Impulsverteilung von Kontinuumslektronen abzubilden, die im Stoß von langsamen He^{2+} auf He und H_2 emittiert werden. Die Impulsverteilungen wurden für voll erschlossene Bewegungen der Kerne gemessen, das heißt als eine Funktion des Stoßparameters und in einer wohl definierten Streuebene. Die einfache Ionisation (**SI**) von H_2 , die zu H_2^+ -Ionen in den nicht-dissoziativen Zuständen führt ($He^{2+} + H_2 \rightarrow He^{2+} + H_2^+ + e^-$), und die Transfer-Ionisation (**TI**) von H_2 ($He^{2+} + H_2 \rightarrow He^+ + H^+ + H^+ + e^-$), die zum Zerfall von H_2 in zwei freie Protonen führt, wurden untersucht. Ähnliche Messungen sind für He , das entsprechend atomische zwei-Elektron System, durchgeführt worden: die einfache Ionisation von He (**SI**) ($He^{2+} + He \rightarrow He^{2+} + He^+ + e^-$) und die Transfer Ionization von He (**TI**) ($He^{2+} + He \rightarrow He^+ + He^{2+} + e^-$). Diese Messungen sind durchgeführt worden, um das Verständnis der Messungen von H_2 zu verbessern. Beim Vergleich zwischen den für He und den für H_2 gemessenen Impulsverteilungen der Kontinuumslektronen wurde eine große Ähnlichkeit bemerkt.

Um die Abhängigkeit der für die TI von H_2 gemessenen Elektronen-Impulsverteilungen von der Orientierung der Molekülachse zu untersuchen, werden die Impulsverteilungen für zwei molekulare Orientierungen generiert: parallel zu der Strahlrichtung und senkrecht zu ihr. Diese Verteilungen zeigen keine Orientierungsabhängigkeit. Das deutliche Merkmal, das die Elektronen-Impulsverteilungen der in-Streuebene der **TI** von H_2 und der **TI** von He gezeigt haben, besteht in dem Erscheinen von zwei Gruppen von Elektronen, die verschiedene Strukturen haben. Außer den Sattellektronen, die in der Region zwischen Target und Projektil zwei Bananen formen, finden wir eine neue Gruppe von Elektronen, die mit einer höheren Geschwindigkeit als die Projektilgeschwindigkeit emittiert werden. Diese neuen schnellen Vorwärtselektronen entstehen im Bereich von kleinen Stossparametern und erscheinen als Abbildung des Sattels im Projektilsystem. Im Gegensatz zur **TI** von He verschwindet diese Gruppe von schnellen Vorwärtselektronen in der Impulsverteilung der **SI** von He . Anstelle dieser Gruppe erscheint ein andere neue Gruppe von Elektronen. Diese Elektronen zeigen einen Grad an Streuung in Rückwärtsrichtung. Diese Rückwärtselektronen erscheinen als Abbildung des Sattels im Targetsystem.

Die von den Sattellektronen gezeigten Strukturen sind eine Folge der quasimolekularen Natur des Stoßprozesses. Für die **TI** von H_2 , die **TI** von He und die **SI** von He , wird dabei eine π -Orbital Form der Impulsverteilung der Sattellektronen festgestellt. Das weist auf die Wichtigkeit der Rotationskopplung $2p\sigma \rightarrow 2p\pi$ in der anfänglichen Promotion des Grundzustandes hin, wo das Elektron durch weitere Promotionen ins Kontinuum gehoben wird. Sowohl die in Rückwärtsrichtung als auch die schnellen in Vorwärtsrichtung emittierten Elektronen werden nicht in der theoretischen Literatur diskutiert. Es gibt jedoch gewisse Hinweise, die auf die Existenz der Rückwärtselektronen und der schnellen Vorwärtselektronen hindeuten, die in den experimentellen Arbeiten von *Abdallah et al.* [1, 2] und in den theoretischen Rechnungen von *Sidky et al.* [3] zu finden sind. Es kann dabei vermutet werden, daß die Elektronen, die sich während des Stoßes für einige Zeit auf dem Sattel befinden,

an dem He^+ Ion im Ausgang des Stoßes steuern, das heißt entweder an dem Projektil in der Vorwärtsrichtung (wie im Fall der schnellen Vorwärtselektronen) oder an dem Target in der Rückwärtsrichtung (wie im Fall der Rückwärtselektronen). Das ist eine Folge des starken Gradienten und der damit verbundenen starken Beschleunigung am abgeschirmten He^+ -Potential.

Abstract

Cold target recoil ion momentum spectroscopy (**COLTRIM**) has been employed to image the momentum distributions of continuum electrons liberated in the impact of slow He^{2+} on He and H_2 . The distributions were measured for fully determined motion of the nuclei, that is, as a function of the impact parameter and in a well defined scattering plane. The single ionization (**SI**) of H_2 , leading to H_2^+ recoil ions in nondissociative states ($He^{2+} + H_2 \rightarrow He^{2+} + H_2^+ + e^-$) and the transfer ionization (**TI**) of H_2 leading to H_2 dissociation into two free protons ($He^{2+} + H_2 \rightarrow He^+ + H^+ + H^+ + e^-$) were investigated. Similar measurements have been carried out for He target, the corresponding atomic two-electron system, i.e. the single ionization (**SI**) ($He^{2+} + He \rightarrow He^{2+} + He^+ + e^-$) and the transfer ionization (**TI**) ($He^{2+} + He \rightarrow He^+ + He^{2+} + e^-$). These measurements have been exploited to understand the results obtained for H_2 target. In comparing the continuum electron momentum distributions for H_2 with that for He , a high degree of similarity is observed.

In the case of transfer ionization of H_2 , the electron momentum distributions generated for parallel and perpendicular molecular orientations revealed no orientation dependence. The in-scattering plane electron momentum distributions for the transfer ionization of H_2 by He^{2+} and for the transfer ionization of He by He^{2+} showed that the salient feature of these distributions for both collisions systems consists in the appearance of two groups of electrons with different structures. In addition to the group of the saddle electrons forming two jets separated by a valley along the projectile axis, we find a new group of electrons moving with a velocity higher than the projectile velocity. These new fast forward electrons result from a narrow range of impact parameters and appear as image saddle in the projectile frame. In contrast to the transfer ionization of He, the fast forward electrons group disappears in the in-scattering plane electron momentum distribution generated for the single ionization of He . Instead of this group, another new group of electrons appear. These electrons exhibit an amount of backscattering. These backward electrons appear as image saddle in the target frame.

The structures that the saddle electrons show are owing to the quasi-molecular nature of the collision process. For the **TI** of H_2 , the **TI** of He and the **SI** of He , a π -orbital shape of the electron momentum distribution is observed. This indicates the importance of the rotational coupling $2p\sigma \rightarrow 2p\pi$ in the initial promotion of the ground state followed by further promotions to the continuum. The backward electrons as well as the fast forward electrons are not discussed in the theoretical literature at all. However, a number of obvious indications of the existence of the backward and fast forward electrons could be seen in the experimental works of *Abdallah et al.* [1, 2] as well as in the theoretical calculations of *Sidky et al.* [3]. One might speculate that electrons which are promoted on the saddle for some time during the collision could finally swing around the He^+ ion in the way out of the collision, i.e., either around the projectile in the forward direction as in the **TI** case forming the fast forward electrons or around the recoil ion in the backward direction as in the **SI** case forming the backward electrons. This might be a result of the strong gradient, and hence the large acceleration of the screened He^+ potential.

Contents

Zusammenfassung	III
Abstract	V
1 Introduction	1
1.1 Ion-Atom Collisions	1
1.2 Ion-Molecule Collisions	4
1.3 Experimental Technique	6
1.4 Motivations of this Work	8
2 Theoretical Approaches	9
2.1 Kinematics of the inelastic ion-atom collision processes	9
2.1.1 Capture Process	12
2.1.2 Ionisation Process	13
2.2 Theory of slow ion-atomic collisions	14
2.2.1 Classical-Trajectory Monte Carlo Method	14
2.2.2 The Quasi-Molecular Model: Diabatic Verses Adiabatic	16
2.2.3 Dynamical Coupling Terms	18
2.2.4 Molecular Orbital Approximation	19
2.2.5 Hidden Crossings Theory	22
2.2.6 Direct Solutions of the Time Dependent Schrödinger Equation On a Grid	28
2.3 Basic Concepts in the Ion-Molecule Collisions	30
2.3.1 Fragmentation Process: Coulomb-Explosion Model	30
2.3.2 Frank Condon Principle	30
2.3.3 Energy Distribution of the emitted Fragments: Reflection method	32

2.3.4	Angular Distributions of the emitted Fragments: Axial-Recoil Approximation	34
2.4	Theoretical Models of the Slow Ion-Molecule Collisions	35
2.4.1	Modified Molecular-Orbital-Expansion Method	35
2.4.2	Orientation-Dependent Atomic-orbital Expansion	35
2.4.3	<i>CTMC</i> Model	37
2.5	Zero-Ranged Potential Model (<i>ZRP</i> -Model)	40
3	Experimental Setup	44
3.1	ECR beam line	44
3.2	Target	46
3.2.1	Supersonic Gas Jet	46
3.3	Reaction Microscope: Momentum spectrometer	48
3.3.1	RIM spectrometer	48
3.3.2	Electron spectrometer	50
3.4	Position Sensitive Dectectors	51
3.5	Multi-Hit System	54
3.5.1	Multi-Hit-line-Anode	54
3.5.2	Multi-hit-TDC (Lecroy TDC 3377)	55
3.6	Signal Processing and Data Acquisition System	55
4	Data Analysis	59
4.1	calibration Of RI-spectrometer	59
4.2	Calibration Of The Electron Spectrometer	63
4.3	Experimental Resolution of Multi-Hit-System	64
5	Results and Discussion	68
5.1	Data Presentation	68
5.1.1	${}_3He^{2+}$ - H_2 Collision System	68
5.1.2	Dissociative Ionization of H_2 (Fragmentation Process)	68
5.1.3	Single Ionization of H_2	80
5.1.4	${}_3He^{2+}$ - He Collision System	85
5.2	Discussion and Interpretation	96
5.2.1	Saddle-point electrons	96
5.2.2	Fast Forward Electrons and Backward Electrons	98

6 Concluding Remarks

102

A Multi-Hit Lecroy 3377 TDC

104

Bibliography

106

Chapter 1

Introduction

1.1 Ion-Atom Collisions

In atomic collisions, ionization and other inelastic processes provide, from the theoretical point of view, a suitable testing ground to describe the fundamental problem of the evolution of a time-dependent multi-particle system. In addition, comprehending these processes is significant for variety of pure and applied fields of research such as astrophysics and stellar structure and evolution [4], plasma physics and thermonuclear fusion [5, 6], and the study of surfaces and materials [7, 8, 9].

It is known that in slow collisions for which the projectile velocity v_p is much smaller than the classical electron orbital velocity v_o , molecular effects play a major role in inelastic collision. In this low velocity regime, an electron is shared temporarily by the target and the projectile nuclei. In consequence, a transient quasi-molecular ion is formed [10]. This picture holds true even for large projectile velocities when inner-shell electrons are the active ones, as was suggested by Fano and Lichten [11], provided that $v_p \ll v_o$ still holds. In this model, as the internuclear separation decreases, electrons are promoted to states of higher energy and eventually into the continuum along a series of transitions between molecular orbitals (MOs). This model was successfully used in illustrating the L inner-shell vacancy formation in collision of Ar^+ with Ar [12] in addition to various other cases. Although in most of the studies, the molecular promotion model has been developed in order to interpret the processes of excitation and charge exchange [13, 14, 15, 16, 17, 18], several authors [17, 19] suggested that this model can be used in treating ionization at slow collision velocities as well.

When v_p becomes comparable to v_o , the nature of the process of ionization is expected to be less molecular. The two Coulomb centers are to be included in any treatment of what is referred to as the two-center effect [20, 21, 22, 23, 24]. Performing classical-trajectory Monte Carlo calculations (CTMC) on $p+H(1s)$ collisions with impact energies from 25 to 200 keV, Olson [25] observed that a large fraction of the forward emitted electrons had velocities approximately equal to half the velocity of the projectile. In a classical description, these electrons will be electrons that were left "standard" at the point where they feel equal and

opposite forces from the projectile and the target core ions. While the two Coulomb centers are receding from each other, those electrons will be pushed to higher energies on the rising potential of the saddle point. Eventually this process will leave the electrons riding the "saddle" in the continuum, when the two Coulomb centers become infinitely separated. Olson [26] and Olson et al. [27] studied in more detail those electrons within the CTMC framework and referred to them as $v_p/2$ electrons. This mechanism found support from coupled channel calculations by Winter and Lin [28]. They found that the inclusion of a third center at the equiforce point in their close-coupling calculations resulted in a large improvement in the calculated cross section compared to early experimental results by Fite et al. [29]. However, Winter and Lin's calculations were performed at relatively smaller impact energies compared to the CTMC calculations by Olson and coworkers.

More recently the "saddle point" process received an alternative formulation in terms of the hidden crossing theory [30, 31, 32, 33, 34]. In this theory two major mechanisms leading to ionization are identified, the T and the S processes. In both processes the electrons are promoted to the continuum via successive hidden crossings of the quasi-molecular states formed during the collision. The term "hidden" was used since those crossings occur in the complex plane of the internuclear axis. In the T process, the electrons are promoted to the continuum while the two Coulomb centers are receding from each other; this process is the quantum mechanical analog of the classical "saddle point" ionization mechanism. In the S process, on the other hand, ionization occurs as the two nuclei approach each other at small inter-nuclear distances, where the target electron can be diabatically promoted into the continuum through a series of hidden crossings. A classical description of the process might be that, as the two nuclei closely approach each other, a centrifugal barrier is formed between them forbidding the electron from existing between the two nuclei. Consequently, an electron may be pushed into the continuum while the target and the projectile are on their way to becoming a united atom (the point at which the barrier rises to infinity) [35]. Theoretical results of Ovchinnikov and Macek for proton impact on H with a velocity of 0.4 a.u. show that S-type electrons are peaked in momentum space at both the target and projectile. Since a considerable amount of theoretical support for the T process was provided by adiabatic calculations, which are expected to apply at much lower projectile velocities than those of most previous experimental investigations, Pieksma et al. [36] investigated the velocity distributions of the electrons ejected from the collision system p-H in the projectile energy range 1-6keV, where adiabatic theories do apply. Their data exhibit a clear dominance of the saddle-point ionization mechanism for energies ranging from 4 to 6keV.

Till 1995, the experimental search for evidence for "saddle-point" electrons lead to ambiguous results. Olson et al. [27] reported on p-He collisions experiments within a projectile energy range of 60-200 keV. They observed a broad peak in the electron velocity spectrum at an angle of 17° which was regarded as an evidence for the existence of a saddle point ionization mechanism. Most of the experiments that followed focused on studying this peak. However, most of the measurements were at angles larger than 0° in order to avoid the pronounced cusp of the *ECC* in the

forward direction. Irby et al. [37] studied the two collision systems $H^+ + He$ and $He^{2+} + He$ at energies of 60-120 keV/u. They reported an electron momentum spectra that have a peak which shifts with changing projectile velocity and charge state according to eq. 5.3. Later, the same group [38] reported similar results for the collisions of C^{q+} (where $q = 1, 2, 3$) with He and Ne at energies 83, 100 and 150 keV/u. In an independent work, Gay et al. [39] showed a similar behavior. On the other hand, Bernardi et al. [40, 41] and Meckbach et al. [42] showed that the observed peak did not shift according to eq. 5.3 and was just the remnant of the cusp at larger angles. DuBois [43] also did not see this shift in the peak in his experimental data for the collisions H^+ and He^{2+} with He in a similar energy range. He concluded that any confirmation of the existence of the saddle-point ionization mechanism based on shifts observed by Irby et al. [37, 38] and Gay et al. [39] was problematic. In a later paper [44] he measured the double differential cross section in the collision $C^{q+} + He$ at impact energies of 100 and 150keV/u, where the projectile charge $q = 0- 4$. Again his data did not support the suggested saddle point ionization mechanism.

The entire field of ionization at low to intermediate projectile velocities and the discussion of the saddle-point ionization mechanism has been profoundly changed over the last few years through momentum imaging techniques which produce complete pictures of the momentum spectra. Kravis and coworkers [45] obtained two-dimensional images of the longitudinal and transverse velocity of the continuum electrons for a wide range of impact velocities of p and C^{6+} . They did not determine the impact parameter. Only for proton impact below 1 a.u. they found most electrons in the saddle electrons. A major advance came from the work of Dörner et al. [46] who used cold target recoil- ion momentum spectroscopy (*COLTRIMS*) [47, 48] to obtain a much more detailed, highly differential image of the velocity distributions of electrons emitted in collisions of protons with He at projectile velocities of 0.45, 0.46, and 0.78 a.u.. By measuring the three components of the target recoil-ion momentum, in addition to two velocity components of the ejected electron, they were able to determine electron velocity distributions for well-defined scattering planes and impact-parameter windows. They observed that electrons were ejected preferentially within the scattering plane and into the forward direction. These forward electrons were emitted in two jets oriented in the scattering plane and off the projectile axis. These features were interpreted by Ovchinnikov et al. [31] and Macek et al. [49]. They showed that only the first transition in the series of hidden crossings changes the angular momentum electronic state. This angular momentum character is then revealed in the form of the continuum velocity distribution. Orbitals of various character have been implied by distributions such as those observed by Dörner et al.. Utilizing a similar *COLTRIMS* setup used by Dörner et al. [46], Abdallah and Coworkers have investigated additional systems of $He^{+,2+}$ incident on He , Ne^+-Ne , He^+-Ne and Ne^+-He at projectile velocities ranging from 0.25 to 1.23 a.u. [50, 1, 2]. These studies have demonstrated that each collision system produces its distinct electron velocity distribution. Very recently, in our group, Schmidt has succeeded in measuring the complete momentum vector of ejected electrons for $He^{2+}-He$ collision system by measuring the time-of-flight of the emitted electrons [51].

1.2 Ion-Molecule Collisions

In comparison to ion-atom collisions, the study of ion-molecule collisions poses an extra challenge since the molecular nature of the target has to be taken in consideration. Slow collisions between highly charged ions and molecules are a probe of both, the electronic processes involved during the collision and the dynamics of the molecular fragmentation after the collision. Particular attention has been concentrated on H_2 molecules [52, 53, 54, 55] due to the relative simplicity of their electronic structure [56, 57]. Although molecular fragmentation processes have been studied for years, recent advances in experimental and theoretical techniques have shed new light on the subject. Historically, experimental investigations of molecular fragmentation were conducted by colliding a variety of projectiles, which include electrons [58, 59], singly [60, 61] and multiply charged ions [62, 63, 64, 65, 66], and photons [67] with the target. Measurements of cross sections, yields, and energy distributions done through these experiments revealed the structure of molecules, how energy is transferred from the incoming projectile to the molecule, and how energy is distributed among molecular states. These data were interpreted in terms of Franck-Condon transitions between states of the isolated molecule.

In the past decade, distinguished experimental and theoretical efforts have been devoted to studies of possible molecular orientation effects in ion-molecule collisions. Starting with the pioneering work by Taun and Gerjuoy [68], several theoretical studies have examined the influence of the molecular axis alignment on the electron capture to the projectile ion and on the associated processes of transfer ionization and transfer excitation [69]. For these processes, the alignment dependence has been interpreted as an interference effect in electron capture from the two centers of the molecule. When the diatomic molecule is oriented perpendicular to the beam there is no phase difference between the amplitudes describing the capture from the two centers, resulting in constructive interference for a gerade target wavefunction and a destructive interference for a ungerade target wavefunction. When the angle between the inter-atomic axis and the beam decreases, the phase difference increases and the interference changes. Therefore, if charge transfer contributes significantly to the ionization, one can expect for certain projectile velocities predominant ionization of molecules oriented perpendicular to the beam. As was theoretically predicted, a strong alignment effect was later verified experimentally in O^{8+} transfer ionization collisions with D_2 [70, 62]. However, in this experiment as well as in proton collisions with H_2 [71, 72], no alignment dependence was revealed in double ionization and ionization-excitation. This result was supported by calculations in the first Born approximation [73] which showed that pure ionization of H_2 by proton impact shows relatively little (typically 20%) alignment dependence.

The use of Coltrims technique has helped in accomplishing recent progress in the investigation of ion-molecule collision. It is evident that coincident measurements with a position- and time-sensitive multi-particle detector provide a complete three-dimensional image of the breakup process for each individual event. In the simplest case of diatomic molecules, this implies that the dissociation of highly ionized molecular ions can be examined for a definite orientation of the interatomic axis. Dörner

et al. [74] has utilized the Coltrims technique to measure the direction and energy of the two ionic fragments in coincidence with the momentum vector of one of the two electrons from D_2 double ionization by linear polarized photons. This work has provided, for the first time, the connection between the ionic and the electronic motion in the continuum.

In contrast to the several theoretical calculations in ion-atom collisions, rigorous theoretical models in ion-molecule collisions are very rare, particularly in the low- and intermediate-energy region. Some may argue that the theoretical models developed for ion-atom collisions, such as the atomic-orbital (AO) and the molecular orbital (MO) expansion models, can be generalized straightforwardly to study ion-molecule collisions. However, in reality this has not been done except for the exploratory calculations of Kimura [75, 76] using the MO expansion for H^+ and Ar^+ on H_2 . Computational complexities are the main reason behind the lack of calculations. On the one hand, one has to treat the two-center or many-center target molecular wave functions, which enlarge the calculations of basis functions required for an AO- or MO-based calculations. On the other hand, the effects of different molecular orientations on the electron-capture cross sections should be taken into account. Calculations of electron-capture cross sections for ion-molecule collisions under various approximations have been carried out by few authors. In the keV/amu energy region, models [77, 78] based on the AO-expansion method have been employed. However, as drastic approximation were adopted in the evaluation of matrix elements, the results are either in poor [77] or in only qualitative agreement [78] with the experimental data. In this energy region, Kimura [75] carried out the most elaborate calculations for $H^+ + H_2$ collisions in the energy range 0.2-20 keV. A semiclassical close-coupling model with an expansion in molecular states was used. The two lowest potential-energy surfaces of the H_3^+ ion for different orientation of the H_2 molecular with respect to the incident beam were calculated using the so-called diatomic-in-molecules (DIM) method [79, 80]. This method resembles the linear combination of atomic orbitals (LCAO) for diatomic systems and is helpful when treating H_3^+ as a composite system of either $H^+ + H_2$ or $H + H_2^+$. The electron-capture cross section was then obtained by solving the two-state coupled equations. His calculations open the door to study the effect of molecular orientation. Besides, they are the first to provide trustworthy theoretical results for ion-molecule collisions. At high collision energies, charge transfer in $H^+ + H_2$ was investigated by Taun and Gerjuoy [68] depending on the Brinkman and Kramers (BK) approximation [81] to calculate the total single-electron-capture cross section for $H^+ + H_2$. They also studied the ratio of the capture cross section from H_2 to that from H as a function of collision energies and deduced that, in general, the hydrogen molecule cannot be considered as made of two independent hydrogen atoms as far as the collision cross sections are considered. Deb et al. [82] reexamined the model of Taun and Gerjouy and calculated the differential cross section for a fixed molecular orientation. They found pronounced oscillations in the angular distributions for each fixed molecular orientation, which can be attributed to the interference of the scattering amplitudes from the two atomic centers. Similar calculations based on a different version of the Born approximation were carried out

by Band [83], Ray and Saha [84]. Other calculations on H_2 employed the classical trajectory Monte Carlo with independent electrons to study state-selective electron capture and ionization [85, 86]. Moreover, the continuum distorted wave model has been applied to $O^{8+}+H_2$ transfer ionization collisions to explain the cross section dependence on the alignment of the molecular axis [62]. Very recently, a five-body classical trajectory Monte Carlo (CTMC) model has been developed to predict the electronic and nuclear dynamics for double electron removal by highly charged ion impact [57].

1.3 Experimental Technique

Recoil- Ion Momentum Spectroscopy (RIMS) has been developed to provide an efficient and precise experimental tool to explore the correlated dynamics of collision induced atomic many-particle reactions by measuring the momenta (and thus angle and energy) of all involved particles in coincidence. In early measurements [87, 88], the recoiling target ion momentum has not, in the practical sense, been experimentally accessed for quite a long time because of the extremely small energies transferred to the target nucleus during most of the atomic reactions for charged particle or photon impact [89]. Because the mass of the nucleus is large compared to the mass of the electron, recoil energies E_R are typically well below 1 eV ranging into the μ eV and even sub- μ eV regime for a majority of atomic reactions. First attempts to measure angles and momenta of slow recoil ions were already reported in the seventies [89, 90, 91]. In the late 80's few groups succeeded in detecting such ions and obtained information on their mean energies [92, 93, 94]. Ullrich and Schmidt-Böcking in Frankfurt were the pioneers in actually measuring the recoil-ion momenta [95, 96, 97]. They used a static room temperature gas target, time-of-flight measurement in a field-free drift tube and magnetic ion charge state selection. This allowed to the measurement of the transverse recoil ion momentum with a solid angle of a few percent. The resolution was limited by the thermal motion of the target at 300K ($\Delta E \approx 40$ meV). Later, this momentum resolution was improved using a static 30 K gas ($\Delta E \approx 4$ meV) [98, 99]. Considerable advance was achieved by carrying localised gas-jet targets in connection with ion-projection techniques into effect. The recoil-ions created in the overlap volume between the localised gas target and the ion beam were extracted by an electrostatic field and projected onto position sensitive detectors [100, 101, 102, 103]. The measured times-of-flight and the impact positions of the ions on the detector will be utilized to reconstruct the ion trajectories and calculate their complete initial momentum vectors. By this technique, Fronhe et al. and Ali et al. [100, 101] measured recoil ion momenta using an effusive gas jet target. They used a multi-capillary array to direct the flow of the gas. At the same time, the gas jet was cooled through the collimation of the gas flow in the channels of the capillary array. This effective cooling of the gas jet helped to improve the momentum resolution. This technique was employed to measure the recoil ion momenta for Ne gas target [102]. The momentum resolution achieved in this study was about 6 a.u. in the direction transverse to the jet and 8-10 a.u. in the longitudinal direction. This resolution was comparable with the resolution obtained for Ne using

the cooled gas cell [104, 105]. This technique offered, for the first time, the ability to detect the recoil ions with a solid angle of nearly 100%. An important breakthrough in the momentum resolution was accomplished by the use of supersonic atomic jets ($\Delta E < 1$ meV) [103, 106]. Finally, the combination of the precooling with supersonic expansion yielded a further increase in momentum resolution and pushed it to $\Delta E_R \approx \pm 30 \mu\text{eV}$ for Helium ions. Therefore, the technique was referred to as **Cold Target Recoil Ion Momentum Spectroscopy: COLTRIMS** [107, 108, 47]. Recently, applying focusing geometry and electrostatic extraction fields, the development culminated in a superior resolution of $\Delta E_R \approx \pm 1.2 \mu\text{eV}$ for He^{1+} ions with a solid angle of 4π for the detection of momenta below 5 a.u. [109, 110, 111]. Thus, these spectrometers made it potential, for the first time, to measure the complete momentum vector of one reaction product, the target ion, emerging from an atomic collision with a resolution of a few percent and a solid angle of nearly 100% of 4π . Experiments became feasible where contributions of the projectile ionization to the electron- nucleus or electron- electron interactions were kinematically separated [112, 113]. State- selective scattering angle dependent studies of single and double electron capture into different shells of the projectile at medium velocities were performed [108, 109, 110, 113, 114, 115, 116]. "Transfer ionization" in proton-helium collisions (one helium electron is captured by the projectile the other one is emitted) was investigated in kinematically complete experiments [110]. Furthermore, the contributions of photoabsorption and Compton scattering to He double ionization at high photon energies became separable [117, 118].

The latest substantial improvement in fast progress was marked by merging such *COLTRIMS* spectrometers with novel electron projection spectrometers. These electron imaging systems employ the fundamental principle of *COLTRIMS* to the electrons. For very low electron energies (typically $< 5\text{eV}$), the same electric field which projects the positive ions onto one detector guides the negative electrons towards another detector [46, 45, 50, 1, 2]. However, the electron detector needs to be placed close to the interaction volume to provide a solid angle close to 4π . Also to guide electrons with higher momenta transverse to the electric field, Moshhammer and coworkers introduced electron imaging with a homogenous magnetic field superimposed parallel to the electric extraction field. The magnetic field forces the electrons on spiral trajectories and thus prevents them from leaving the spectrometer. This novel electron analyzer extends the projection technique for electron towards much higher electron energies [48, 111]. A resolution for electrons of ± 5 meV at zero energy and full solid angle up to 300 eV has been achieved [48]. These projection spectrometers can be equipped with fast delaying detectors, capable of handling multiple hits. Thus, all electrons from multi- electron reactions can be analyzed simultaneously [119]. Merging a high resolution recoil ion with such a multi- electron projection spectrometer creates an extremely versatile and powerful tool for atomic and molecular collision physics. In pioneering experiments for multiple ionization by fast ion impact, more than two electrons have been detected together with the recoil ion momentum [120]. A great amount of coincident 3-dimensional momentum space imaging studies have been performed in the last decade. They include electron impact ionization of atoms [121, 122], single photon double ionization of

atoms from threshold [123, 124, 125, 126, 127, 128] to 100 keV [118, 129] and ion impact on atoms from keV protons [46] to GeV/u U^{92+} [130] projectiles, capture and transfer reactions [108, 131], and single photon double ionization of fixed in space molecules [74]. An overview can be found in [132]

1.4 Motivations of this Work

In this thesis, we present an experimental study of 15 and 25keV $p - H_2$ and ${}_3He^{2+} - H_2$ collisions, which, for the first time, gives two-dimensional images of the square of the final state of electron wave function in velocity space with simultaneous determination of the nuclear motion and the scattering angles of the projectile (the impact parameter). We have employed the *COLTRIMS* technique to determine the three-dimensional momentum vector of both fragments in coincidence with two momentum components of the emitted electron and with scattering angles of the projectile as well.

Because of their large cross sections for electron capture, multi-charged ions are effective sources of dissociative ionizations. We have used such slow multi-charged ions as projectiles to induce fragmentation of H_2 molecules. The ionization and dissociation processes associated with one electron capture can be described as two independent sub-processes. The first one is the electronic transition in which one electron is captured and simultaneously the other is emitted while the nuclei can be assumed to stay fixed (axial recoil approximation). The second is the dissociation of the leftover molecular ion caused by the Coulomb repulsion of the nuclei. In most of the previous studies on the ion-molecule collisions, the researchers have used position-sensitive multi-hit-detectors and projection spectrometers to measure the fragmentation pattern from this second step of molecular fragmentation. Hence, in this work, we have tried, for the first time, to relate the two sub-processes, i.e., the ejection of the electrons(s) and the molecular fragmentation.

When the molecular ion dissociates, it does so in a time span which is very small compared to rotational times. This is the basis of the axial-recoil approximation [133] which states that the H^+ fragment ions travel along the line of the internuclear axis at the time of the excitation of the dissociative state. Therefore, the ion direction can be taken as indication for the orientation of the molecule at the instant of the electronic excitation. Depending on the validity of axial-recoil approximation and using our measurements, we introduce the first concrete experimental study of the effect of the molecular orientation on velocity distributions of the emitted electron.

We carried out the same measurements for Helium, the corresponding atomic two-electron system, using the same experimental setup and following the same procedures. These results are used so as to improve our understanding of the results for H_2 .

Chapter 2

Theoretical Approaches

2.1 Kinematics of the inelastic ion-atom collision processes

For the overwhelming part of all atomic reactions in ion-atom collisions only a little momentum, energy and mass compared to the initial momentum P_p , energy (E_p) and mass (M_p) of the incoming projectile is transferred during the encounter. This is true even for small projectile masses as well as for comparably violent collisions where the target atom is multiply ionised in an encounter with a highly charged ion. Under these conditions the longitudinal and transverse momentum balances are decoupled. They contain different information on the collision and can be calculated separately on the basis of the non-relativistic energy and momentum conservation. In the collision process, the projectile and its electrons (as far as it possesses electrons) interact with the target atom through Coulomb interaction. This interaction can induce one or more from the following processes:

1. n_T target electrons can be emitted to the continuum.
2. n_p projectile electrons can be emitted to the continuum.
3. n_c electrons can be transferred from target to projectile bound states.
4. n_T^* target electrons can be excited.
5. n_p^* projectile electrons can be excited.

Out of 3 degrees of freedom for the projectile and 3 for the target in the initial state and by neglecting the spin of the electrons, the system has $6+3(n_T + n_p)$ degrees of freedom in the final state.

The initial conditions of the collision partners in the lab-system can be defined from the preparation of the supersonic jet target of velocity V_{jet} in the y-direction and the projectile of velocity V_p in the z-direction as follows

$$\vec{p}_{\mathbf{P}}^i = \begin{pmatrix} 0 \\ 0 \\ m_p V_P \end{pmatrix} \quad (2.1)$$

and

$$\vec{p}_{\mathbf{R}}^i = \begin{pmatrix} 0 \\ m_R^i V_{jet} \\ 0 \end{pmatrix} \quad (2.2)$$

where m_R and \vec{p}_R^i are the mass and momentum of the target before the collision; and m_P and \vec{p}_P^i are the mass and momentum of the projectile before the collision.

In general, the energy and momentum of the collision system are conserved and given in the following equations

$$\vec{p}_R^i + \vec{p}_P^i = \vec{p}_R^f + \vec{p}_P^f + \sum_{j=1}^N \vec{p}_{e_j}^f \quad (2.3)$$

and

$$\sum_{j=1}^N \varepsilon_j^i + E_R^i + E_P^i = E_R^f + E_P^f + \sum_{j=1}^N (E_{e_j}^f + \varepsilon_j^f) \quad (2.4)$$

where p_P^f and p_R^f are the momentum vectors of projectile and recoil ion after the collision. E_P^i and E_R^i are the energy of projectile and target before the collision and E_P^f and E_R^f are after the collision. $E_{e_j}^f$ and $p_{e_j}^f$ are the continuum energy and final momentum of the j-th electron. ε_j is the binding energy of the j-th electron. N is the total number of the target and projectile electrons.

In the lab system, the kinetic energy of the target before the collision can be neglected compared to the initial kinetic energy of the projectile, i.e.,

$$E_R^i \approx 0 \quad \text{for} \quad \frac{m_R^i}{2} V_{jet}^2 \ll E_P^i \quad (2.5)$$

and because of the high collision energy and the small momentum transfer the kinetic energy of the recoil ion after the collision can be neglected too:

$$E_R^f \approx 0 \quad (2.6)$$

The kinetic energy of the projectile is given by

$$E_P^f = \frac{1}{2m_p^f} (p_{xp}^f{}^2 + p_{yp}^f{}^2 + p_{zp}^f{}^2). \quad (2.7)$$

if the momentum transfer is small compared to the initial momentum of the projectile, i.e., $p_{xp}^f{}^2 + p_{yp}^f{}^2 \ll p_{zp}^f{}^2$, equation 2.7 can be approximated

$$E_P^f \approx \frac{p_{zp}^f{}^2}{2m_p^f}. \quad (2.8)$$

and therefore the longitudinal momentum is given by

$$p_{zp}^f \approx \sqrt{2m_p^f E_p^f}. \quad (2.9)$$

by substituting 2.5 and 2.6 in 2.4, we obtain

$$E_p^i = E_p^f + \sum_{j=1}^{n_T+n_p} E_{ej}^f + \sum_{j=1}^N (\varepsilon_j^f - \varepsilon_j^i) \quad (2.10)$$

where $\sum_{j=1}^N (\varepsilon_j^f - \varepsilon_j^i)$ is the energy difference between initial and final bound electronic states and can be identified as the Q-value of the reaction, i.e.,

$$Q = \sum_{j=1}^N (\varepsilon_j^f - \varepsilon_j^i) \quad (2.11)$$

substituting 2.10 and 2.11 in 2.9, we get

$$p_{zp}^f = \sqrt{2m_p^f (E_p^f - Q - \sum_{j=1}^{n_T+n_p} E_{ej}^f)} \quad (2.12)$$

Since n_c target electrons are transferred to the projectile and n_p projectile electrons are emitted to the continuum, the projectile mass will change after the collision. The final mass of the projectile is then given by

$$m_p^f = m_p^i + (n_c - n_p) m_e \quad (2.13)$$

substitute m_p^f in 2.12, we get

$$p_{zp}^f = \sqrt{2m_p^i E_p^i \left(1 + \frac{(n_c - n_p) m_e}{m_p^i}\right) \left(1 - \frac{Q + \sum_{j=1}^{n_T+n_p} E_{ej}^f}{E_p^i}\right)} \quad (2.14)$$

after expanding the square root of $n_c - n_p / m_p^i$ ($m_e = 1 \text{ a.u.}$) and $(Q + \sum_{j=1}^{n_T+n_p} E_{ej}^f) / E_p^i$, we obtain after neglecting all quadratic terms

$$p_{zp}^f = p_{zp}^i \left[\frac{1}{2} \left(\frac{n_c - n_p}{m_p^i} - \frac{Q + \sum_{j=1}^{n_T+n_p} E_{ej}^f}{E_p^i} \right) + 1 \right] \text{ for } \frac{1}{m_p}, \frac{\Delta E_p}{E_p^i} \ll 1 \quad (2.15)$$

As known from the initial conditions that $p_{zp}^i = v_p m_p^i$ and using 2.14, the change in the longitudinal momentum of the projectile

$$\Delta p_{zp}^f = p_{zp}^f - p_{zp}^i = \frac{n_c - n_p}{2} v_p - \frac{1}{v_p} \left(Q + \sum_{j=1}^{n_T+n_p} E_{ej}^f \right) \quad (2.16)$$

From the momentum conservation law, the longitudinal momentum of the recoil ion after the collision is given by

$$p_{zR}^f = p_{zp}^i - p_{zp}^f - \sum_{j=1}^{n_T+n_p} p_{zej}^f \quad (2.17)$$

A combination of 2.16 and 2.17 results in:

$$p_{zR}^f = \frac{n_p - n_c}{2} v_p + \frac{Q}{v_p} + \sum_{j=1}^{n_T+n_p} \left(\frac{E_{ej}^f}{v_p} - p_{zej}^f \right) \quad (2.18)$$

up to equation 2.16, all energies and momenta were given in lab-system. The n_p emitted electrons can be observed in the projectile system, because these electrons belong originally to the projectile. Using the transformation $p_{zej}^f \sum^{lab} = v_p + p_{zej}^f \sum^p$, man can exchange between lab- and projectile systems. Upon 2.18 a new term ξ_j can be defined as follows

$$\xi_j = \frac{E_{ej}^f \sum_i^{ab}}{v_p} - p_{zej}^f \sum_i^{ab} = \frac{p_{zej}^f \sum_i^{ab}}{v_p} - p_{zej}^f \sum_i^{ab} \quad (2.19)$$

when ξ_j is transformed to the projectile system, we get

$$\xi_j = \frac{v_p + p_{zej}^f \sum_i^{ab}}{2v_p} - v_p - p_{zej}^f \sum_p = \frac{E_{ej}^f \sum_p}{v_p} - \frac{v_p}{2} \quad (2.20)$$

By summing over all projectile electrons, we get

$$\sum_{j=1}^{n_p} \xi_j = -n_p \frac{v_p}{2} + \sum_{j=1}^{n_p} \frac{E_{ej}^f \sum_p}{v_p} \quad (2.21)$$

Substituting 2.21 in 2.18, we obtain the final longitudinal momentum of the recoil ion

$$p_{zR}^f = -\frac{Q}{v_p} - n_c \frac{v_p}{2} + \sum_{j=1}^{n_T} \left(\frac{E_{ej}^f}{v_p} - p_{zej}^f \right) \sum_i^{ab} + \sum_{j=1}^{n_p} \left(\frac{E_{ej}^f}{v_p} \right) \sum_p \quad (2.22)$$

This is a general equation which includes all possible ionisation processes. This equation can be simplified if the reaction channel is singled out.

2.1.1 Capture Process

In this process, electrons (n_c) are transferred from the target to the projectile. For pure electron capture, only discrete values of p_{zR}^f occur corresponding to the energy

eigenvalues of the projectile and target electrons. Therefore, equation 2.22 can be simplified to

$$p_{zR}^f = -\frac{Q}{v_p} - n_c \frac{v_p}{2} \quad (2.23)$$

The measurements of the capture reactions are used to calibrate the spectrometer and to determine the momentum resolution. In our experiment, the Q-values of the single and double capture of He (1^1S_0) by He^{2+} are measured at different projectile energies using different electric extraction fields. The results are employed to determine the calibration factors and the momentum resolution. For the single capture (SC), $He^{2+} + He \rightarrow He^+ + He^+$, the Q-value can be calculated from the following equation

$$Q_{SC(m,n)} = -79eV - (-13.6eV)\left(\frac{4}{n_1^2} - \frac{4}{n_2^2}\right) \quad (2.24)$$

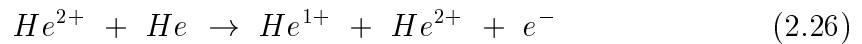
thereby, 79eV is the double ionisation threshold of He in the ground state. n_1 and n_2 describe the principle quantum numbers of both electrons. For the SC in the ground state ($n_1 = n_2 = 1$), man obtain $Q=29.8eV$ [134]. By the Double capture of helium (DC) $He^{2+} + He \rightarrow He + He^{2+}$, both electrons are bound in a neutral He atom before and after the collision. Therefore, $Q_{DC(1^1S_0)} = 0eV$ is valid by a DC in the ground state.

2.1.2 Ionisation Process

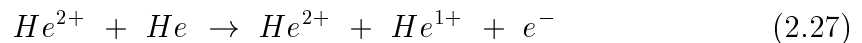
For the emission target electrons to continuum states, we obtain

$$p_{zR}^f = -\frac{Q}{v_p} - \sum_{j=1}^{n_T} \left(\frac{E_{ej}^f}{v_p} - p_{zej}^f\right) \Sigma^{lab} \quad (2.25)$$

In the collision systems studied in this work, two types of ionisation reactions are investigated: **Transfer Ionisation (TI)** and **Single Ionisation (SI)**. While, in the transfer ionisation of He, one electron is emitted from the target to the continuum and the second electron is captured by the projectile



in the single ionisation (SI) of He, only one electron is emitted from the target to the continuum and the other one stays in the bound states of the target



The Q-value for both reactions can be obtained from the following equation

$$Q_{TI(n)} = Q_{SI(n)} = -79eV + 13.6eV \frac{4}{n^2} \quad (2.28)$$

where n here is the principle quantum number of the bound electron.

2.2 Theory of slow ion-atomic collisions

Classical Approach

2.2.1 Classical-Trajectory Monte Carlo Method

In 1966, Abrines and Percival [135, 136] introduced this method in ion-atom collision studies. They used classical mechanics to study electron capture and ionization in the collision $p+H$ at intermediate velocity. Since then, this method was extensively used by many authors [25, 27, 137, 138, 139, 140] to study different inelastic processes including ionization. In this method the collision is simulated using classical mechanics, while the initial conditions contain necessary quantal information. The initial target electron is represented by spatial and momentum distributions that are calculated quantum mechanically. The target core ion is described by a model such as a screened Coulomb potential. The independent-electron model [141, 142] is used for many electron atoms. The impact parameter and the initial position and momentum of the target electron are chosen randomly. Different reaction channels are identified by looking at the final states (position and momentum of the three collision products) when the collision partners are infinitely separated. The procedure is repeated for a large number of trajectories (10^5 - 10^7). The cross sections are determined statistically from the number of events that lead to each channel. By reactions, in which, a quantum mechanical effect is dominant such as Tunneling, the *CTMC* method can not be used.

Utilizing the rapid development in computers, in 1987 [93] Olson developed the method by directly including all the electrons on the target atom. This method was called the n -body *CTMC* (n CTMC). In order to maintain parity with the experimental progress, incremental extensions have been made to the CTMC method so that now model potentials based on Hartree-Fock calculations can be used to describe the electron-nuclear interactions [143]. In addition, electrons on both target and projectile centers can be incorporated [112] so that dynamical screening of the nuclei during the collision [144] and direct inclusion of the e-e interaction in the post collision regime [119] can be also described. One of the strength of *CTMC* is that it yields a complete determination of the momenta of the product states of a collision. This makes it possible to calculate the impact parameter dependence of any inelastic process, the scattering angle of the projectile, and the energy loss (gain) by the projectile. Full information can be obtained about recoil ions [145]. For this reason the *CTMC* method has accompanied the recoil ion momentum spectroscopy development since its early days until now.

Using this method Olson [25] introduced one of the most surprising theoretical predictions in the slow ion atom collisions which is the existence of a so called saddle point ionization mechanism. The relative importance of this mechanism has been discussed within the theoretical framework of classical mechanics [26, 27, 146] as well as in various quantum mechanical approaches [34, 30, 31, 33].

Saddle Point Ionization Mechanism

On the grounds of classical mechanics, Olson suggested this mechanism. The potential between the projectile and the residual ion has a point (the saddle point) where no force acts on an electron moving between them. As projectile and target separate, the potential rises and hence electrons traveling with the velocity of this saddle could be left stranded in the continuum between the target and projectile [25]. Experimental attempts to identify a saddle point feature in the continuum electron spectra resulted in both positive and negative evidence for such a mechanism but at velocities so high that the whole concept of saddle point electrons was questionable. On the theoretical side, the saddle point process received an alternative formulation in terms of the hidden crossings theory. This Theory will be discussed later in this chapter. In this theory two major processes are identified, T - and S -process, respectively. In both processes the electron is promoted to continuum via series of hidden crossings in the complex R plane of the quasimolecular states formed during the collision. In this language, the T process corresponds to a saddle-point promotion. Experimentally, a great deal of work has been dedicated to searching for evidence for saddle point electrons, with vague results. An electron distribution centered on the saddle point is expected to shift with changing projectile and velocity according to

$$\vec{V}_s = \frac{\vec{V}_p}{1 + \sqrt{\frac{q_p}{q_t}}} \quad (2.29)$$

where \vec{V}_p and \vec{V}_s are the projectile and saddle-point velocities, and q_t and q_p are the target and projectile charges, respectively. The first experimental investigation of this mechanism was carried out by Olson et al. [27] by studying ionization during the collision $p - He$ within a projectile energy range of 60-200keV. A broad peak observed in the electron velocity spectrum at an angle of observation of 17° was considered as an evidence for the existence of a saddle point ionization mechanism. Most of the subsequent work focused on studying that peak [37, 38, 39, 41, 42, 43]. A major advance came from the work of Dörner et al. [46]. They applied the Cold Target Recoil-Ion Momentum Spectroscopy (COLTRIMS) to obtain a much more detailed differential picture of the velocity distributions of electrons emitted in collisions of protons with He at projectile velocities 0.45, 0.64, and 0.78 a.u.. They found that at large impact parameters nearly all electrons are in a board range around the saddle point. To answer the question whether the electron longitudinal velocity distribution does follow Eq. 2.29, Kravis et al. [45] and Abdallah et al. [50] performed a series of experiments with light, bare ions colliding

with He and Ne. It was concluded that the maximum of the electron distributions did not follow the velocity and charge state dependence predicated by Eq. 2.29.

Quantum Mechanical Approach

When the velocity of the projectile V_p is comparable to or less than the typical target electron orbital velocity, a transient molecule is formed during the collision which plays a major role in determining the inelastic processes that take place, including excitation, charge transfer and ionization. The two nuclei come close to each other and there is enough time that an electron is shared temporarily by both nuclei. In this regime, any perturbative treatment of collision is expected to give poor results due to the strong interaction between the projectile ion, target atom and the target atom active electron. The need for rigorous quantum nonperturbative treatment then arises. One commonly used approximation in this velocity range is so-called "semi-classical approximation", whereby the electrons motion is described quantum mechanically while the nuclear motion is described classically.

2.2.2 The Quasi-Molecular Model: Diabatic Verses Adiabatic

Time Dependent Formalism

We consider a projectile of charge Z_p incident on a hydrogen-like-atom with a nuclear charge Z_T . The center of mass coordinate is shown in Fig. 2.1. The total Hamiltonian of this system can be divided into two parts in order to separate the fast motion of the electrons (the electronic Hamiltonian H_{el}) from the slow motion of nuclei (a nuclear part T_R) [147]

$$H = T_R + H_{el} \quad (2.30)$$

where

$$T_R = - \frac{1}{2\mu} \nabla_R^2 \quad (2.31)$$

$$H_{el} = \frac{Z_p Z_T}{R} - \nabla_r^2 - \frac{Z_p}{r_1} - \frac{Z_T}{r_2} \quad (2.32)$$

where μ is the reduced mass of the nuclei.

The total wave function ψ , which is the solution of the time-dependent Schrödinger equation

$$H \psi = E \psi \quad (2.33)$$

can be expanded into an orthonormal basis set of electronic wave function $\phi_i (R, r)$

$$\psi = \sum_i F(R) \phi_i (R, r) \quad (2.34)$$

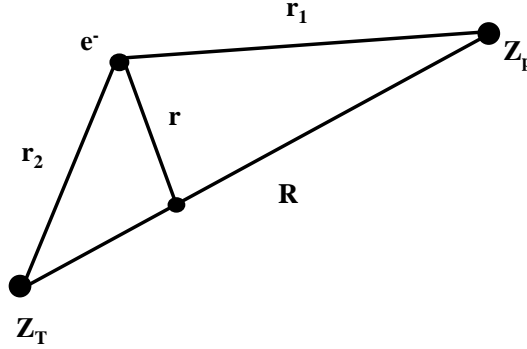


Figure 2.1: Coordinate system used to describe the collision of a bare ion Z_p with atom of nuclear charge Z_T .

substituting Eq. 2.30 and Eq. 2.34 in Eq. 2.33, multiplying the left by $\langle j |$ and integrating over the electronic coordinates, one gets the set of coupled equations:

$$[T_R + \langle j | H_{el} | j \rangle - E] F_j(R) = - \sum_{i \neq j} [\langle i | H_{el} | j \rangle - \frac{1}{\mu} \langle i | \nabla_R | j \rangle \cdot \nabla_R] F_i(R) \quad (2.35)$$

where second order terms in $\langle |\nabla^2| \rangle$ were neglected.

The left hand side of Eq. 2.35 contains the elastic scattering in the j channel for a collision energy E . The right hand side contains the coupling terms which induce electronic transition between the channel $|j\rangle$ and the other channels $|i\rangle$. The term $\langle i | H_{el} | j \rangle = \varepsilon_{ij}(R)$ represents the electronic coupling term and $\langle i | \nabla_R | j \rangle \cdot \nabla_R$ is the dynamic coupling term.

In order to use Eq. 2.35 in calculations for inelastic processes, one must use a suitable basis function $\phi_i(R, r)$ that has the correct asymptotic behavior (as the two atoms set of infinitely separated).

Adiabatic Representation

If the molecular orbitals (MOs) are chosen as basis, then

$$\langle i | H_{el} | j \rangle = \varepsilon_{ij}(R) \delta_{ij} = \varepsilon_j^A(R) \quad (2.36)$$

where

$$\delta_{ij} = \langle i|j \rangle = \langle \phi_i|\phi_j \rangle \quad (2.37)$$

Then Eq. 2.35 reduces to

$$[T_R + \varepsilon_j^A(R) - E] F_j(R) = - \sum_{i \neq j} \frac{1}{\mu} \langle i|\nabla_R|j \rangle \cdot \nabla_R F_i(R) \quad (2.38)$$

Therefore, in this representation only the dynamical coupling exists between different channels. This representation is referred to as the adiabatic representation as it inherently allows the electronic cloud to adapt to the slowly moving nuclei.

Diabatic Representation

Alternatively, one can look for a basis set functions $\phi_i(r)$ that do not depend on R . One may choose atomic orbitals (AOs), for instance. The coupling then arises from the electronic term. $\varepsilon_{ij}(R)$ will no longer be diagonal

$$\langle i|H_{el}|j \rangle = \varepsilon_{ij}^D(R) \quad (2.39)$$

and Eq. 2.35 is rewritten as

$$[T_R + \varepsilon_j^D(R) - E] F_j(R) = - \sum_{i \neq j} \varepsilon_{ij}^D(R) F_i(R) \quad (2.40)$$

Such representation is usually called *Diabatic* representation.

2.2.3 Dynamical Coupling Terms

The physical meaning of the dynamical coupling terms is best seen within a semi-classical treatment of the collision. In a time dependent version, the expansion shown in Eq. 2.34 is now written as

$$\psi(t, R, r) = \sum_i a_i(t) \chi_i(R, r) \quad (2.41)$$

The time-dependent Schrödinger equation therefore reads

$$i \frac{\partial}{\partial t} \psi(t, R, r) = H \psi(t, R, r) \quad (2.42)$$

Substituting Eq. 2.41 in Eq. 2.40 and making use of the orthonormality of the basis χ_i , the set of the coupled equations are written now as follows

$$i \frac{d}{dt} a_j = \sum_i \langle \chi_j | H - i \frac{\partial}{\partial t} | \chi_i \rangle a_i(t) \quad (2.43)$$

where the term $\langle \chi_j | H - i \frac{\partial}{\partial t} | \chi_i \rangle$ contains the dynamical coupling. By defining the scattering plane to be the XZ plane, the operator $\frac{\partial}{\partial t}$ can be reexpressed as

$$\frac{\partial}{\partial t} = \frac{d}{dR} \frac{\partial}{\partial R} + \frac{d\theta}{dt} \frac{\partial}{\partial \theta} = V_R \frac{\partial}{\partial R} + V_p \frac{b}{R^2} iL_Y \quad (2.44)$$

where b is the impact parameter, V_p is the initial projectile velocity, V_R is the radial velocity, θ is the angle of rotation of the internuclear axis, and $iL_y = \frac{\partial}{\partial \theta}$ is the electronic orbital angular momentum operator perpendicular to the collision plane.

The dynamical coupling term is then rewritten as

$$\langle \chi_i | \frac{\partial}{\partial t} | \chi_j \rangle = V_R \langle \chi_i | \frac{\partial}{\partial R} | \chi_j \rangle + \frac{V_p b}{R^2} \langle \chi_i | \frac{i}{iL_Y} | \chi_j \rangle \quad (2.45)$$

Radial Coupling

The first term in Eq. 2.45, $V_R \langle \chi_i | \frac{\partial}{\partial R} | \chi_j \rangle$, represents the radial coupling term. It describes the tendency of the electronic charge cloud to maintain its position along the internuclear axis as the particles approach and couples molecular states of the same symmetry, i.e., the states which have the same projection of the angular momentum on the internuclear axis. This projection is represented by the quantum number m . In other words, the radial coupling term couples molecular states for which $\Delta m = 0$, e.g. $\sigma \leftrightarrow \sigma$, $\pi \leftrightarrow \pi$.

Rotational Coupling

The second term in Eq. 2.45, $\frac{V_p b}{R^2} \langle \chi_i | \frac{i}{iL_Y} | \chi_j \rangle$, called the rotational coupling term couples molecular states that are obeying the rule $\Delta m = \pm 1$; $\sigma \leftrightarrow \pi$, $\pi \leftrightarrow \sigma$ for instance. On the contrary to the radial coupling, the rotational coupling arises from rotation of the internuclear axis as the internuclear distance of the two colliding particles changes. Per definition the molecular orbitals are attached to the internuclear axis. Thus, in order to maintain their identity during the collision they have also to rotate with respect to a fixed frame. If molecular forces were not acting on the orbital it would tend to stay space fixed as shown in Fig. 2.2 and thereby clearly change its symmetry with respect to the internuclear axis from σ at an early time to π at later time. This is what is called rotational, or sometimes Coriolis, coupling. The L_{\perp} operator which is responsible for this essentially geometric effect just couples molecular states with $\Delta m = \pm 1$.

2.2.4 Molecular Orbital Approximation

The molecular orbital approximation assumes an independent particle model in which the stationary states of the transient molecule are built up of a product of one electron orbital wave functions. Thus, the total electronic wave function can be described by stating the electron configuration in terms of molecular orbitals. At small

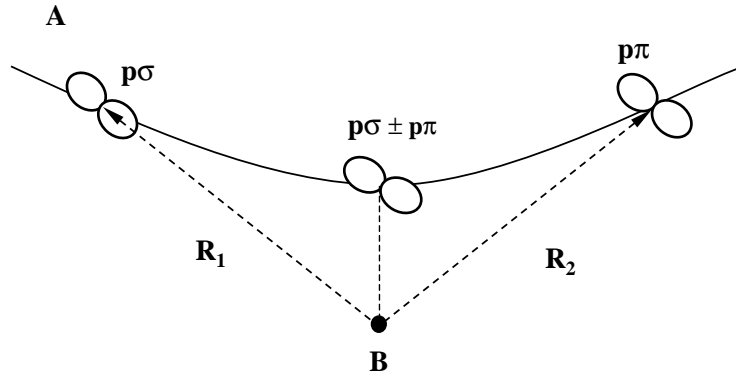


Figure 2.2: Schematic of molecular orbitals during a collision process. Space-fixed p orbital (rotational coupling active) which from the molecular (internuclear) axis is effectively seen as a σ orbital at distance R_1 and as a π orbital at R_2 .

internuclear distances ($R \rightarrow 0$) the molecular orbitals go over into atomic orbitals of the united atom (UA limit). Since energy levels of the united atom are usually well known or easily estimated, one can obtain the energies of the molecular states at $R \approx 0$. At medium internuclear distribution the molecular orbitals (MO) can be described fairly accurately as a linear combination of atomic orbitals ($LCAO$). At very large internuclear distances where the MO approximation at times becomes inaccurate, one can specify the wave function of the entire system in terms of the wave functions of the separate atoms (AO approximation; SA limit). It is important to mention, that in addition to the potential energy the electrons have kinetic energy in the CM system since they move with the nuclei. The electron translational factors (ETF 's) introduced by Bates and McCarroll [148] in the electronic wavefunction account for this to ensure Galilean invariance. The most common ETF 's are simple exponential functions of the electron momentum, $\mathbf{p}_i e^{i\mathbf{p}\cdot\mathbf{r}}$.

Correlation Diagrams

During the transition between the SA limit and the UA limit, molecular orbitals are formed. Due to the symmetry considerations, atomic orbitals in the SA limit evolve to certain molecular orbitals at intermediate internuclear distances and finally to specific atomic orbitals in the UA limit. This kind of correspondence is usually represented by molecular orbital correlation diagram. In addition some of these diagrams show not only the electronic energy but also add the heavy particle potential energy.

For the purpose of illustration, we discuss the correlation diagram of the $H^+ + H$ collision system. This genuine one electron system is the prototype of a three-body Coulomb problem. Fig. 2.3 shows the correlation diagram of H_2^+ molecule; the united atom $He^+(n'l)$ limit on the left side and the separated atom limit $H + H(nl)$

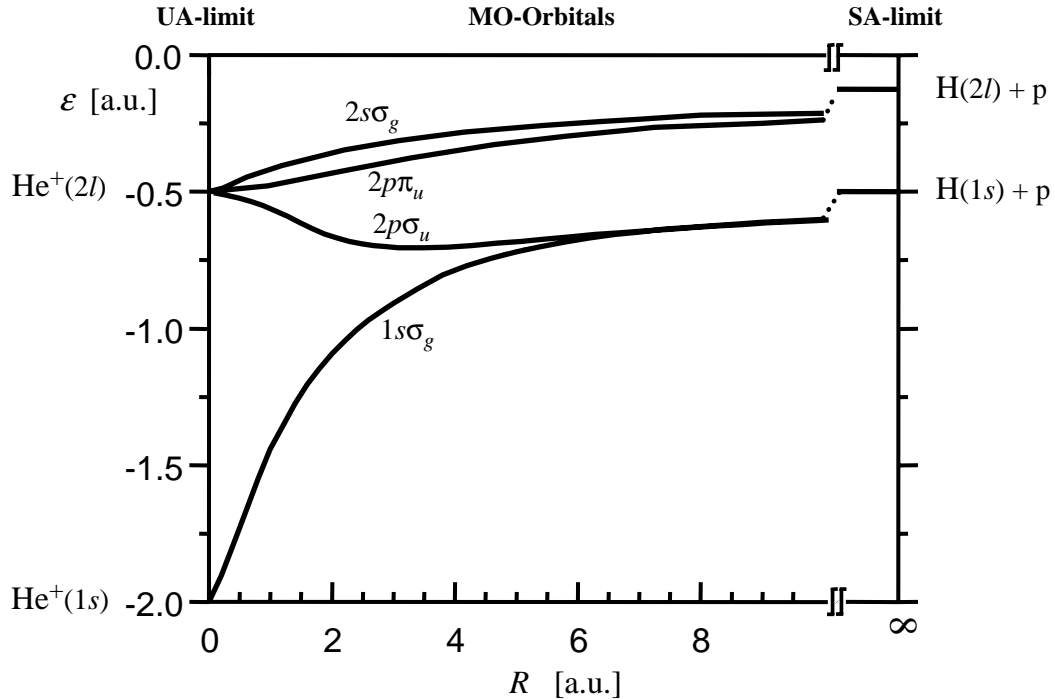


Figure 2.3: Lowest four potential curves of H_2^+ . The united atom $He^+(n'l)$ limit is on the left side and the separated atom limit $H + H(n'l)$ on the right side of the figure.

on the right side of the figure. When describing this system quantum mechanically in the *MO* picture, the wavefunction in Eq. 2.34 has to contain both *g* and *u* states which are linear combination (*LCAO*) of atomic orbitals located at the nuclei. In resonant charge exchange for example the asymptotic wavefunction is given by

$$\psi_{\pm}(r) = (\psi_{1s\sigma_g}(r) \pm \psi_{2p\sigma_u}(r))/\sqrt{2} \quad (2.46)$$

r being the electron coordinate and the \pm referring to the electron being localized at one proton or the other, respectively. During the collision the probability amplitudes for the two states involved change since different phases are picked up on the $1s\sigma_g$ and $2p\sigma_u$ potential energy curves, depending on the impact parameter b and the energy E . Thus, for large internuclear distance, $R \rightarrow \infty$, we will find the system in a state

$$\psi_{\pm}(r) = (a_g(t = \infty, b)\psi_{1s\sigma_g}(r) + a_u(t = \infty, b)\psi_{2p\sigma_u}(r))/\sqrt{2} \quad (2.47)$$

which has to be compared with Eq. 2.46. Thus, the probability for finding the electron at either of the protons, \pm in Eq. 2.46, will depend on the impact parameter and collision energy. Fig. 2.4(a) shows an example of a rotational coupling in the transition $H^+ + H(1s) \rightarrow H^+ + H(2p)$.

A schematic picture of the relevant coupling terms is given in Fig. 2.4(b), which illustrates the relative importance of the rotational and radial coupling among the ungerade (u) and gerade (g) states. We note from Fig. 2.4(b) that the most significant interaction is the rotational coupling between the $2p\sigma_u$ and $2p\pi_u$ states at close internuclear distances where the two potential energy curves approach each other.

The $2p\sigma_u$ - $2p\pi_u$ rotational coupling

For very small R values the $2p\sigma_u$ and $2p\pi_u$ states are nearly degenerate. The transition between these two states, induced by the $V_0 b/R^2 < 2p\sigma_u | L_y | 2p\pi_u >$ rotational coupling term leads to the selective excitation of the $H(2p)$ state [150]. It should be stressed that the selective $2p$ excitation through the $2p\sigma - 2p\pi$ rotational coupling is a common feature of K shell interactions as has indeed been observed both in inner and outer shell collision processes.

Very recently, the electron momentum distributions for the $p-H$ collision system have been calculated by Macek and Ovchinnikov [151, 49] using an alternative basis set called *Sturmain* basis. Based on these calculations, the two-fingered structure of the electron momentum distribution has been explained. They have suggested that the ionization process begins with rotational coupling of the $2p\sigma$ orbital occupied by the incoming active electron into a $2p\pi$ one at small internuclear distances. The $2p\pi$ orbital is then eventually promoted via a series of radial crossings (the so-called T process) into the continuum, keeping the π character. This description of the ionization process will be helpful in the interpretation of our results. Since there are no theoretical calculations of the electron momentum distributions for the systems studied in this work.

2.2.5 Hidden Crossings Theory

This theory is an extension of the adiabatic theory. It describes non-adiabatic transitions in slow atomic collisions and has been thoroughly reviewed by Solov'ev [152]. The theory based on the analytic continuation of the adiabatic potential curves into the complex plane (where they become potential surfaces). Since the Hamiltonian is an analytic function of the internuclear distance the potential surfaces are different sheets of the same analytic function connected by branch points where the curves cross exactly [152]. These crossings are called hidden crossings because they can not be identified with any crossings of the real potential curves. They can therefore be distinguished from the well known avoided crossings. Transitions between levels via hidden crossings are determined by branch points connecting them. These complex branch points can be interpreted physically. The real part indicates the region of the internuclear distances where the transitions take place, while the imaginary part determines the transition probability (a small imaginary part corresponds to a large transition probability).

As an illustration, let us assume two diabatic potential curves $U_1(R) = E_o + \alpha R$ and $U_2(R) = E_o - \alpha R$. The two levels interact via a potential W which is

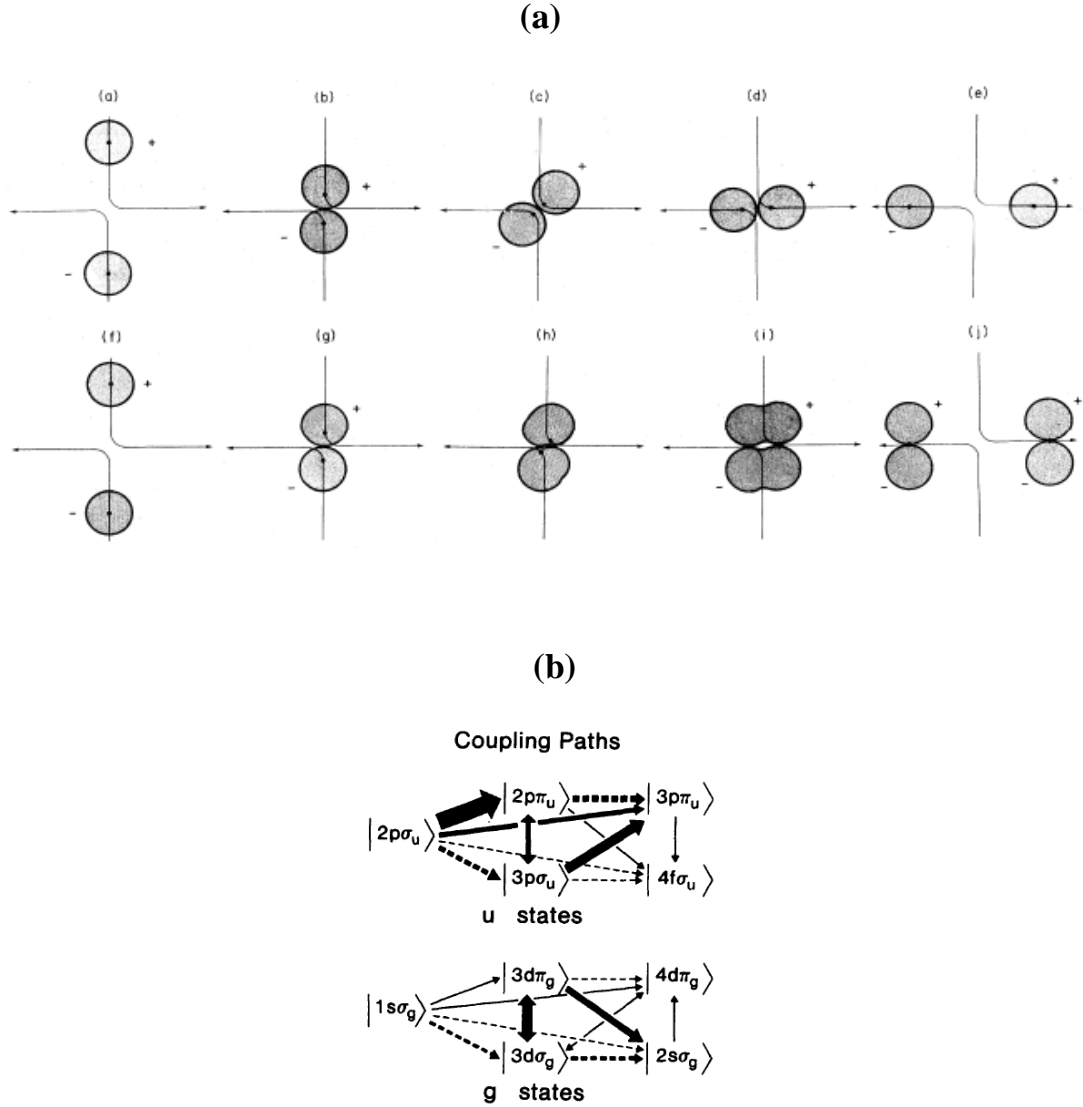


Figure 2.4: **(a)** Rotational coupling in the transition $H^+ + H(1s) \rightarrow H^+ + H(2p)$. Collisions in which the nuclei scatter to 90° are represented. (a)-(e) illustrate a very slow collision: (a) The electrons begin in the *ungerade* superposition of $1s$ atomic states. (b) for small internuclear separations, this state becomes a $2p\sigma$ united-atom state. (c), (d) If the internuclear axis rotates slowly, the electronic state follows. (e) As the nuclei move apart, the electronic state again becomes the *ungerade* superposition of $1s$ states. No transition has occurred. (f)-(j) illustrate the consequence of more rapid motion on the same path: (f), (g) just as (a), (b). (c) If the internuclear axis rotates too rapidly, the electronic state might not follow. (d) As the axis rotates further, the electronic state becomes $2p\pi$. (e) The $2p\pi$ molecular state dissociates into the *ungerade* superposition of separated-atom states. The transition occurred because the electrons could not follow the rapidly rotating internuclear axis. **(b)** Effective couplings paths for u and g manifolds in $H^+ - H(1s)$ collisions. (\longrightarrow) represents rotational coupling and (\dashrightarrow) is the radial coupling. Thickness of connecting arrow indicates qualitative importance (adapted from [149]).

independent of R (as in Landau-Zener model). The corresponding adiabatic energy levels are

$$E_1(R) = E_o - \sqrt{(\alpha R)^2 + W^2} \quad (2.48)$$

$$E_2(R) = E_o + \sqrt{(\alpha R)^2 + W^2} \quad (2.49)$$

These two curves pseudo-cross at the interaction point of the diabatic levels. In the complex plane of R , $E_1 = E_2$ at the two branch points $R_c = \pm \frac{i}{\alpha}W$. Near the branch points R_c , the energy difference between the two adiabatic states is

$$\Delta E(R) = E_1(R) - E_2(R) \approx A\sqrt{R - R_c} \quad (2.50)$$

where A is a constant. Upon moving around a branch point R_c , states are switched. At low relative velocities v of the nuclei the probability of a transition is expressed through the contour integral of the energy difference around the branch point

$$P = \exp\left(-\frac{2\Delta}{V_p}\right) \quad (2.51)$$

where V_p is the collision velocity. Δ is the Massey parameter and is given as a contour integral in the complex plane

$$\Delta = \left| \text{Im} \int_{\text{Re}(t_c)}^{t_c} \Delta E(R(t)) V_p dt \right| \quad (2.52)$$

where t_c is the complex root of the equation $R(t_c) = R_c$, and $R(t)$ is the time dependent internuclear distance.

Three types of hidden crossings have been found. First calculations by Solov'ev [152] revealed series of branch points, which were denoted as the S -series. This series is associated with transitions while moving from the SA limit to the UA limit. Therefore electron promotion to the continuum happens via this process while the two nuclei are approaching each other. Later Ovchinnikov and Solov'ev [153] discovered the so-called P - and T -series. The P -series only arise when there is a small difference in charge. The T -series are associated with diabatic transitions of electrons located on the top of the internuclear potential barrier (which is the saddle point) to higher levels. Therefore electrons are promoted to the continuum while the two nuclei are receding from each other. The T process is the equivalent of the (classical) saddle point ionization mechanism.

Detailed study of the $H^+ H$ system within framework of the theory of hidden crossings was carried out by M. Pieksma [154]. The two types of hidden crossings for this system are shown in Fig. 2.5 and 2.6. One can notice that the S -type crossings lead to continuum while the two centers are approaching each other. On the other hand the T -type crossings lead to the continuum while they are departing from each other. Fig 2.7, illustrates the spiral shape surface leading from one level to another by moving around a branch point.

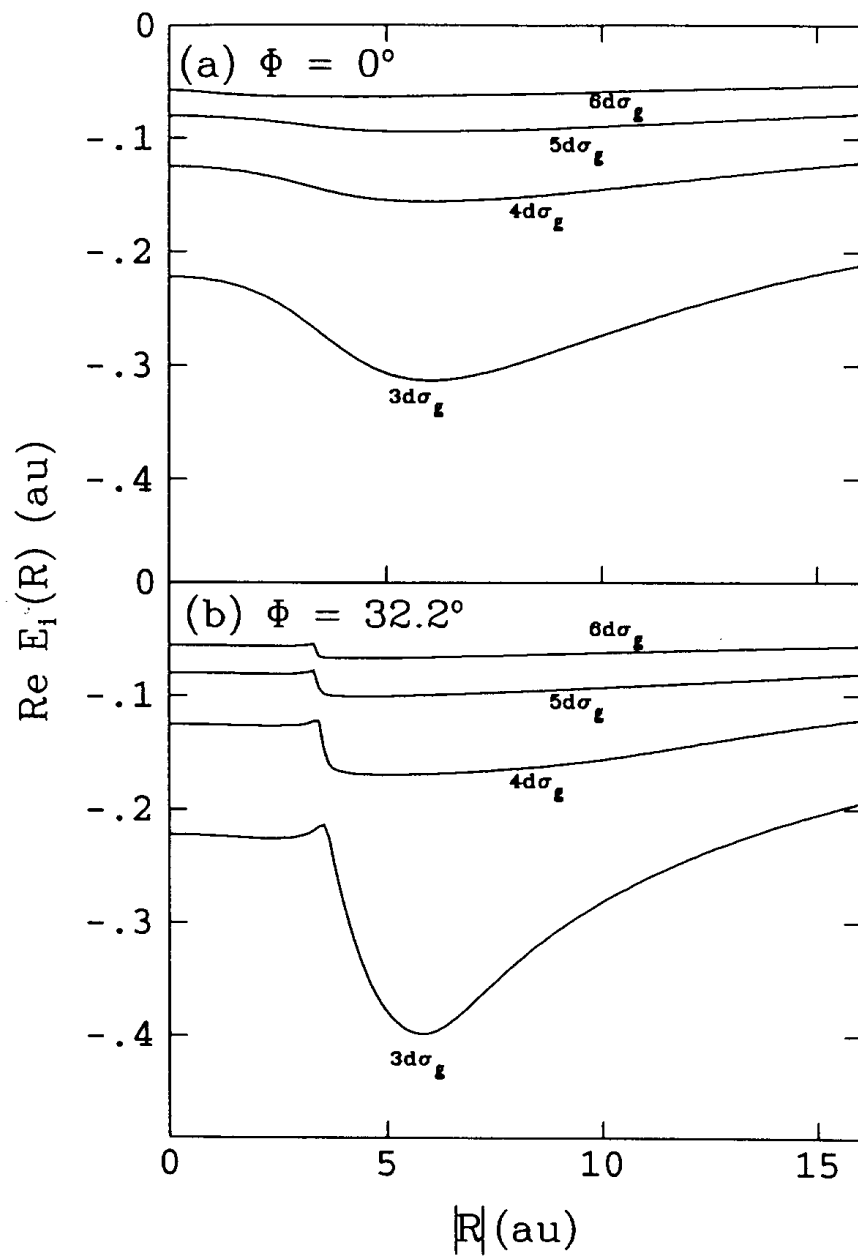


Figure 2.5: Potential energy curves for H_2^+ quasimolecule. (a) along the real axis ($\Phi=0^\circ$) and (b) along an axis in the complex plane which makes an angle $\Phi=32.2^\circ$ with the real axis. The *S*-type hidden crossings can be seen in (b). (Adapted from M. Pieksma [154]).

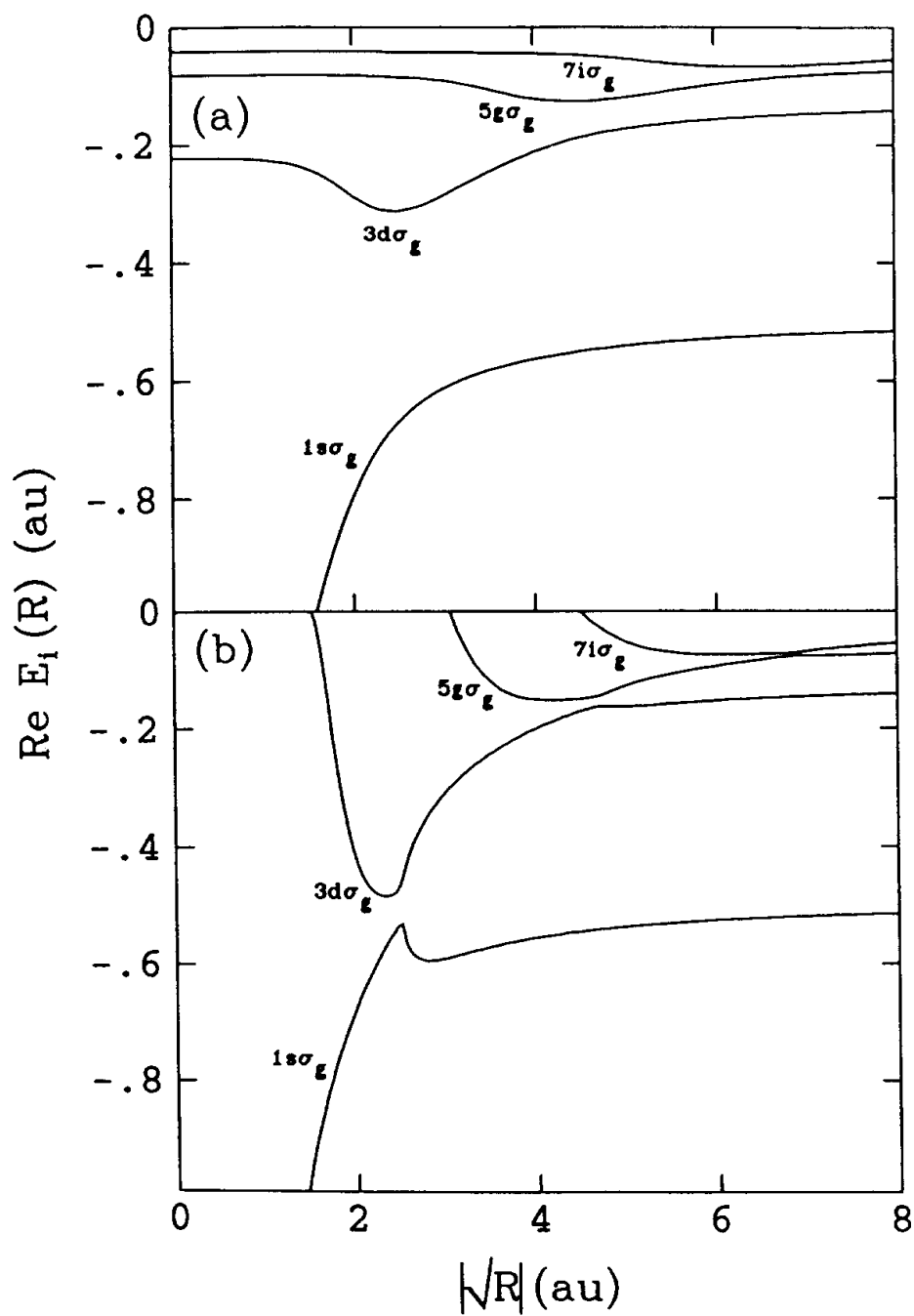


Figure 2.6: The same as Fig. 2.5, but now in the complex $R^{\frac{1}{2}}$ plane showing the T -type hidden crossings. In (a) the path was chosen along the real $R^{\frac{1}{2}}$ axis. In (b), the path is taken along a straight line path that passes close to successive T branch points. (Adapted from M. Pieksma [154]).

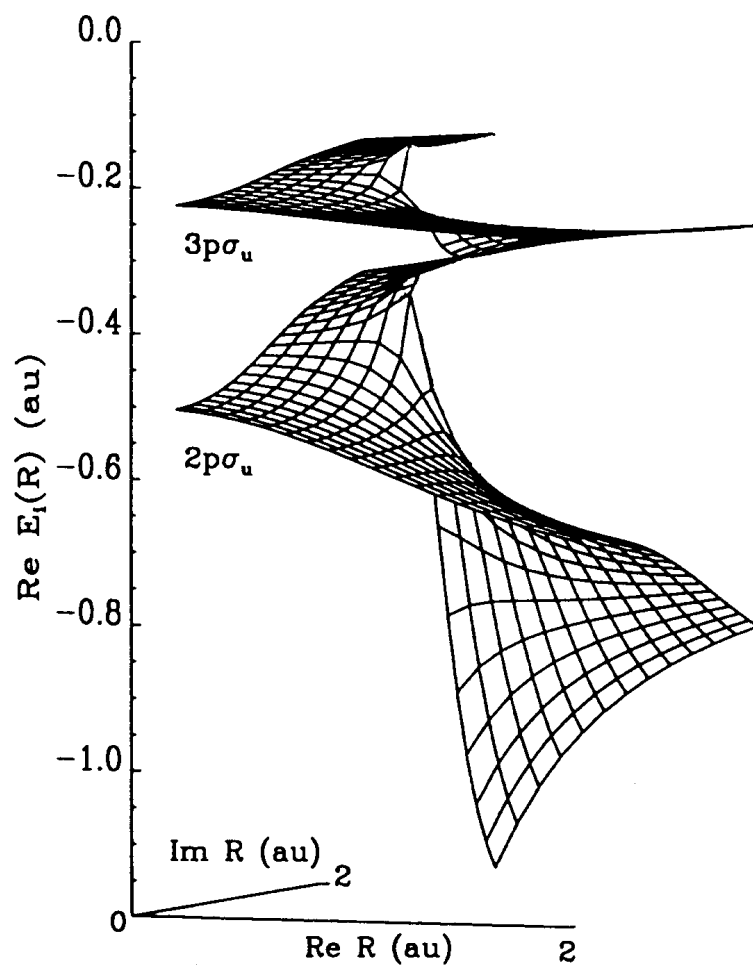


Figure 2.7: Real part of the potential energy as a function of the complex internuclear distance R for two levels connected by an S -type branch point. (Adapted from M. Pieksma [154]).

2.2.6 Direct Solutions of the Time Dependent Schrödinger Equation On a Grid

An additional approach for ion-atom collisions is the direct solution of the time dependent Schrödinger equation on a numerical lattice [155, 156, 157, 158, 159]. Due to the long-range nature of the Coulomb electrostatic force, however, only the substantial advances in computer technology over the last few years have allowed the possibility of carrying out full three-dimensional lattice calculations. A general advantage of the lattice method lies in its application over a wide energy range. A numerical lattice method makes no assumption regarding the suitability of any particular basis set expansion. A further advantage is that collision dynamics may be easily visualized since the total wave function is calculated explicitly as a function of time. Lattice size is generally the main determinant of overall computational time.

1D, 2D and recently 3D lattice solutions have been employed to study different processes in the ion-atom collisions, especially in the p-H collision system [160, 161, 162, 163]. Kolakowska et al. [161] have solved the Schrödinger equation for the $p - H$ collision system using two different lattice techniques, the finite-difference method and Fourier collection method, to obtain a discrete representation of the wave function and all operators on a three Cartesian coordinates grid. The collision dynamics are revealed by examination of time-evolving electron probability density dots. Furthermore, Wells and Co-workers [162] have obtained ionization cross sections by projecting the wave function onto the stationary states of the target.

To employ such technique to study a two-electron collision system such as the collision system investigated in this work, the numerical solution must be done on a 6-dimensional lattice. The implementation of such calculation with sufficient resolution can not be realized because of the extension of the computational expensive. The lattice approach is extended to two electron targets using the time-dependent Hartree-Fock (TDHF) theory. The TDHF-method allows to calculate systems by treating only one electron in an explicitly time dependent screened potential [157, 164].

The Time Dependent Hartree Fock Theory

In the TDHF approach, one assumes that the many-electron wave function can, for all times, be characterized with sufficient accuracy as a Slater determinant of one-electron orbitals. Variation of the electron integral [165] [165]

$$J = \int dt \langle \phi | H_{el} - id_t | \phi \rangle \quad (2.53)$$

with respect to the one-electron wave functions ϕ_j^* leads to the standard set of N coupled, non-linear differential equations known as the *TDHF* equations. For the two-electron system such as $He^{2+} - He$ system, they take the form

$$i\frac{\partial}{\partial t}\phi_j = h_o\phi_j + (D - A)\phi_j \quad j = 1, 2. \quad (2.54)$$

where h_o is the one-particle Hamiltonian, D is the screened potential calculated from the charge distribution of the electrons and A is the exchange potential. Concerning the $He^{2+} - He$ system, the ionic motion which is decoupled from the electronic motion is represented by Coulomb trajectory for two point charges. When all electrons in the initial state occupy the similar orbital, the position parts of both one-electron wavefunctions will agree with one another. Thus, the *TDHF*-approximation can be applied for this system and one only needs to calculate the time development of the one-electron wavefunction, because the development of both one-electron wavefunctions followed the same equation. In the case that the spin of the two electrons are anti-parallel, the second term in Eq. 2.54 can be simplified to

$$(D - A)\phi(\vec{r}) = \int d\vec{r}' \frac{|\phi(\vec{r}')|}{|\vec{r} - \vec{r}'|} \phi(\vec{r}) \quad (2.55)$$

Several studies are performed on the $He^{2+} - He$ system utilizing the *TDHF* method [157, 164, 166].

The Two Centre Momentum Space Disretization Method

This method was introduced by E. Sidky and C.D. Lin [167] in an attempt to solve the time-dependent Schrödinger equation exactly, in the numerical sense. They construct the electron wavefunction in momentum space. The wavefunction is expanded in spherical harmonics about both target and projectile centers, both of which are stationary in momentum space, assuming a straight-line projectile trajectory. The two-center expansion limits the number of harmonics necessary thereby reducing the computational effort. The main advantage of expressing the wavefunction in momentum space is that one knows that the wavefunction is confined, i.e, the wavefunction goes to zero for large momentum. To avoid difficulties in evaluating the convolution integrals present in the momentum space Schrödinger equation, they have transformed the basis to coordinate space following a similar strategy to the three-dimensional Fourier gride method [168]. They have employed this technique to solve the Schrödinger equation for proton impact at energies from 5 to 100keV on atomic hydrogen and at an impact-parameter value of 1.2 a.u. [169]. The collision system is viewed in standard semiclassical framework, where the internuclear motion is classical and the electron is treated fully quantum mechanically. Furthermore, the projectile motion is assumed rectilinear with constant velocity \vec{v} and impact parameter \vec{b} . To account for the two-center nature of the collision system the momentum space wavefunction Φ is expanded in spherical harmonics about both nuclear centers

$$\Phi(\vec{p}, t) = \sum_{l,m} \tilde{T}_{l,m}(p, t) Y_{l,m}(\hat{p}) + e^{-i(\vec{p} \cdot \vec{R} - \frac{1}{2}v^2t)} \sum_{l,m} \tilde{P}_{l,m}(q, t) Y_{l,m}(\hat{q}) \quad (2.56)$$

where

$$\vec{q} = \vec{p} - \vec{v} \quad \text{and} \quad \vec{R} = \vec{v}t + \vec{b} \quad (2.57)$$

\tilde{T} and \tilde{P} are functions in momentum space which depend on time and the magnitude of the momentum with respect to the target and projectile respectively. Although no explicit mention of rotational coupling was made in the calculation, the results reproduced the two-fingered structure seen in the data of Dörner et al. [46]. This structure was identified within their formalism as being caused by a two-island structure: one island is associated with target projectile-centered basis states and one with target-centered states. More recently, Sidky and Co-workers [3] have employed this method to investigate the role of the saddle-point promotion. They have observed that only a small fraction of the continuum electrons released for 1 a.u. p on H originate from the saddle promotion scheme. They have provided a classification of ejected electrons into saddle point and kinetic electrons and their results show that this classification is valid for a broad range of impact energies. They found in classical calculating as well as in using their *TCMSD*-method a significant emission of fast forward electrons, i.e., $V_{e,z} > V_p$.

2.3 Basic Concepts in the Ion-Molecule Collisions

2.3.1 Fragmentation Process: Coulomb-Explosion Model

Fragmentations, in which all fragments are positively charged, are often referred to as *Coulomb-Explosions (CE)* and the following model is assumed: In the collision process valence electrons are removed from the molecule during an interaction time which is short on the time scale defined by the rotation and vibration periods of the molecule. In this case the fragmentation dynamics is governed by the strong mutual repulsion of the positive ions, and the kinetic energies and emission angles may be computed by assuming Coulomb forces acting between point charges. The Coulomb potential energy, i.e.,

$$V(r) = \frac{q_1 q_2}{r} \quad (2.58)$$

stored in the fragments at small distance is converted into kinetic energy as the fragments move away from each other. This model produces approximately a *Gaussian* distribution for the energy of the emitted fragments centered around $\frac{q_1 q_2}{r_o}$ where r_o is the average internuclear distance. Due to its simplicity, this model is frequently used. However, the energy spectra are sometimes reported to be insufficient if the energy and angular spectra are studied in more detail, i.e, when, for instance, the screening effects are included in the study.

2.3.2 Frank Condon Principle

In considering transitions between two electronic states in a molecule there is an important principle known as the *Frank-Condon* Principle [170, 171]. In essence,

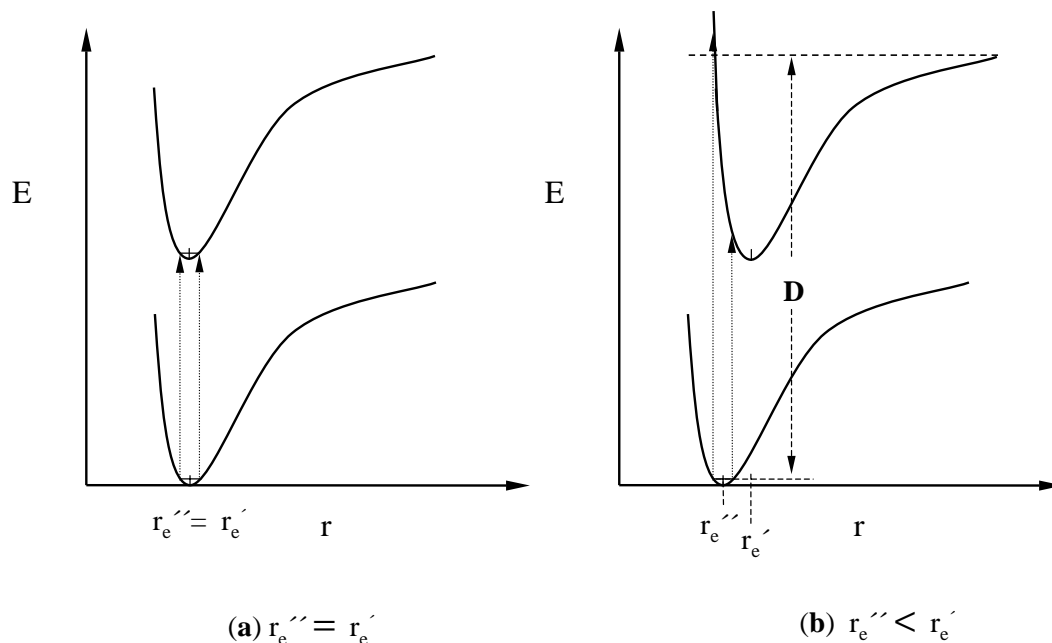


Figure 2.8: Vertical transitions between two electronic states: in (a) $r_e'' = r_e'$ and in (b) $r_e'' < r_e'$. The transition D represents a dissociation.

it states that the electronic transitions from vibrational levels of one electronic state to vibrational levels of another electronic state take place in a time much shorter than that of a single vibration. Hence the nuclei, because of their large masses, have very nearly the same positions and velocities before and after the transition which takes about 10^{-15} sec. These are known as vertical transitions and are illustrated in Fig. 2.8. The Figure also shows that the transition from the lower electronic state occurs from points on the potential curve. This is to be expected classically since such points correspond to extremes of the oscillatory motion where the velocity is zero. Since the molecule spends more time in the vicinity of the extremes, the probability of a transition from these positions is increased. This idea was worked out mathematically and put on quantum mechanical basis by *Condon* [171].

Assume that the wavefunction of a vibrating molecule, without rotation, is written in the Born-Oppenheimer approximation [147] as

$$\psi = \psi_e \psi_v \quad (2.59)$$

where ψ_e is a function of electronic coordinates with the nuclei in their equilibrium positions and ψ_v is a vibrational eigenfunction. It is also assumed that

$$\langle \psi_{ef} | \psi_{ei} \rangle = 0 \quad (2.60)$$

where i and f refer to initial and final states. The matrix element for the transition

is

$$\langle \psi_f | \mathbf{R} | \psi_i \rangle = \langle \psi_{ef} \psi_{vf} | \mathbf{R}_e + \mathbf{R}_v | \psi_{ei} \psi_{vi} \rangle \quad (2.61)$$

in which \mathbf{R}_e is the transition moment operator for transitions electronic states and \mathbf{R}_v is the same for vibrational states. Expanding Eq.2.61

$$\langle \psi_f | \mathbf{R} | \psi_i \rangle = \langle \psi_{vf} | \psi_{vi} \rangle \langle \psi_{ef} | \mathbf{R}_e | \psi_{ei} \rangle + \langle \psi_{ef} | \psi_{ei} \rangle \langle \psi_{vf} | \mathbf{R}_v | \psi_{vi} \rangle \quad (2.62)$$

In view of the orthogonality of the electronic wavefunctions, the second term will vanish leaving

$$\langle \psi_f | \mathbf{R} | \psi_i \rangle = \langle \psi_{vf} | \psi_{vi} \rangle \langle \psi_{ef} | \mathbf{R}_e | \psi_{ei} \rangle \quad (2.63)$$

The two vibrational functions ψ_{vi} and ψ_{vf} belong to two different electronic states with different potential functions. There is, therefore, no requirement for ψ_{vi} and ψ_{vf} to be orthogonal. The integral $\langle \psi_{vi} | \psi_{vf} \rangle$, known as the overlap integral or the *Frank – Condon* integral, multiplies the electronic transition matrix element (Eq. 2.63) and therefore, exerts an important influence on the intensity of a transition. Near the end points, the overlap integral is greater, hence the probability of a transition is increased. Thus, either classically or quantum mechanically the most probable transitions are those that occur when the nuclei scarcely move [172].

2.3.3 Energy Distribution of the emitted Fragments: Reflection method

Collisional fragmentation of a molecule by a charged particle can usually be described as a two-step process: a vertical Frank-condon electronic transition induced during the collision, followed by dissociation of the excited molecular state. The kinetic energy of the emitted fragments is fixed by the electronic transition induced in the molecule and the internuclear separation at the instant of electronic excitation. This is easily seen in a potential energy diagram like that in Fig.2.9. For a particular electronic transition the total kinetic energy of the fragments is seen to be the distance above the dissociation limit of the point on the upper potential curve to which transition takes place. The energy distribution of the fragments may be determined approximately by the reflection method [173], in which the square of the ground-state vibrational eigenfunction is reflected in the upper potential curve onto the energy axis. The matrix-element which represents the energy of a emitted fragment can be obtained by

$$T = A \cdot \langle \Psi_f(R, r) | V | \Psi_i(R, r) \rangle \quad (2.64)$$

where A is a constant, $\Psi_f(R, r)$ and $\Psi_i(R, r)$ are the initial and final state of the molecule and V is the potential of the projectile. Upon the *Frank – condon* principle, during the electronic transition, relative position of nuclei do not change.

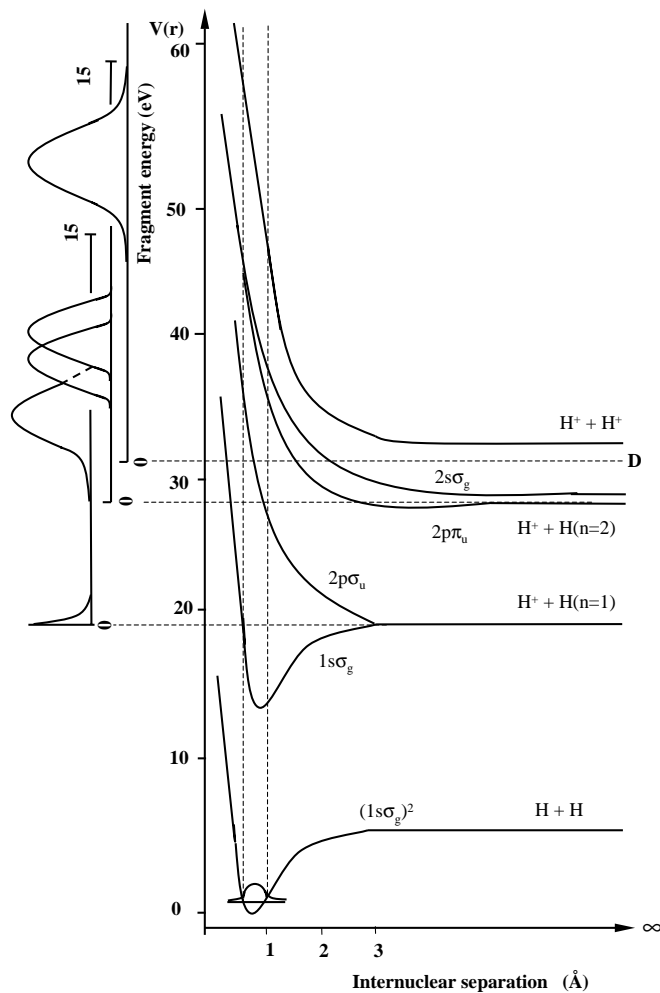


Figure 2.9: Potential energy curves for selected states of H_2 and H_2^+ : from Sharp et al. [174]. Also shown are the predictions of the shapes of the fragment proton energy spectra produced by *Frank – Condon* transitions and subsequent dissociation of the repulsive states of H_2^+ and H^+H^+ [175]. D represents the dissociation limit.

Therefore, R is constant during the transition. By carrying out the integration over the electronic wavefunction, this becomes

$$T = A \cdot U_e \cdot \langle \chi_f | \chi_i \rangle \quad (2.65)$$

where $U_e = \langle \phi_f(R, r) | V | \phi_i(R, r) \rangle$ is the matrix element for the electronic transition from the initial state (i) to the final state (f). By defining U_N as the matrix-element for the transition of the nuclei from the initial state (i) to the final state (f), then Eq. 2.65 becomes

$$T = A \cdot U_e \cdot U_N \quad (2.66)$$

Since cross section is proportional to T^2 , then

$$\sigma \propto A^2 U_e^2 U_N^2 \quad (2.67)$$

Calculation of U_N^2 requires knowledge of χ_f and χ_i . In the reflection approximation assumes that χ_f can be replaced by an appropriately normalised δ function [173, 176]

$$\chi_f = S \delta(R - R_c) \quad (2.68)$$

at the classical turning point R_c .

2.3.4 Angular Distributions of the emitted Fragments: Axial-Recoil Approximation

Since the collision time and the dissociation time are both small compared to the rotational time of the molecule, the fragments dissociate along the direction which the intermolecular axis had prior to the collision. This means that the trajectories of the fragments will indicate the orientation of the target molecule in space. Based on this idea, the so-called "Axial-Recoil method" has been developed and used to calculate the orientation of the emitted fragments [177, 178]. The probability of a transition to a specific dissociation state depends on the symmetry of the wavefunctions of the emitted ions and electrons [179]. This symmetry can be described by the orientation of the emitted fragments with respect either to the momentum change vector \mathbf{K} (where $\mathbf{K} = \mathbf{k}_f - \mathbf{k}_i$) or to the direction of the incident projectile \mathbf{k}_i . When the collision process exclusively induces dipole transitions, the cross section for the orientation of the emitted fragments is proportional to [180]

$$\sigma \propto |\mathbf{K} \cdot \mathbf{M}|^2 \quad (2.69)$$

where \mathbf{M} is the dipole matrix element for the transition to a dissociation state. *Zare et al.* [180] have discussed the transformation from $|\mathbf{K} \cdot \mathbf{M}|^2$ to the lab-system for the H_2 molecule. Applying their transformation, the angular distribution should be given by

$$I_\theta = B(\cos^2\theta\cos^2\eta + \frac{1}{2}\sin^2\theta\sin^2\eta) \quad (2.70)$$

where θ is the polar angle between one of the emitted fragments and the direction of the incident projectile. η is the angle between \mathbf{K} and the momentum vector of one of the emitted fragments. B is a constant which depends on the energy of the incident projectile.

2.4 Theoretical Models of the Slow Ion-Molecule Collisions

2.4.1 Modified Molecular-Orbital-Expansion Method

The molecular orbital expansion incorporating the *ETF* (electron translation factor) effect has been modified and employed by Kimura [75] to study the ion-molecule collisions. He has used this method to investigate the charge transfer in $H^+ + H_2$ collision in the energy range from 0.2 to 20 keV. Two-state semiclassical close-coupling calculations have been performed to examine the ion-molecule collision dynamics. The molecular states used as expansion basis have been obtained by using the diatoms-in-molecules (DIM) method (first proposed by Ellison [79]) as function of the internuclear distance R and two molecular orientation angles ϕ and θ . Fig. 2.10(a) displays the coordinate of the laboratory frame used by Kimura. The calculated adiabatic potential curves are shown in Fig. 2.10(b) for several values of θ with $\phi=0$. The figure indicates that for the ground state ($H^+ + H_2$), although molecular orientation effects are apparent for $R \leq 2$ a.u., the potential curves are essentially identical for $R > 2$ a.u., independent of molecular orientation. The same adiabatic curves calculated this time for various ϕ at fixed $\theta = 30^\circ$ are presented in Fig. 2.10(c). The differences in shapes of the potentials, corresponding to different values of ϕ are relatively small compared to the θ dependence shown in Fig. 2.10(b). He Also has found that the charge transfer cross section is very sensitive to the molecular orientation at energies below 0.5 keV and above 10 keV. An example of results is given in Fig. 2.10(d) and Fig. 2.10(e).

2.4.2 Orientation-Dependent Atomic-orbital Expansion

Shingal et al. [181] have studied single capture (*SC*) process in collisions of protons and He^{2+} with ground-state H_2 molecules for projectile energies ranging from 1 to 500 keV/amu. They have treated these ion-molecule collisions as an extension of the ion-atom collisions. In their model, the ground-state H_2 wavefunction was treated as a linear combination of the atomic orbitals from the two atoms. Thus, the electron-capture amplitude in ion-molecule collisions is expressed as the coherent superposition of two amplitudes in ion-atom collisions with the relative phase between the two amplitudes dependent on the collision velocity and the orientation

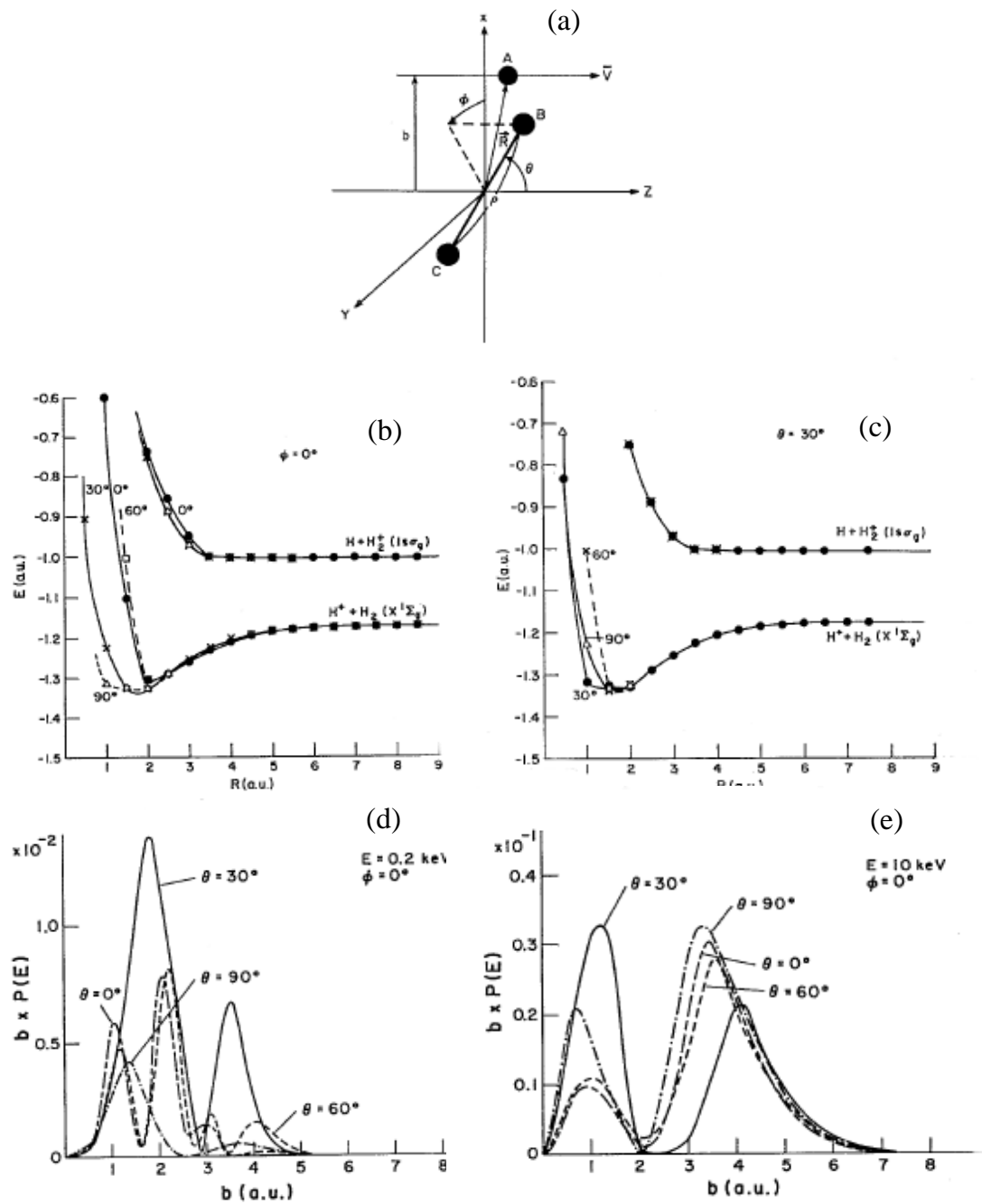


Figure 2.10: (a) Coordinate in the laboratory frame for the H^+-H_2 system. (b) Adiabatic potential curves as a function of internuclear distance R and angle θ with fixed $\phi=0^\circ$. (c) The same as (b) but angle ϕ with fixed $\theta=30^\circ$. (d) Probability times impact parameter versus impact parameter as function of θ at $E=0.2\text{ keV}$ and $\phi=0^\circ$. (e) The same as in (d) except $E=10\text{ keV}$.

of the molecule. They have calculated the cross sections for the SC process as a function of the impact parameter at a given orientation, i.e.,

$$\sigma(\theta, \phi) = \int_0^\infty bP(b)db \quad (2.71)$$

where $P(b)$ is the electron capture probability at a given impact parameter b . The total cross section can be calculated by averaging the cross sections obtained from Eq. 2.71 over all orientations as follows

$$\bar{\sigma} = \frac{1}{4\pi} \int \sigma(\theta, \phi)d\Omega \quad (2.72)$$

One of the calculations done by *Shingal et al.* [181] using method is presented in Fig. 2.11. They have investigated the orientation dependence (θ -dependence) of the single capture in the $p-H_2$ collision system. Fig. 2.11(a) displays the single capture probability times the impact parameter, i.e. $b * P(b)$ as a function of the impact parameter for a fixed $\phi=0^\circ$ at various angles θ for $E=10 \text{ keV}$. A weak orientation dependence of the capture probability can be determined. The θ -dependence becomes stronger for collision energy at 10 keV , as can be seen in Fig. 2.11(b). They found a strong orientation dependence for $E=200-400 \text{ keV}$, where the electron capture cross sections from the molecule parallel to the beam is 5-20 times less than from molecules oriented perpendicular to the beam. In the lower energy region, they have shown that the effect of molecular orientation is very small.

2.4.3 CTMC Model

Wood et al. [182] has developed the classical trajectory Monte Carlo Model to study double electron removal from H_2 by collisions with highly charged ions at impact energies range from 1 eV/u to 1 GeV/u. This model for ion-molecule collisions is an extension of that for ion-atom collisions described in section 2.2.1, with the exception that an additional target center is involved. This increases the complexity to a five-body problem. The Hamiltonian for the five-body system is

$$H = \sum_{i=1}^5 \frac{p_i^2}{2m_i} + \sum_{i=1}^4 \sum_{j=i+1}^5 V_{ij} \quad (2.73)$$

where p_i is the momentum of a given particle, m_i a particle's mass, r_{ij} is the distance between i and j , and V_{ij} is the potential between i and j . Each electron is initially bound to its parent atomic center by the Coulomb force and has no dependence on the other nucleus or the other electron. The two atom molecule is held together by a Morse potential [183]

$$V_m(R) = D_e(1 - e^{-\beta(R-r_e)})^2 \quad (2.74)$$

Where D_e is the dissociation energy, R is the separation of the atomic centers, and r_e is the separation defined such that $V_m(r_e)$ is a minimum. The values for

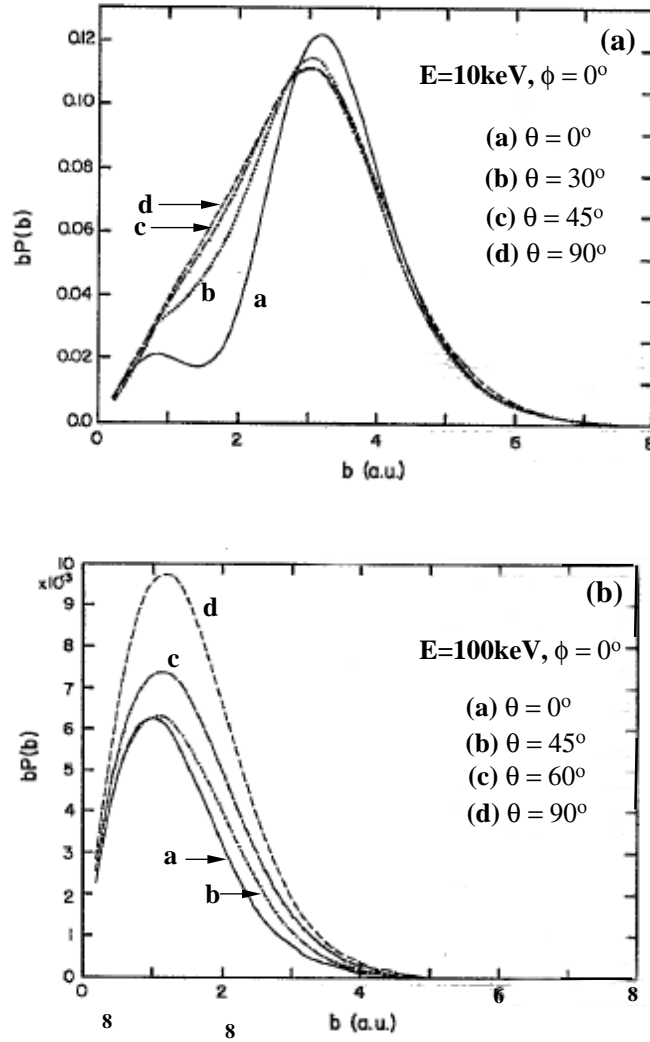


Figure 2.11: (a) Probability times impact parameter as a function of impact parameter at 10 keV, $\phi=0^\circ$, and (a) $\theta=0^\circ$, (b) $\theta=30^\circ$, (c) $\theta=45^\circ$, (d) $\theta=90^\circ$. (b) Probability times impact parameter as a function of impact parameter at 100 keV, $\phi=0^\circ$, and (a) $\theta=0^\circ$, (b) $\theta=45^\circ$, (c) $\theta=60^\circ$, (d) $\theta=90^\circ$.

$D_e = 4.7$ eV, $R_e = 1.40$ a.u., and $B_e = 0.73$ a.u. are determined from spectroscopic data [183]. To extend the *CTMC* method to the H_2 molecule, additional quantities must be generated for the position and momentum of both atomic centers. It is assumed that the molecule is in the ground vibrational state with a separation distance selected randomly from its vibrational Gaussian squared distribution. The distribution is centered about the minimum of the potential well ($R_e = 1.4$ a.u.) of the Morse potential. This implementation is necessary to obtain the correct *Frank-Condon* energy distribution of the dissociating protons for the isolated molecule. The electrons are placed on the atoms as described for this simple hydrogenlike case [85], with the ionization potential for each electron set equal to 13.6 eV. The

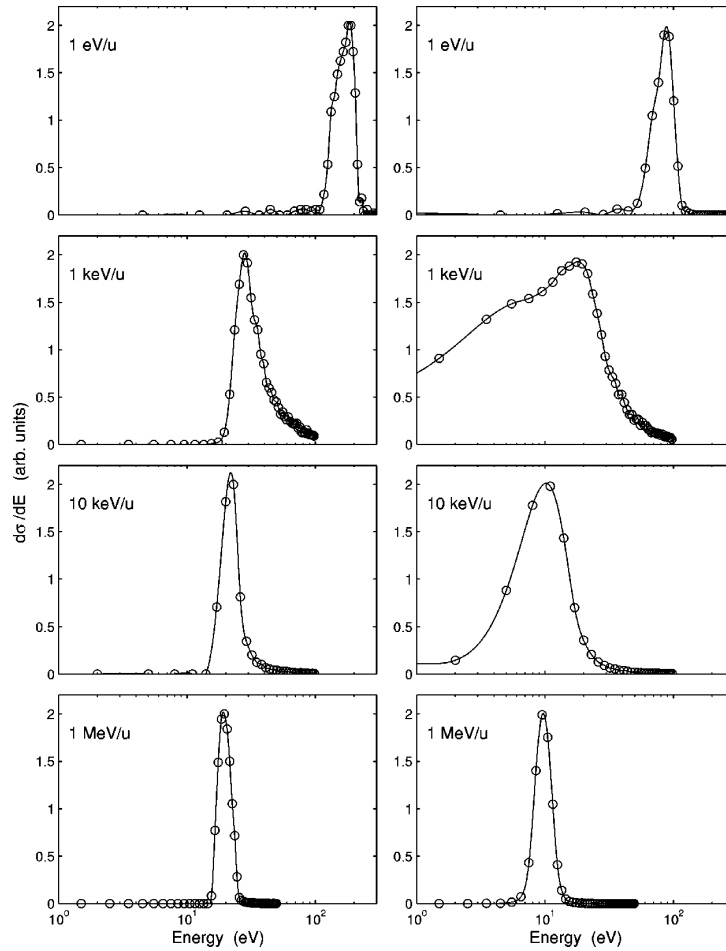


Figure 2.12: Energies of the protons after double electron removal by Xe^{54+} . The left-hand side represents the total energy of both ions, and the right-hand side represents energies of a single ion.

molecular axis is randomly oriented at the start of each trajectory. To investigate the properties of the energy and momentum spectra of the fragments, using this model, simulations have been made for the $Xe^{54+} + H_2$ collision system over a broad range of impact energies. The results are shown in Fig. 2.12.

The left-hand side of Fig. 2.12 is the distribution for the sum of the energies of both H^+ ions, and the right-hand side is the energy distribution for individual H^+ ions. The figure shows that the total energy sum of the two ions increases as the collision energy decreases. The high energy protons produced from impact at 1 eV/u are due to a large collisional transfer of energy to the target from the projectile. In essence, this is a three-body Coulomb explosion between the positively charged heavy ions since the collision time is quite extended. The extent of the Coulomb

explosion is not as large as given by the simple ratio of the projectile to proton charges, since in these slow collisions the impact parameter range is extended to almost 40 a.u.. As the impact energy increases and the collision decreases, less energy is collisionally transferred to the target and the total energy approaches the *Frank – Condon* transition energy of the isolated molecule, 19 eV.

2.5 Zero-Ranged Potential Model (*ZRP*-Model)

In their theoretical investigation of the saddle-point electron emission, Burgdörfer et al. [184] have introduced a new model referred to as Zero-Range potential model (δ -potential). Exact differential ionization probabilities have been calculated for inelastic ion-atom collisions in one dimension with interaction potentials of zero range. The δ -potential employed in their calculations is of interest for two reasons [185]. First, it is one of the few exactly solvable quantum-mechanical three-body problems. It therefore allows the exploring of three-body effects without distortions owing to approximations. Second, zero-ranged potentials represent, to a certain extent, the opposite extreme to long-ranged Coulomb forces. Therefore, this model permits the identification of features specifically related to interactions at short distances. According to this method, the time dependent "electronic Hamiltonian" for 1D δ -potential is given by

$$H_{1D} = -\frac{1}{2}\frac{\partial^2}{\partial Z^2} - Z_T\delta(z) - Z_P\delta(z - vt) \quad (2.75)$$

In this equation, the target frame has been adopted. Z_p and Z_T are the projectile and target nuclear charges. v is the velocity of projectile. As usual, the internuclear potential has been neglected since it gives rise to an irrelevant phase factor in the wave function within a constant-velocity approximation. The corresponding Hamiltonian for the 3D δ -problem is given by

$$H_{3D} = -\frac{1}{2}\nabla^2 - Z_T\delta(\mathbf{r}) - Z_P\delta(\mathbf{r} - vt\hat{z}) \quad (2.76)$$

where the projectile trajectory is restricted to zero-impact parameter (head-on) collisions and it is understood that $\delta(\mathbf{r})$, when applied to the wave function, takes the form [186] $[\delta(r)\delta(\cos\theta)\delta(\phi)/r^2][\partial[r\psi(r)]/\partial r]$. In each case, the initial state is assumed to be a $1s$ -like bound state of the target. A new feature has been observed in the electron momentum distribution calculated by Wang et. al. [185]. This feature clearly visible in Fig. 2.13 is a sequence of higher-order binary encounter peaks and dips at higher velocities in both the forward and backward directions. The ordinary binary encounter peak is located at $k=2v$ and results from a single head-on collision between the target electron and the projectile described by a first-Born approximation to the transition operator

$$T^{(1)} = V_P \quad (2.77)$$

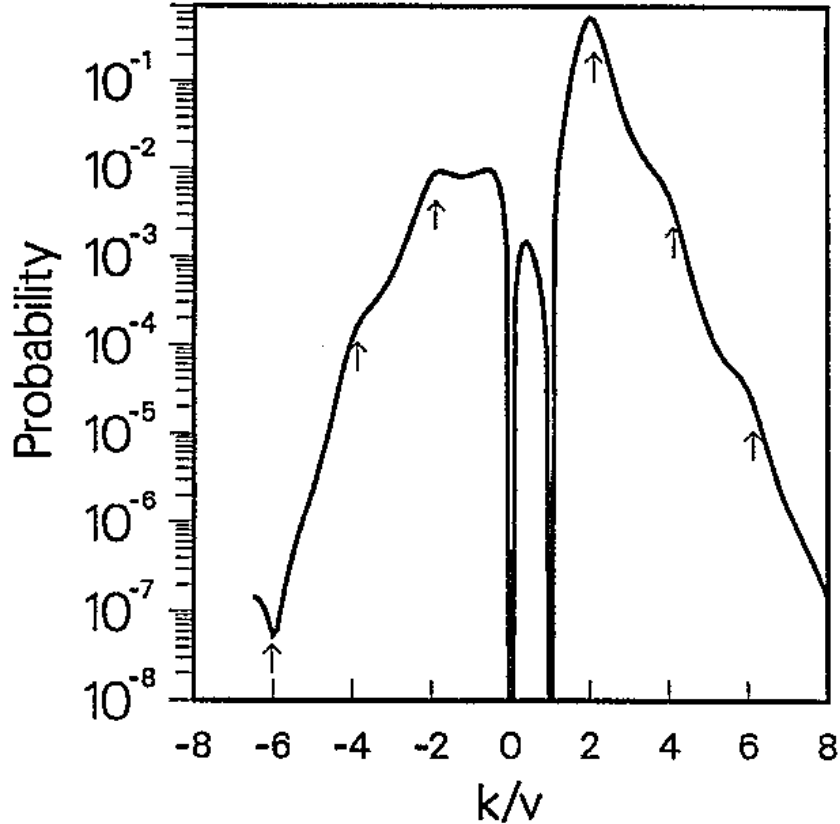


Figure 2.13: $Z_P/v=5$, $Z_T/v=5$, the expected positions of resonance structures [Eq. 2.78] are marked by arrows.(adapted from [185])

with $V_P = -Z_p\delta(z - vt)$ the electronic interaction with the projectile. The prominence of the binary encounter (BE) peak for ion-atom collisions with δ potentials results from the fact that hard collisions are dominant for short-ranged potentials. The peak observed at $k = -2v$ corresponds to backward scattered BE electrons having suffered another hard collision with the target. Subsequent head-on collisions alternately with the projectile and the target lead to a sequence of resonant structures in the forward and backward direction at momenta

$$k = \pm 2nv \quad (n = 1, 2, \dots) \quad (2.78)$$

with rapidly decreasing amplitude. They originate from partial amplitudes T^{2n-1} in forward direction and T^{2n} in backward direction of the Born series. The resonant structures are either peaks or dips depending on the relative sign of these multiple knock-on amplitudes and the first-order amplitude they interfere with either constructing or destructively. Since the multiple knock-on process involves simultaneous collisional interactions with both the target and the projectile they are intrinsic three-body scattering effects. The sequence of multiple scattering peaks [Eq. 2.78] has a classical analog in the **Fermi Cosmic-ray acceleration model** [187] of a

ball bouncing back and forth between a moving and a stationary wall.

Very recently, *Macek et al.* [188] have computed the electron distributions in ion-atom collision system for both high and low ion velocities using this model. In their calculations, the exact solution have been express in the terms of g and u Sturmain functions. Distributions at low velocity exhibit *Fermi* acceleration peaks due to interference between g and u amplitudes. The exact electron distributions corresponding to g and u states at low velocity $v \approx 1$ are shown in Figs. 2.14(a) and 2.14(b). For g state, there is just one peak centered at $\mathbf{k}=\frac{\mathbf{V}}{2}$ and a small ridge at $k \approx 7 a.u.$. For u state, There is a node at the midpoint owing to symmetry requirements where two separated peaks are emerged. In Fig. 2.14(c) shows the distribution corresponding to an electron initially in the projectile. This distribution exhibits a main peak at the midpoint. In addition, there is a series of interference features. Because the g and u distributions are smooth, it is apparent that the oscillations in the representation are due to interference between the g and u amplitudes. Furthermore, the oscillations in the forward and backward directions are out of phase since the peaks are at $(2n-1/2)v$ in the forward direction and at $(2n+1/2)v$ in the backward direction. Such peaks are attributed classically to *Fermi* acceleration where the electron bounces back and forth between the target and the projectile.

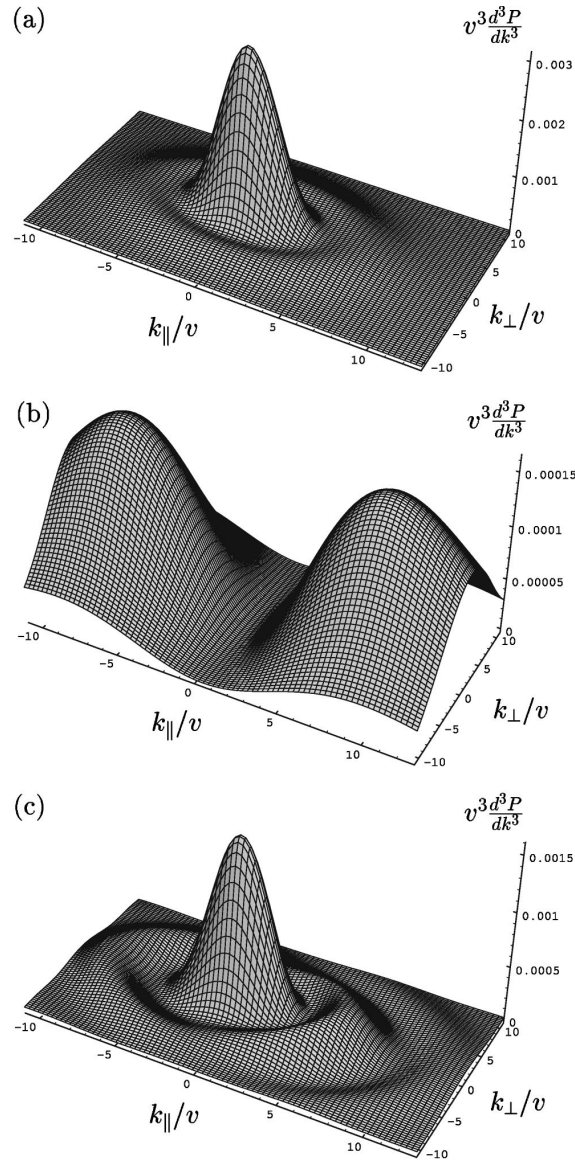
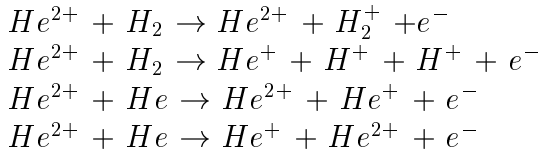


Figure 2.14: Electron distribution $v^3 d^3P/dk^3$ vs k/v for $v=1$ a.u.. Distributions corresponding to (a) gerade and (b) ungerade symmetry and (c) the distribution corresponding to an electron initially in the projectile are shown. Out of phase oscillations corresponds to Fermi acceleration.(adapted from [188])

Chapter 3

Experimental Setup

The schematic of the experimental setup is shown in Fig. 3.1. The experiment was performed at the IKF-ECR facility in the university of Frankfurt. It is a very powerful ion source capable of producing highly charged ions with energy up to 45 keV per charge. The incoming beam was collimated to beam spot of less than 1 mm² by two pairs of collimators. The beam intersected a supersonic gas jet. Ejected electrons and recoil ions produced in the target region were extracted and accelerated in opposite directions toward position-sensitive-multi-channel-plate detectors by an electric field. Both detectors were oriented perpendicular to the beam. Meanwhile, the projectile ions were charge-state- analyzed and directed onto a third position-sensitive detector except the main beam which was deflected after penetrating the target and dumped into a Faraday cup. Using standard coincidence techniques the following reactions



are investigated and their products are detected in time coincidence.

3.1 ECR beam line

The ion source installed in this beam line is a 14.36GHz *ECR* (**E**lectron **C**yclotron **R**esonance) ion source. Detailed descriptions of the ion source have been published [189]. Generally speaking, the mechanism for producing positive charge ions inside an *ECR* ion source is electron impact ionization. In order to create highly charged ions, two conditions must be met. First, the target ion has to be impacted by energetic electrons many times, because usually only one electron will be removed from a target ion in a single ionization. Second, the electrons need to be energetic, because the binding energies of target electrons are higher for the inner shell electrons. For an *ECR* ion source, the first requirement is met by confining electrons

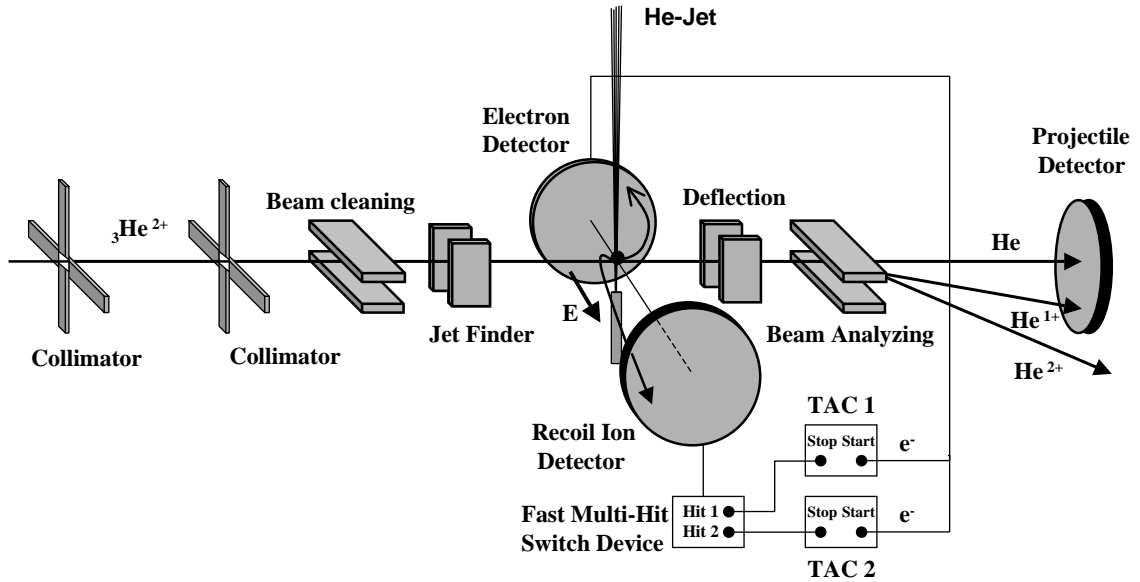


Figure 3.1: Schematic sketch of the experimental setup illustrating the geometry of the three two-dimensional position sensitive detectors (2d-psd) for triple coincidence between the ejected electrons, recoil ions and projectile ions.

and ions in a volume by magnetic fields. The magnetic field used on an *ECR* ion source is a combination of a radial field with an axial field. The magnetic field strength is a minimum in the center of the plasma chamber and increases in every direction from the center, a so called "minimum B- field" configuration. For this ion source, the radial field is obtained from *hexa-* pole- permanent magnets. The axial magnetic field is supplied by two water cooled solenoid coils. The mirror ratio is the ratio of the maximum field strength at the magnetic mirror to the field strength at the center of the source. The higher mirror ratio, the better plasma confinement is, and the better the chance to produce highly charged ions. The second condition to produce highly charged ions is met by injecting 14.36 GHz microwave into the plasma chamber to heat up electrons. Electrons are accelerated or decelerated by the electric field component of the microwave and are performing cyclotron motion around the magnetic field lines inside the source. Once the electron cyclotron frequency is equal to the electric field oscillating frequency (microwave frequency), the electronic cyclotron motion becomes resonant (*ECR*). The intensity of the output ion beam increases with the injected microwave power. A positive voltage (extraction voltage, V_{extr}) which can go up to 45keV is applied on the plasma chamber; the rest of the beam line is at ground potential. An ion which loses its axial confinement sees the potential difference between the plasma chamber and the beam line. It will follow the field and be accelerated out of the source with energy of $(Q * V_{extr})\text{keV}$.

3.2 Target

High resolution recoil ion momentum spectrometer is based on well localized inherently cold targets ensuring a perfect preparation of the initial target momentum, i.e., the initial target motion (the initial target temperature) has to be strongly reduced so that the target is well localized in the direction of the projectile.

3.2.1 Supersonic Gas Jet

In the recoil- ion spectrometers a well localized atomic or molecular target is generated exploiting the features of quasistatic adiabatic (i.e. isentropic) supersonic expansion of the gas target. This method of producing atomic beams was first proposed by Kantrowig and Grey [190]. In this case a dense gas is allowed to expand through a very narrow nozzle. The condition in this limit is that

$$d \gg \lambda \quad (3.1)$$

where d is the diameter of the *container's aperture*, the λ is the mean free path of atoms in the source (container). This results in many inter-atomic and atom-wall collisions before the particles escape the nozzle. These conditions result in thermal cooling of the particles in which the random motion is converted into directional energy in the direction of flow. The jet envelope is elliptical in shape with the long axis in the direction of the gas flow. This shape is due to the superposition of the directional velocity of the jet and the random effusive velocity. The expanding gas is then skimmed in one or two stages in order to (a) add more directionality to the atom beam, (b) throw away the slower part of the jet envelope, and (c) reduce the number of the scattered particles in the collision chamber. Usually, the skimmer has a conical shape which contributes in reducing the effect of scattered particles on the gas- jet flow through the orifice.

In our experiment, 2-stages supersonic gas jet is used to produce a well geometrically defined and localized gas jet. This supersonic gas jet is produced by allowing the He gas (or H_2) at a pressure of 17 bar and at the room temperature to expand upward through a $30\mu\text{m}$ nozzle into a first vacuum chamber. After the expansion, the atoms move with a momentum of p_{jet}

$$P_{jet} = (5 * k * T_o * M_R)^{1/2} \quad (3.2)$$

which is about 5.9 *a.u.* for helium at $T_o = 300\text{ K}$. The jet then passes through a 0.22 *mm* skimmer into a second vacuum chamber. The pressure in this stage is about $3 * 10^{-5}\text{ mbar}$. The inner jet fraction passes through another skimmer of 0.7 *mm* into the collision chamber yielding an atomic beam with a diameter of 1.1 *mm* at the intersection point with the projectile beam. The target chamber is maintained at a pressure of $2 * 10^{-8}\text{ mbar}$. Finally the jet is collected by an evacuated catcher on the opposite side of the target chamber.

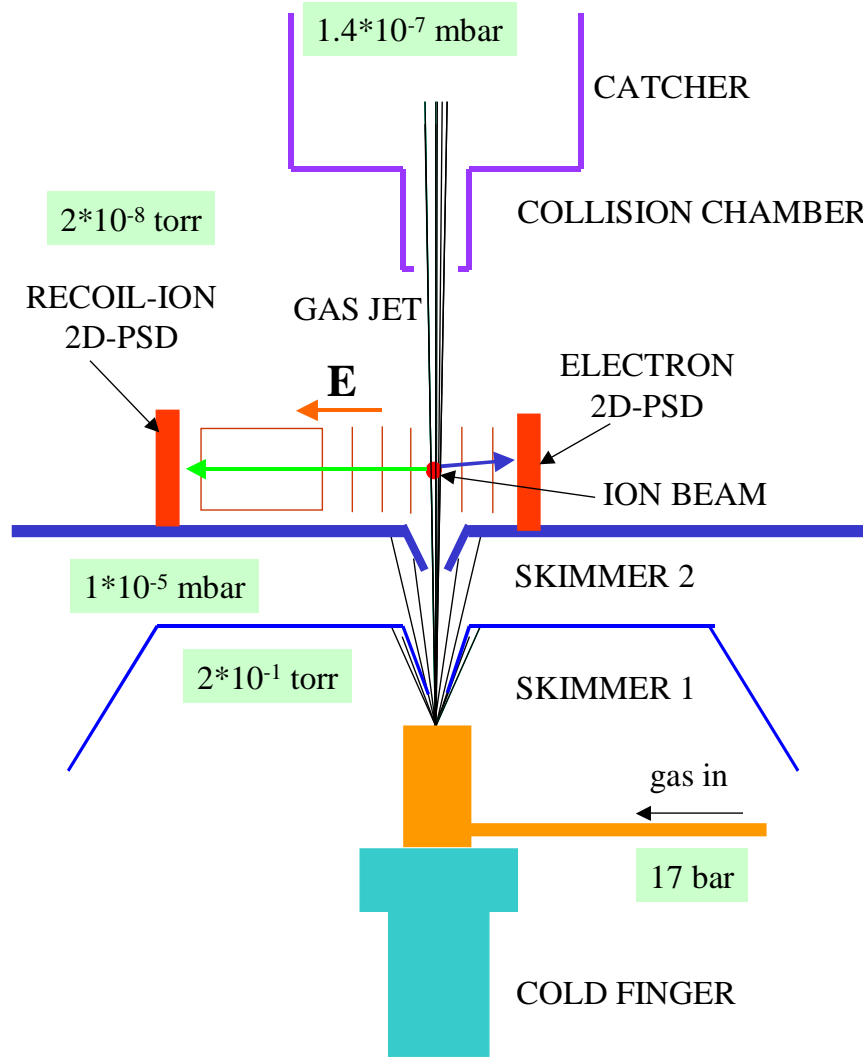


Figure 3.2: Schematic representation Of COLTRIMS apparatus.

The actual quality of the jet is expressed by its speed ratio

$$S = (5T_o/2T)^{1/2} \quad (3.3)$$

where T is the leftover internal jet temperature after the expansion. The speed ratio of our jet system is about 40. Thus accordingly to eq. 3.3, the jet has an internal temperature near $0.1 K$ which corresponds for He to a momentum spread of $0.07 a.u.$. The Target density is estimated about $4.5 * 10^{11} cm^{-3}$ at the intersection point in the target chamber. This density corresponds to a target surface density of about $5 * 10^{10} cm^{-2}$. The exact dimensions of the jet system is shown in Fig. 3.2.

3.3 Reaction Microscope: Momentum spectrometer

The next challenging important task was to find field configurations which guide particles with different masses (electrons and ions) and energies toward the position sensitive detectors. The program *SIMION* [191] allows us to do very accurate representation and simulation of the electrostatic system (spectrometer) used to achieve a projection of these very different particles. The schematic of a coincident momentum space imaging spectrometer used in our experiment is shown in Fig. 3.3. The spectrometer consists of two main parts; the electron spectrometer and the recoil ion spectrometer. A high acceleration field was used in order to detect the fragments resulted from the dissociation of the H_2 molecule; $E= 13 V/mm$. This electric field has been produced using two power supplies connected to the ends of the spectrometer. This generates a potential difference between the two ends of the spectrometer. This potential has been distributed on the electrodes of the spectrometer by a chain of resistors.

3.3.1 RIM spectrometer

All *COLTRIMS* spectrometers used with supersonic gas jet targets apply a projection technique. An electric field guide recoil ions from the reaction zone (the small overlap volume of the gas jet with the projectile beam) onto the position sensitive detector. From the position and *TOF* of ions, the momentum of the recoil ion can be calculated. In *RIM* spectrometers which exploit homogeneous electric fields only, the momentum resolution in the two dimensions perpendicular to the electric field is determined by the extension of the interaction volume and the ion time of flight. To circumvent these restrictions of the extended reaction volume, we have used an electrostatic focusing lens in the extraction field. The detector is placed in the focal point, so that ions created at slightly different positions but with the same momentum vector hit the detector at the same position. The implementation of a lens in the extraction field, however, changes the focusing properties in the time-of-flight direction. Thus, lens and length of the drift region have to be adjusted such that the focus length for the *TOF* and the special focusing by the lens coincide. In general, the implementation of a lens requires a longer drift region compared to a spectrometer with homogeneous fields.

As mentioned above, the three-dimension focusing (i.e. the time and position focusing) can be achieved by using the lens in the acceleration region together with the drift region. To optimize the properties of the spectrometer, the relation between the length of the drift region and the focusing of the lens has been derived as follows: the acceleration field of the spectrometer can be divided into three separated field regions. The first region extends from the target position to the lens in the acceleration region and has a distance s_1 . The second region lies between the lens and the grid used to separate the acceleration region from the drift region. The region has a distance s_2 . In these both regions the acceleration field is homogeneous. The

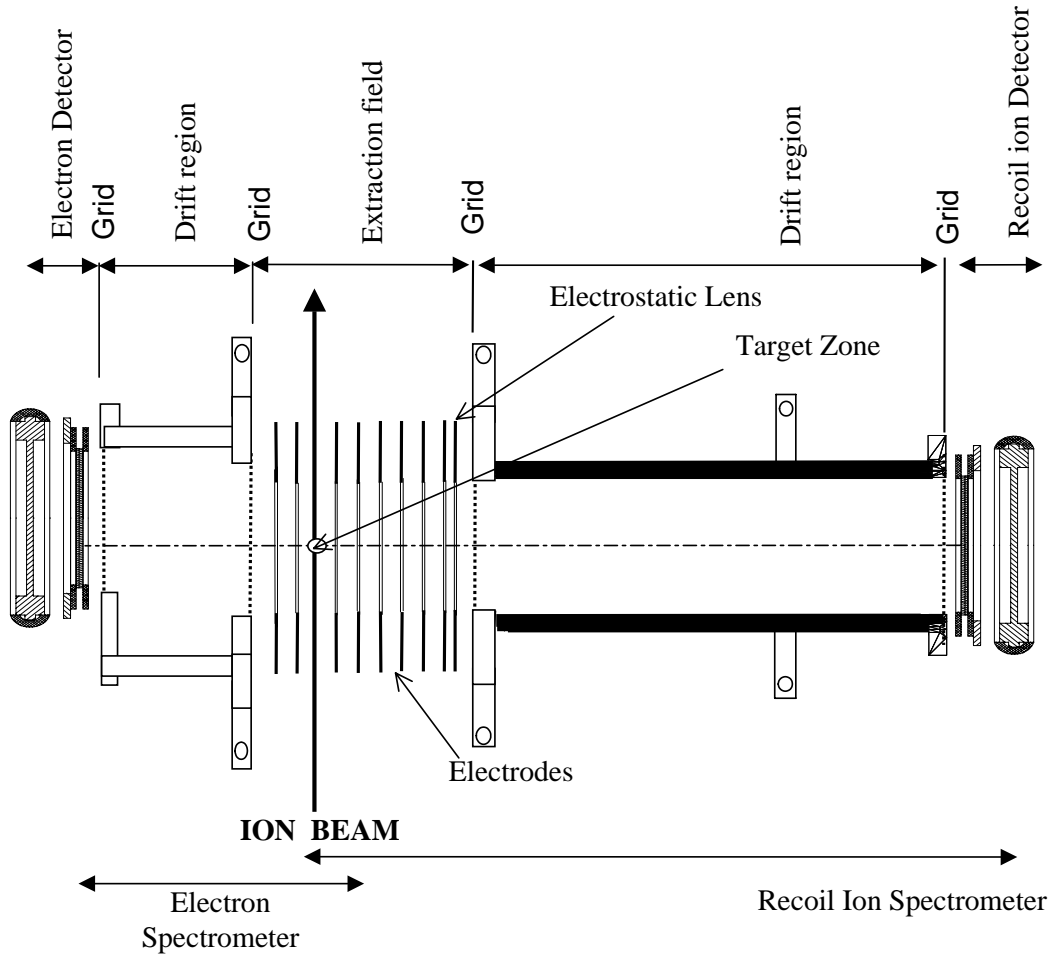


Figure 3.3: Schematic of a coincident momentum space imaging spectrometer used in the present work.

third region which represents the lens is an imaginary region and has a distance s' obtained from the following equation

$$s' = \frac{U_L}{E} \quad (3.4)$$

where U_L is the lens voltage and E is the field intensity at $U_L=0$ V. The length of the Drift region can be defined by s_d . The time of flight t_1 , in which an ion with zero initial momentum can cross the distance s_1 , is

$$t_1 = \sqrt{\frac{2s_1}{a}} \quad (3.5)$$

where a is the acceleration of the ion. And it needs the time t_2

$$t_2 = \sqrt{\frac{2(s_1 + s')}{a}} \left(\sqrt{1 + \frac{s_2}{s_1 + s'}} - 1 \right) \quad (3.6)$$

to cross s_2 and t_d

$$t_d = s_d \sqrt{\frac{1}{2a(s_1 + s_2 + s')}} \quad (3.7)$$

to cross the drift region. Therefore, the total time of flight of the ion till it reaches the detector is the sum of all previous time of flights, i.e.,

$$t = t_1 + t_2 + t_d = \sqrt{\frac{1}{a}} \left(\sqrt{s_1} + \sqrt{s_1 + s_2 + s'} - \sqrt{s_1 + s'} + \frac{s_d}{2\sqrt{s_1 + s_2 + s'}} \right) \quad (3.8)$$

To calculate the length of the drift region which fulfills the time focusing condition, Eq. 3.8 has been differentiated to s_1 , because the time of flight of the ions, which start from different positions in the target volume with the same initial momentum, should be independent on the start position. This means

$$\frac{\partial t}{\partial s_1} = 0 \quad (3.9)$$

The differentiation leads to

$$s_d = 2(s_1 + s_2 + s') \left(1 + \sqrt{\frac{s_1 + s_2 + s'}{s_1}} - \sqrt{\frac{2s_1 + s'}{s_1 + s'}} \right) \quad (3.10)$$

This equation (Eq. 3.10) gives the length of the drift region which satisfies the focusing conditions. The initial conditions for the spectrometer which does not contain a lens are $U_L = 0$ V and $s'=0$ mm. Under these conditions and using Eq. 3.10, the length of the drift region, which meets the focusing conditions, is $s_d = 2(s_1 + s_2)$. In order to adjust the properties of the lens, i.e the voltage, used in the present work, a changable resistance has been connected to the electrodes formed the lens. This resistance has been placed outside the chamber to enable us to control it during the experiment.

Fig. 3.4 shows a simulation of the ion spectrometer part. This figure demonstrates the time and position focusing. Three groups of ions with energy of 10 eV have been generated in three different directions: $\theta = -90, 0, +90$ (where θ is the angle between the ion momentum vector and the axis of the spectrometer). Each group consists of three ions which start from different positions in the reaction zone. The used spectrometer shown in Fig. 3.4 focuses an extended target zone of 1.1 mm to a focus spot of below 0.1 mm on the detector.

3.3.2 Electron spectrometer

The same electric field which guides the positively charged ions to one direction accelerates the electrons in the opposite one. Electrons produced during the collision

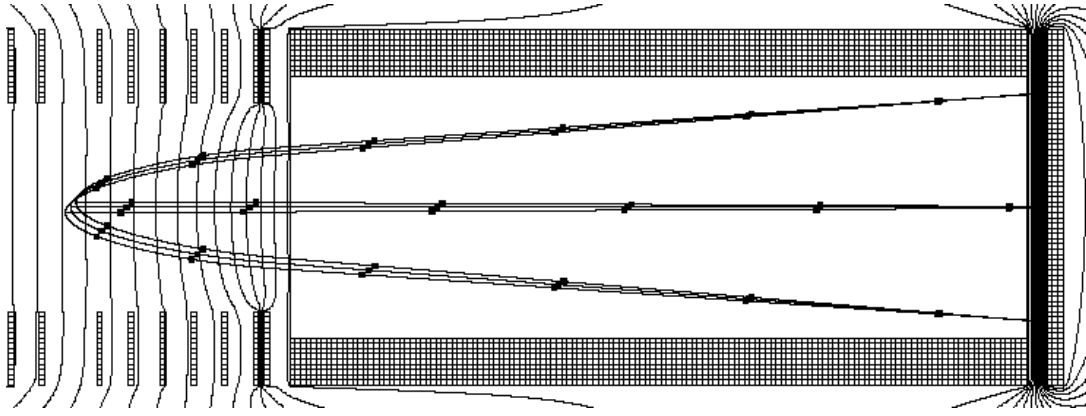
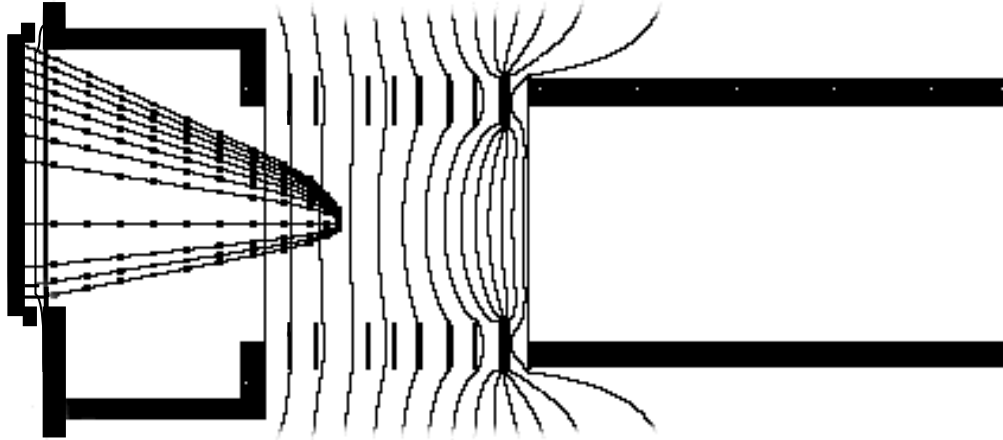


Figure 3.4: Field geometry in the recoil-ion part of the spectrometer with three-dimensional focusing properties. The three groups of trajectories result from ions starting from different positions (represent the extension of the gas target) with different directions (for more details see in text). Time markers of ions are at 100 *nsec*.

were accelerated over a distance of 15 *mm*. Then they traveled a distance of 40 *mm* in a field free region and were detected by another positive sensitive detector. A small negative bias voltage was put on the top of the first channel plate to repel stray electrons which are mostly very slow electrons. Because we know from the first measurements that electrons are emitted forward with the projectile due to the postcollision interaction between them, the electron detector is shifted about 12 *mm* in the direction of the projectile in order to get more active surface. Fig. 3.5 shows the trajectories of electrons which started in perpendicular to the beam direction with energies: 0.2, 0.4, ..., 1.6 *a.u.* in the upper half and 0, 0.1, 0.3 *a.u.* in the lower half. Without a magnetic field a 4π detection solid angle has been achieved only for the electrons with momenta transverse to the extraction field below 1.7 *a.u.* in the forward direction. No resolution has been obtained along the direction of the extraction field due to the missing explicit time-of-flight measurement for the electrons. Assuming a constant *TOF* for all electrons, two of the three momentum components of the electrons were calculated from the electron impact position on the electron detector. An electron with initial momentum of 0.2 *a.u.* directed parallel or anti-parallel to the field yields about a 7.3% change in the electron time of flight and thus a similar error in momentum components transverse to the field calculated from the electron position.

3.4 Position Sensitive Dectectors

For recoil ion and electron momentum imaging Position-Sensitive-Detectors (*PSD*) which combine good position resolution (typically 0.1*mm*) with good time resolution (1 *nsec*) are essential. Channel-plate detectors with delay line position encoding have



SIMION

Figure 3.5: Field geometry in the electron spectrometer. For illustration: in the upper half, 8 electrons with energy 0.2, 0.4,..., 1.6 a.u. are projected on the electron detector in direction transverse to the spectrometer axis ($\theta = 90^\circ$). In the lower part, 4 electrons with energy 0, 0.1, 0.2, 0.3 a.u. are projected onto the detector with ($\theta = -90^\circ$). Time markers of electrons are at 1 nsec.

been widely used for this purpose. For imaging purpose chevron (two plates) or z-stack (3 plates) configurations of 48 mm diameter are used. The ions are typically accelerated by 2000 V onto the surface of the channel plate. For electrons, maximum efficiency is reached at about 200-300 eV. A typical pulse height distribution from a channel-plate z-stack and the detection efficiency of He^{1+} ions as function of the acceleration voltage are shown in Fig. 3.6(a) and Fig. 3.6(b).

A delay-line position readout for channel-plate detectors has been suggested by *Sobottka* [192]. The delay-line-anode is composed of two crossed double wire planes spirally wound over a copper plate where they are held with ceramic holders fixed on the edges of the copper plate in order to isolate the wires from one another and from the copper plate. The distance is about 1 mm between the wire planes and 1 mm between the copper plate and the near wire plane. Each wire plane consists of a pair of wires with nearly 0.5 mm distance to separate them from each other (see Fig. 3.7). By a potential difference of 50V between the two wires the electron avalanche produced by an ion hitting the *MCPs* are collected by only one of the wires. The wire pair acts as a lecher cable. At both ends of the double wire spiral the signals are processed by a differential amplifier. Both wires pick up the same capacitively coupled noise, but their signals differ by the real electrons from the charge cloud collected by the more positively biased wire. These differential amplifiers yield extremely low noise signals. The time differences between a start signal, picked at front or back of the channel plate, and the two signals from both ends of the wire pair are measured with two time-to-digital converters. The time

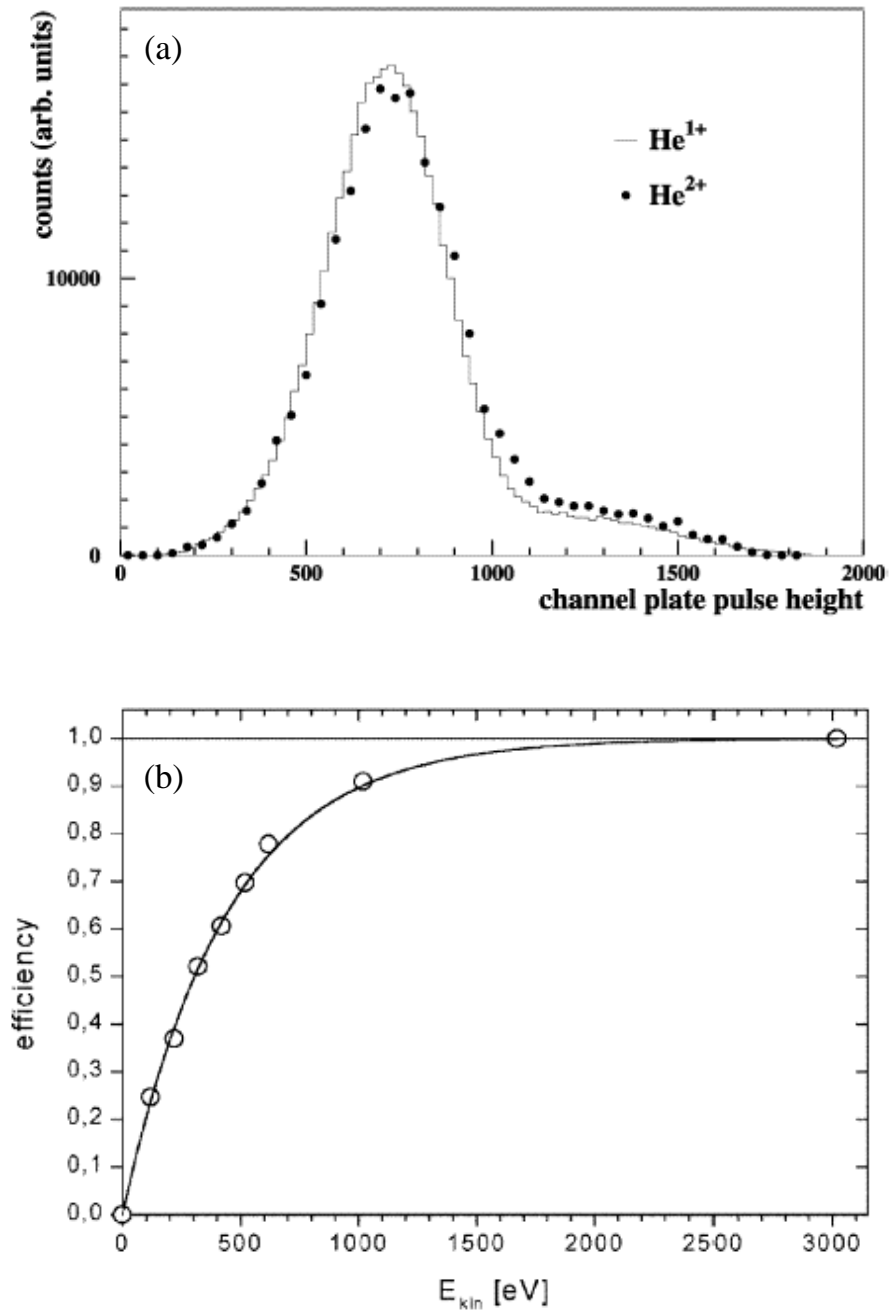


Figure 3.6: (a) Pulse height distribution for He^{1+} and He^{2+} ions on a z-stack channel-plate detector (i.e. three plates). The ions hit the detector with an energy of $3000\text{eV}\cdot q$ (adapted from [124]). (b) Relative detection efficiency of a z-stack pf channel plate for He^{1+} as a function of the extraction field toward the surface of the detector. The curve is arbitrarily normalized to 1 at 3000eV (adapted from [110]).

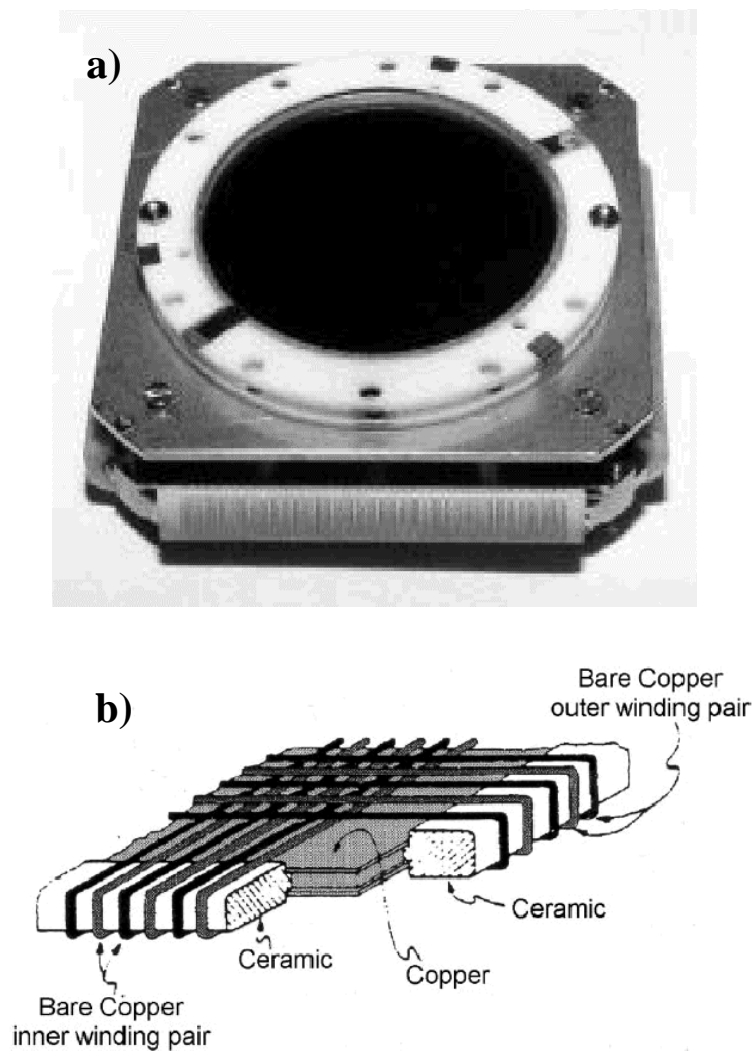


Figure 3.7: Delay-line anode for multi channel plate position read out. The inner and outer winding pair are for x and y encoding.

difference is proportional to the position respective direction. Depending on the *TDC* used a position resolution of better than 0.1mm can be achieved.

3.5 Multi-Hit System

3.5.1 Multi-Hit-line-Anode

The delay-line detector and the delay-line wire system can in principle detect and separate the signals of two recoil ions impinging on the detector in a very short time difference within the limited time resolution of the system (50 ps) if they hit at different positions. Whether the *TOF* and position for both fragments can be

determined, depends only on the electronics used. With commercially standard fast timing modules we were able to separate recoil impacts which were separated by a time delay of more than 5 ns . In order to do that, a fast switch device was built as shown in Fig. 3.8. A delay-gate signal is created from the first pulse (5 ns delay and $1\text{ }\mu\text{s}$ gate). The direct signal and the delayed gate signal are fed into a logical "And" gate "overlap coincidence". From this unit one obtains a timing- signal for the second pulse. More similar circuits can be added to allow the processing of a third and fourth multi-hit. The time to resolve two consecutive signals is presently limited to 5 ns . This limit comes from the limited pulse length of the electronic modules used.

3.5.2 Multi-hit-TDC (Lecroy TDC 3377)

This multi-hit *TDC* has 32 channels and can process 16 hits per channel separated by at least 10 ns in time with a time resolution of 0.5 ns (for more details, see appendix A). If two recoil-ions hit the detector within 30 ns (i.e., the total signal processing time on the delay line), the x- and y-delay-line signals of the two particles interfere with each other. However, the sum of the corresponding arrival times for each ion on opposite ends of a delay-line is constant for a true event because the delay line has always a constant length for each signal pair. This information can be used to sort the signals of all the particles according to their arrival time and thus their position on the detector can be identified.

3.6 Signal Processing and Data Acquisition System

A block diagram of the electronics used in present work is shown in figure 3.9. The signals from the detectors are processed using a standard *NIM* electronic. Three-position-sensitive- delay-line-anode detectors are used to detect the reaction products. Each delay-line anode contains two pairs of low resistive wires, one pair in x- and the other in y-direction. The signal wire of each pair runs a little higher positive voltage than the reference wire, so that most electrons are collected by the signal wire (lecher cables). The signals are de-coupled from the *DC*-voltages on the wires/contacts (using *RC*-element) and then the difference between these signals is amplified by a differential amplifier. In order to get rid of noise, the signals are transmitted to a constant fraction discriminator converting them to standard *NIM* signals. These *NIM* signals are then converted to *ECL* signals by *NIM – ECL* converter and fed into the multi-hit *TDC*. The two dimensional position can be calculated by the signal arrival time at the ends of the two perpendicular wire pairs. To improve the position resolution the position is calculated from the time difference between the two ends. The sum of both arrival times is constant and can be used as a check. The timing signals are taken from every detector either from front or back sides of the *MCP* and then sent to Timing-filter amplifiers for

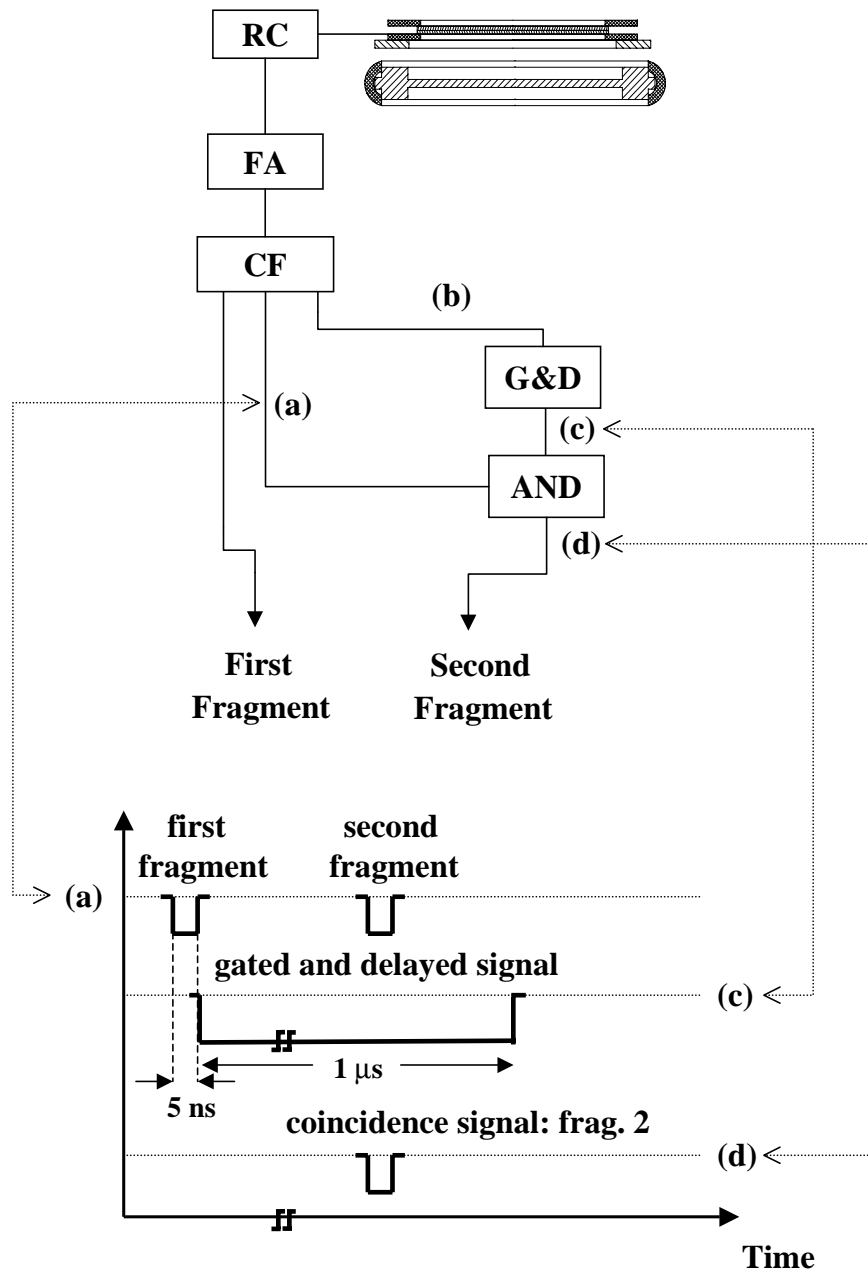


Figure 3.8: Fast multi-hit switch device used to direct signals consecutive in time from one output to separate TDC stop inputs. The above part shows the electronic diagram of the device. The different shorts have the following meaning: **RC**: RC-couple box, **FA**: Timing amplifier, **RC**: Constant fraction discriminator, **G&D**: Gate and delay generator. The lower part of the figure displays the time development of the signal processing in this device.

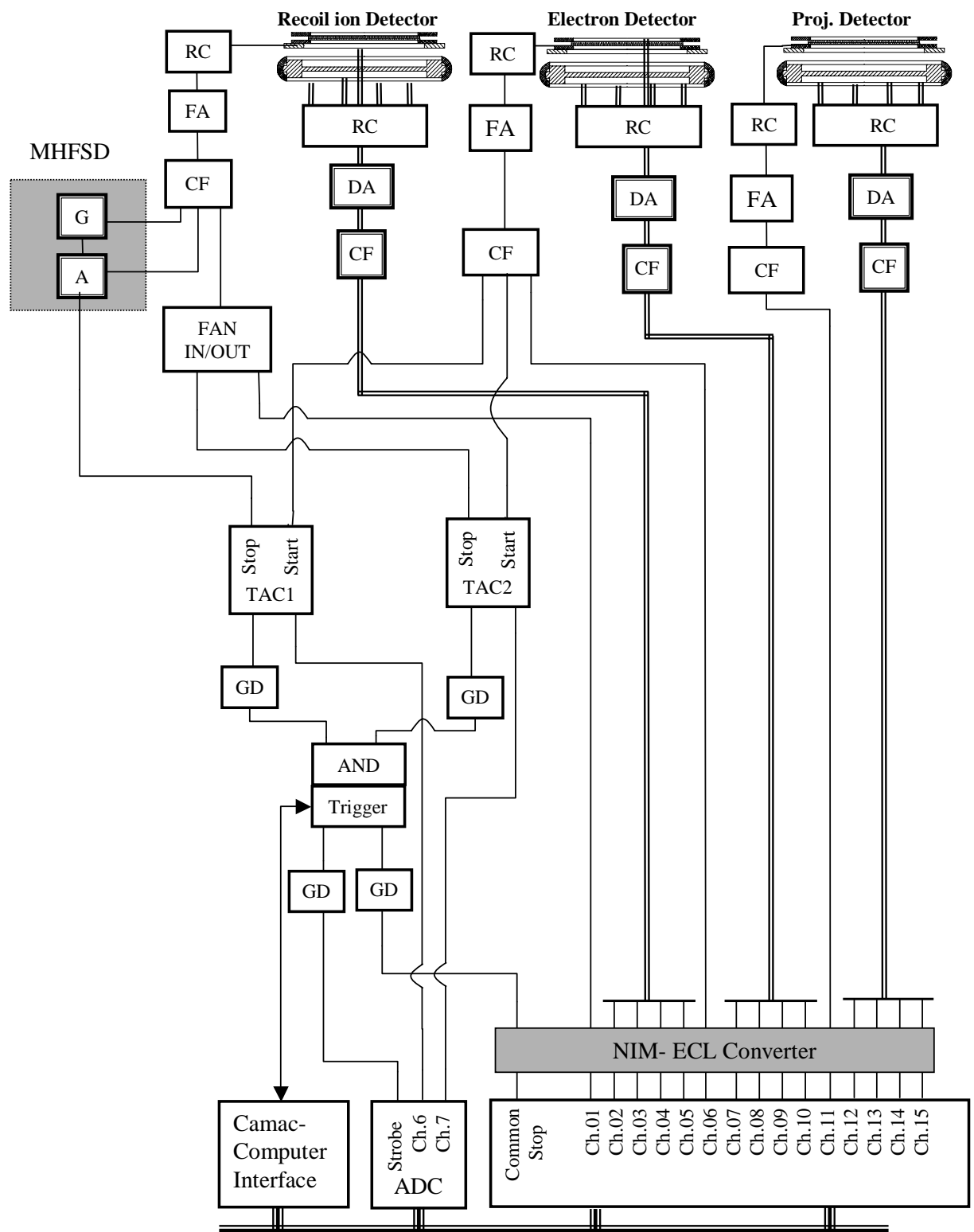


Figure 3.9: Block diagram of the electronic set-up utilized in the present work. See text for the abriviations.

further amplification and shaping. After that, the timing signals are processed with constant-fraction-discriminators (*CFD*). The outputs are converted to *ECL* signals using *NIM – ECL* converter and then read with the multi-hit *TDC*.

As mentioned above, the reaction products are detected in time coincidence using different coincidence modes. In order to realize that, two Time-to-Analog converters (*TAC*) are used as coincidence units. The time signal of electron detector is split into two similar signals which are then used to provide the start signals of the *TACs*. As stop signals, the timing signals of two fragments are used after separating them by the fast switch device described in 3.5.1. For every *TAC* there are two output signals; one corresponds to the time-of flight, the other is a trigger signal. In order to switch between the different coincidence modes in the experiment, a master trigger box is built using the Quad Coincidence Logic unit (*AND/OR* logic unit); Where the trigger signals of the *TACs* are fed into this box as selective inputs. So, for example, when the experiment should to be run in triple-coincidence mode (electrons, two fragments), the trigger signals of the both *TACs* have to be fed into the master box which is chosen to work in *AND* mode.

Finally, the data are taken in "event mode", i.e. the computer records the full momenta of all products for every event and correlation between momenta of collision products which can be examined later in the sorting of the data. The data can be presented not only in terms of individual particle momenta, but also in terms of collective or *Jacobi* coordinate. The PC-software used to control the read-out and event handling has been developed in our group and called *COBOLD* software [193].

Chapter 4

Data Analysis

Fig. 4.1 shows a conventional coordinate system that will be used in describing the results of this experiment. The beam direction is in the positive Z direction. The gas jet flows in the positive Y direction. The extraction electric field points in the negative X direction. Thus electrons are accelerated in the positive X direction while recoil ions are accelerated in the negative X direction. Two components of the recoil-ion momentum (P_z and P_y) are reconstructed from the position on the recoil ion detector (z and y). The same procedure applies to the projectile and electron detectors. Typically, the time-of flight of the electrons is about 11 nsec . The time of flight of the recoil ions is in the order of hundred *nano*-seconds. The spread in the time-of- flight of electrons was about 2.5 nsec . This made measuring the third component of the electron velocity unachievable. However, the time signals of the electrons was used to give the start signal for TAC which was stopped by the recoil ion signal, therefore resulting in measuring the time-of-flight of the recoil ions and hence their initial momentum in the X direction. Thus, the complete momentum vector of the recoil was determined.

4.1 calibration Of RI-spectrometer

As first step in the data analysis, the measured positions and times must be calibrated, i.e., the relation function between the direct measured quantities (positions and times) and momenta must be determined. Moreover, a reference point is needed for every momentum component. This reference point serves as momentum zero point. Calibration factors and reference points for the recoil ions and electrons must be found out for every momentum component.

In the longitudinal direction (Z direction), the capture reactions are used to determine both the momentum zero point and the calibration factor. Due to the energy- and momentum conservation, only discrete values of $P_{f,z}$ occur for pure electron capture corresponding to the projectile velocity and Q -value of the reaction:

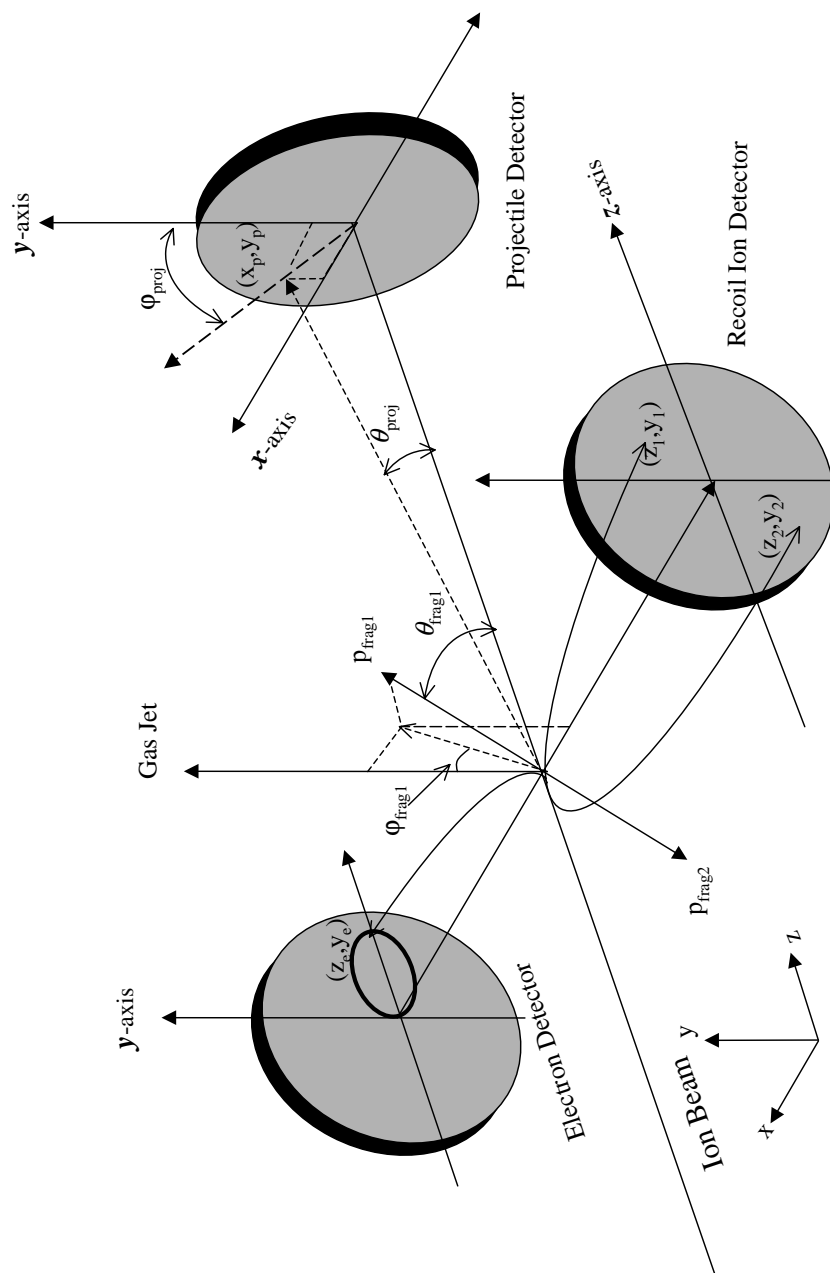


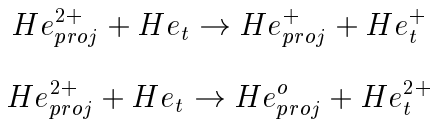
Figure 4.1: The coordinate system used in describing the results of the present work.

$$p_{||R}^f = \frac{Q}{v_p} - n_c \frac{v_p}{2} \quad (4.1)$$

where Q -value is the change in inner electronic energy of the projectile and the target, i.e., the energy difference between initial and final bound electronic states as follows:

$$Q = \sum_{j=1}^N (\varepsilon_j^f - \varepsilon_j) \quad (4.2)$$

For the calibration, the following capture reactions



were measured at different projectile energies using different extraction fields for capture into the projectile ground state. The double coincidence mode (projectile-recoil ion), in which the previous experiments were carried out, served in minimizing interference between two reaction channels. For example, a *TOF* distribution of recoil ion will show two peaks corresponding to He_t^{1+} and He_t^{2+} . This distribution was used to gate on He^{1+} in order to discriminate the single capture from double capture. On the other hand, the projectile detector was used to gate on He_{proj}^{1+} which was separated from other possible charge states by an electrostatic deflector. The same method was used to double capture. As an example of these measurements, the longitudinal momentum distribution of the recoil ions for the single capture process at $V_p=0.9$ a.u. is presented in Fig. 4.2(a). This momentum distribution was measured using an extraction field of 1 *V/mm*. Each peak in this momentum distribution belongs to a certain capture line and hence to an exact Q -value. In order to determine calibration factor in Z -direction, the values of longitudinal momenta in channels are extracted from Fig. 4.2(a) and their values in *a.u.* are calculated using Eq. 4.1 (see table 4.2(c) in Fig. 4.2). Fig. 4.2(b) shows the position of the capture line against the calculated momenta. The slope of the fitted straight line yields the calibration factor in *ch./a.u.*. Following the same procedure, the calibration factor in Z -direction has been obtained for different extraction fields. To determine the calibration factor at high extraction field, the calibration factor is drawn as a function of the square root of the extraction field as shown in 4.2(d). The straight line is extrapolated to high extraction field region to determine the calibration factor at these high fields. Because the collision is symmetric around the beam axis, the same calibration factor as in the Z -direction is used in the Y -direction.

The calibration of the recoil ion spectrometer is also carried out using the program SIMION. Our SIMION calibration agreed within 10% deviation with the calibration carried out using the capture channel.

Since our spectrometer has an electrostatic lens in the acceleration region (on the recoil-ion side), the calibration factor in the time direction (x -direction) is ob-

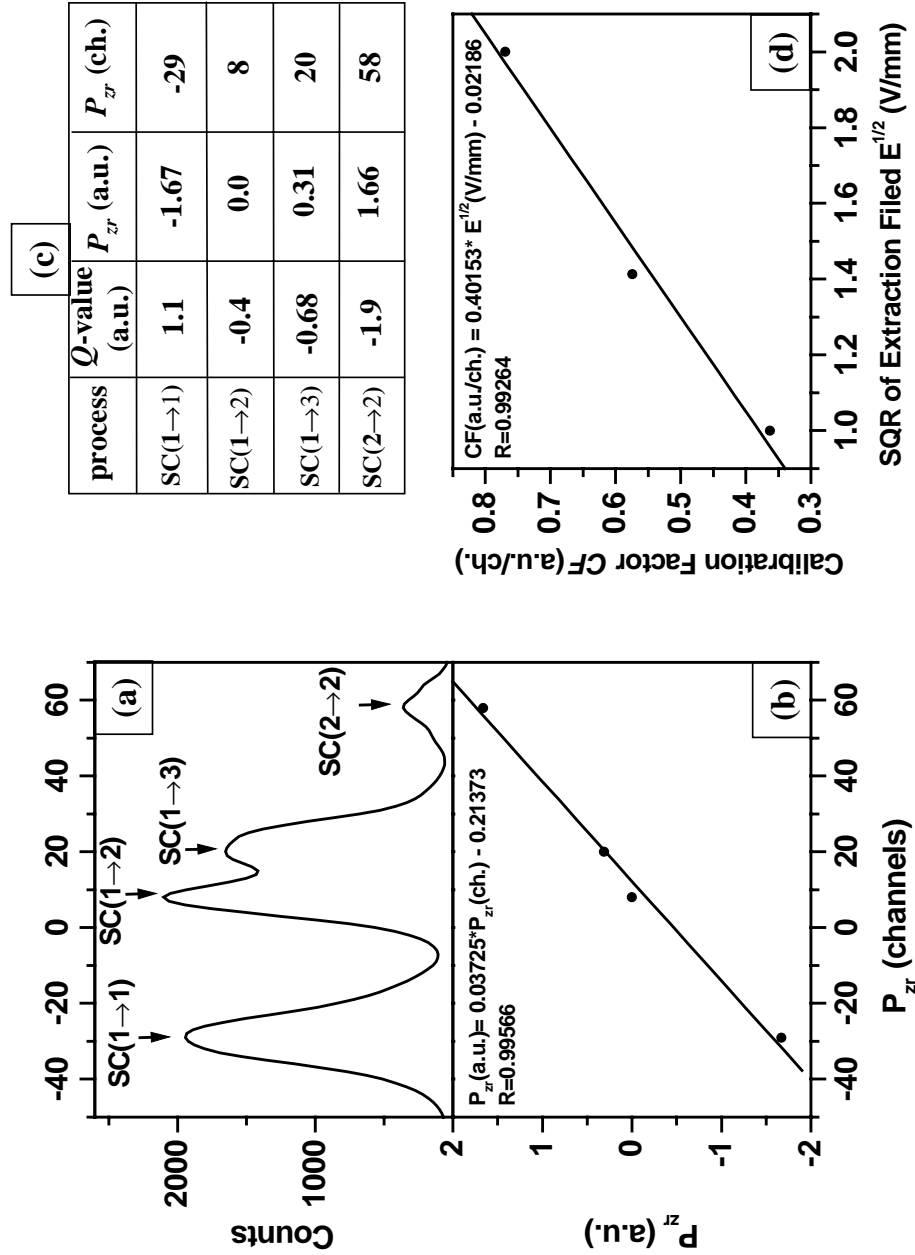


Figure 4.2: (a) is the longitudinal momentum distribution (in channels) of recoil ions for SC in the $He^{2+} - He$ collision system at the $V_p=0.9$ a.u..(b) The longitudinal momenta (in channels) extracted from (a) as function of their values in a.u. units calculated using Eq.4.1. (c) Table contains the longitudinal momenta in channels extracted from (a) and the corresponding values calculated using Eq.4.1. (d) Momentum calibration factor CF in Z-direction as a function of the square root of the electric field.

tained *SIMION* program. The maximum of each peak in the *TOF* distribution is considered as a momentum zero point for the different charge states of recoil ions.

4.2 Calibration Of The Electron Spectrometer

In order to calibrate the electron detector, a mask with an array of holes is positioned in front of the detector. An alpha particle source was used as a source of uniform parallel-ray ions. The image of the masked detector was reconstructed using the computer. Comparing this image with the known dimensions of the detector leads to conversion factor to go from the position in channels to the position in *mm*. In order to determine the momentum zero point of the electron detector, the voltage of spectrometer and electron detector is reversed to detect the recoil ions on the electron detector. Since the recoil ions have only negligible momentum, the momentum zero point of the electron detector is almost exactly on the position where the recoil ions hit the electron detector if the recoil ion time-of-flight is sufficiently short (as in our case). Fig. 4.3 presents the electron detector image of these detected ions used to determine the momentum zero point. The electrons move in uniform field with equipotential lines parallel to the detector surface. Therefore, electrons experience no acceleration in both directions of the detector so that the momentum is given by

$$P_{y,e} = c m_e \frac{(Y_e - Y_{o,e})}{T_e} \quad (4.3)$$

and

$$P_{z,e} = c m_e \frac{(Z_e - Z_{o,e})}{T_e} \quad (4.4)$$

where c is the position/channels calibration factor. $Y_{e,o}$ and $Z_{e,o}$ are the momentum zero points in the Y - and Z - directions. Y_e and Z_e are the impact positions of the electron on the detector measured with respect to the center of the detector. T_e is the time of flight of the electrons. It was not possible in our experiment to measure this time with a reasonable accuracy. Therefore, the Y - and Z - momentum components are calculated using Eq.4.3 and Eq.4.4 assuming a constant electron time-of-flight which is the time-of-flight of electrons with $P_x=0$. The nonzero value of P_x has only a small effect on the experimental resolution. To estimate this effect, An electron with $P_x = 0.2 \text{ a.u.}$ directed parallel or anti-parallel to the field yields about a 7.3% change in the electron time of flight and thus a similar error in momentum components transverse to the field calculated from the electron position.

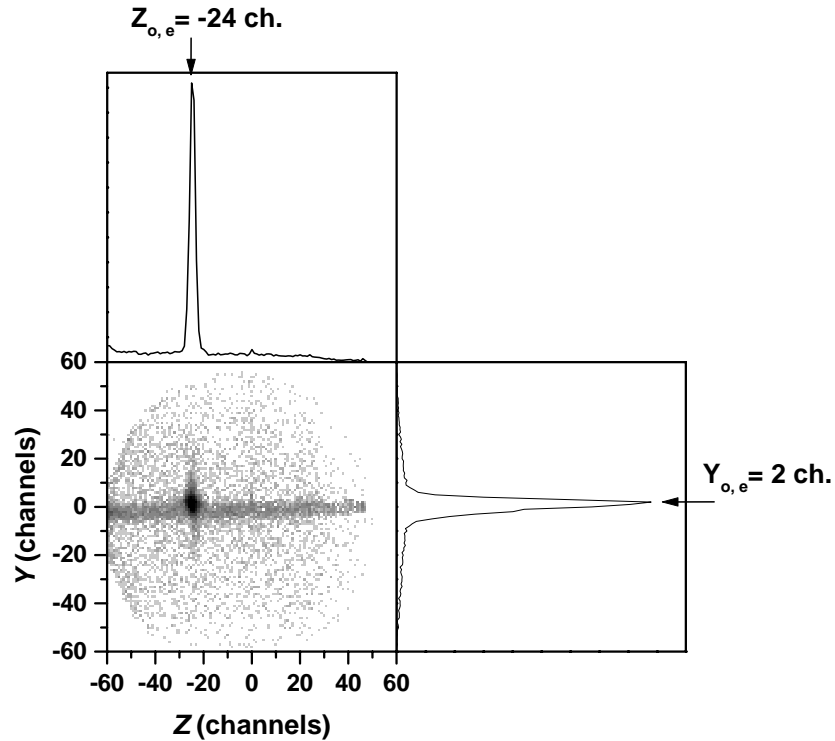


Figure 4.3: Raw recoil ion distribution measured by projecting the ions, resulting from the $He^{2+} - He$, onto the electron detector. This distribution has been used to determine the momentum zero point of the electron detector. The projections of the distribution are given in the upper and right figures.

4.3 Experimental Resolution of Multi-Hit-System

In the dissociation process of the H_2 studied in this work, the H_2 molecule explodes into two H^+ fragments. They arrive on the detector within a very short time difference. Therefore, one challenge in this work was to improve the multi-hit-system used in our experiment to be capable of detecting both fragments in a very short time. In this section, the performance of this system extracted from the experimental results will be discussed.

A main feature of this system is the so-called dead time (t_D), i.e, the time that this system needs to resolve two consecutive signals. To explore this feature, the time difference between the two fragments are calculated and presented in Fig. 4.5(a). A dead time of 10 ns has been achieved. To investigate the influence of the dead time on the measured data, the radial position difference between the two fragments Δr (where $\Delta r = \sqrt{(x_2 - x_1)^2 + (y_2 - y_1)^2}$) is plotted against the time difference Δt as shown in Fig 4.4. Again a dead time of 10 nsec is obtained. This dead time is mainly determined by the electronics used in the experiment.

Another important feature that can be checked is the angular resolution of the system which can be investigated by studying the angular correlation of the emitted fragments. The emission angle of a fragment from the dissociation of the molecule can be calculated from the measured momentum components. For the dissociation of the H_2 , the difference between the azimuthal angles ($\Delta\phi = \vartheta_{frag2} - \phi_{frag1}$; see Fig. 4.1) of the first and the second fragments is displayed in Fig 4.5(b). The derived distribution peaks at 180° . The width at the half maximum of the peak is $\pm 5^\circ$ which gives the angular resolution of the system.

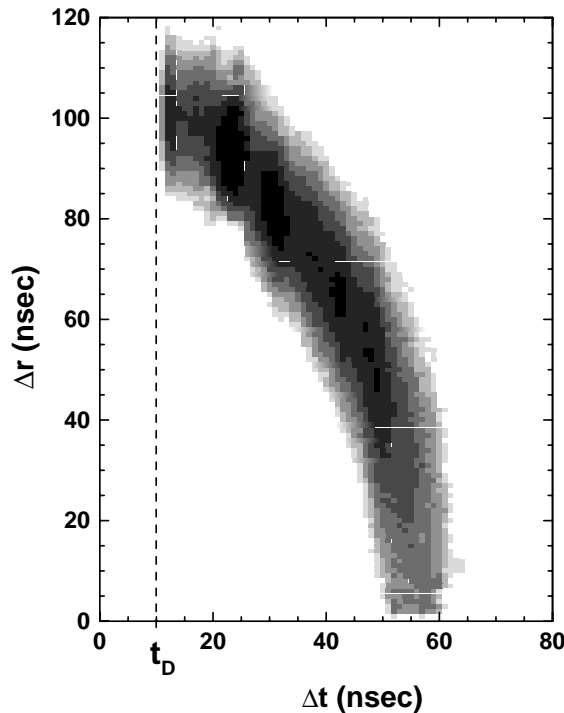


Figure 4.4: Radial position difference of both fragments Δr plotted against the time difference Δt . t_D is the dead time.

To obtain the momentum resolution of this system, the momentum of the center-of-mass of both fragments resulting from the TI of H_2 by He^{2+} is calculated and is then rotated in the scattering planes of the projectile. The result is presented in Fig. 4.6(a). The scattered projectile is fixed in $+y$ -direction which helps to calculate the experimental momentum resolution of the multi-hit-system. This assumes that the momentum of the emitted electron is very small comparing to the momentum of the CM and can be neglected. This assumption is very well fulfilled for the present collision system. Accordingly, the momentum resolution will be the change in CM momentum of the fragments around the y -axis. Therefore, the CM momentum distribution is projected on the horizontal axis to determine the momentum resolution as shown in Fig. 4.6(b). From the width at half-maximum, a momentum resolution of $\Delta p = \pm 2.3 a.u.$ is obtained.

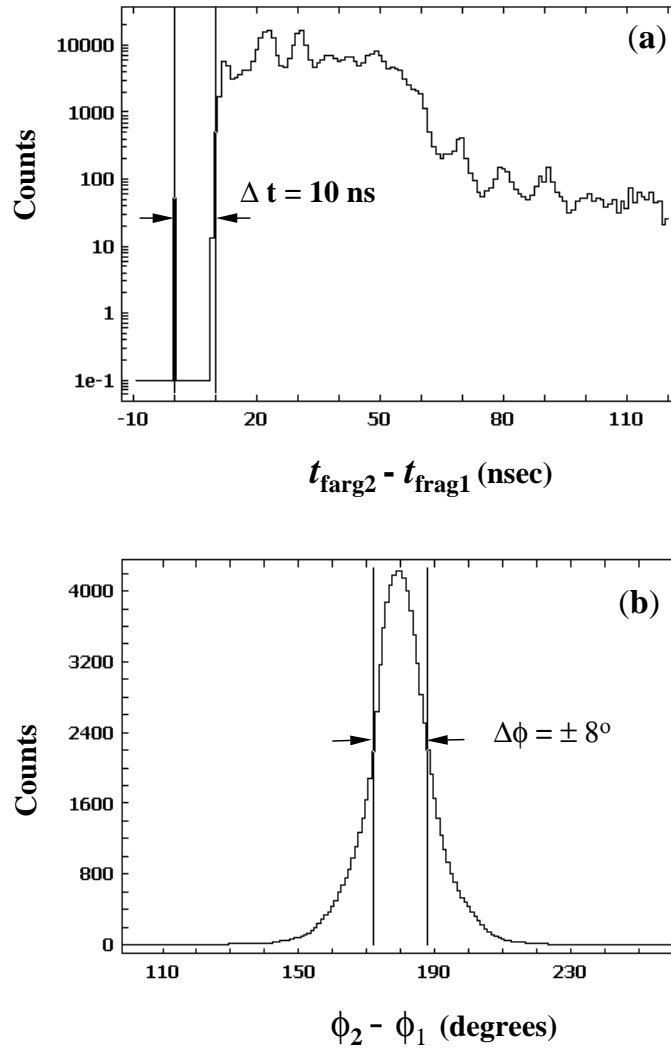


Figure 4.5: (a) Time difference between the two fragments given in *nsec* units. The figure shows the dead time of 10 *nsec* for the multi-hit-system used in the present work. (b) The difference between the azimuthal angles of the first fragment ϕ_1 and second fragment ϕ_2 . The figure shows that the multi-hit system has an angular resolution of $\pm 8^\circ$.

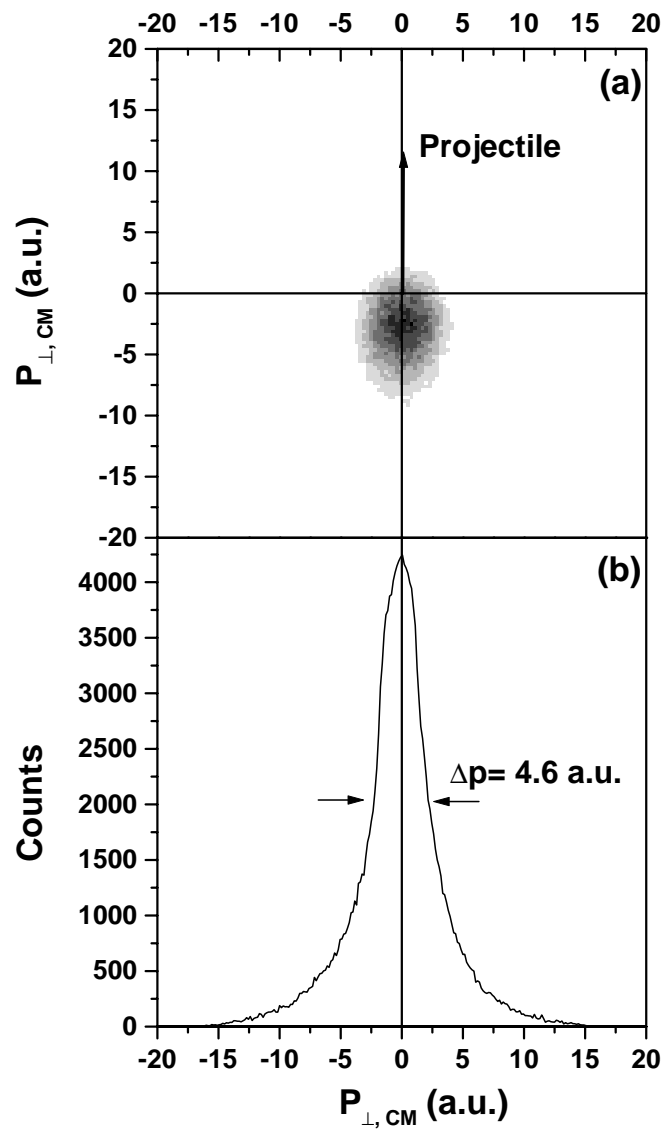


Figure 4.6: (a) Momentum of the center-of-mass of both fragments resulting from the TI of H_2 by He^{2+} rotated in the scattering planes of the projectile. The emission of the outgoing projectile is fixed as indicated by the arrow, whose length is arbitrary. (b) projection of the CM-momentum distribution seen in (a) on the horizontal axis.

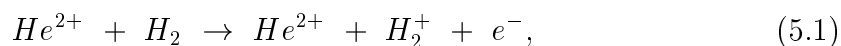
Chapter 5

Results and Discussion

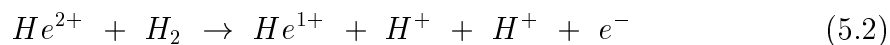
5.1 Data Presentation

5.1.1 ${}^3He^{2+}$ - H_2 Collision System

We have investigated this collision system utilizing the *COLTRIMS* technique. The single ionization and transfer ionization channels have been measured. While the single ionization of H_2 leads to H_2^{1+} ions in non-dissociative states



in the transfer ionisation of H_2 , one electron is captured by the projectile and the second one is emitted to the continuum leading to the dissociation of H_2



5.1.2 Dissociative Ionization of H_2 (Fragmentation Process)

The coincidence detection of both fragments resulting from the dissociation of H_2 allowed the studying of the H_2 dissociation process by providing two things: (a) distinguishing the dissociative ionization process from other processes especially direct ionization process, (b) providing information about the molecular orientation at the instant of the electronic excitation. Utilizing the measured times-of-flight and impact positions on multi-hit-detector of both fragments, we were able to calculate all quantities relating to the dissociation process, like momentum, energy,..etc. In the next section, we will focus our discussion on the ionic motion of this collision system.

Ionic Motion

The removal of two electrons from H_2 leads automatically to the dissociation of the molecule into two free H^+ ions. The kinetic energy of the two ions in the final state has two sources: the energy transfer from the projectile during the collision and the energy from the Coulomb repulsion between the protons. Fig. 5.1 displays the kinetic energy of one H^+ fragment resulting from the dissociation of H_2 by He^{2+} . The figure shows that the energy distribution is broad and peaked around 9.5 eV. This energy is slightly lower than that one would obtain from Coulomb repulsion if one instantaneously strips the electrons from the ground state which equals 9.7 eV. In addition, this figure can be compared with the kinetic energy spectra of H^+ ions calculated based on the "reflection approximation" [175]. These spectra are presented in Fig. 5.2. The comparison shows that H^+ ions gain their kinetic energy from the Coulomb repulsion. To study the dependence of the fragment energy on the molecular orientation, the fragment energy distribution has been generated for parallel orientation, i.e parallel to the beam axis and perpendicular orientation, i.e perpendicular to it. These distributions are given in Fig. 5.3. The distributions show no molecular orientation dependence of the fragment energy. The same result can be observed from the *CTMC* calculations which are performed for this collision system and presented in Fig. 5.3.

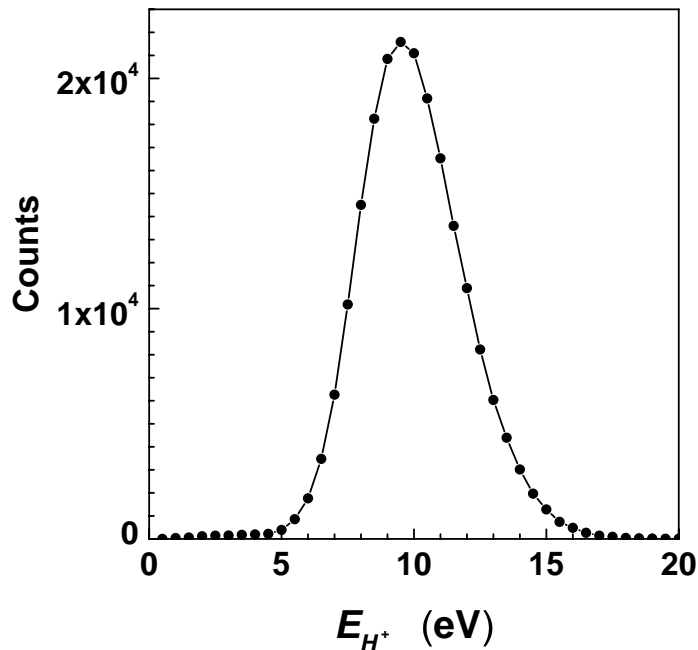


Figure 5.1: H^+ ion kinetic energy distribution for $He^{2+} + H_2$ integrated over all angles and energies of electrons.

To further investigate the ionic motion for this collision system, the energy of one H^+ is plotted versus the energy of the other H^+ in Fig. 5.4(a). The peak is concentrated around $E_1 = E_2 = 9.5\text{eV}$. This means that the total energy of fragments is determined by the vertical *Frank – Condon* transition to the repulsive

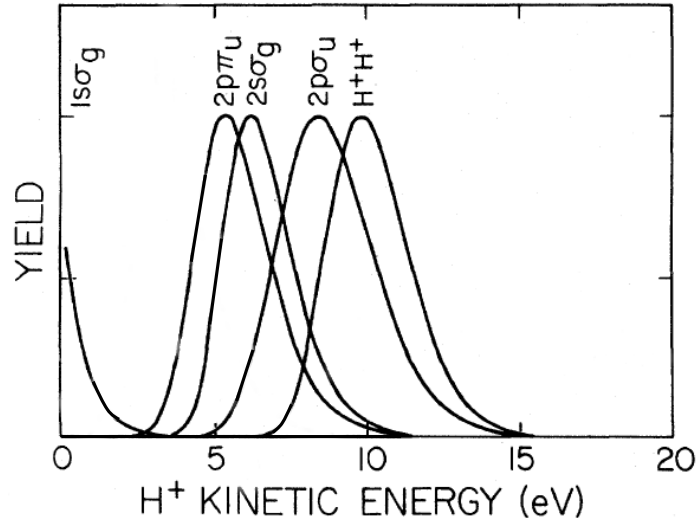


Figure 5.2: Kinetic energy spectra of H^+ ions calculated based on the "reflection approximation" (adapted from [175]).

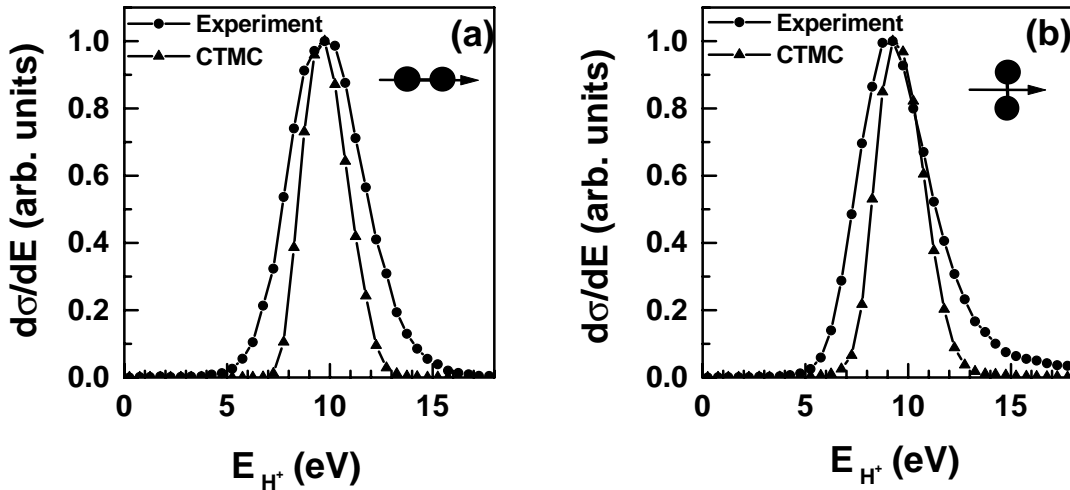


Figure 5.3: H^+ ion kinetic energy distribution generated for (a) parallel molecular orientation, i.e. parallel to the beam axis and (b) perpendicular molecular orientation, i.e. perpendicular to the beam axis. Circles represent the experimental data and Triangles are referred to the *CTMC* calculations.

coulomb potential of the isolated molecule. Although most density of events is concentrated around 9.4eV point, some events shift away from this point. This indicates that the kinetic energy transfer from the projectile has an influence on the collision. The momentum distribution of the fragment ions is given in Fig. 5.4(b) using *Jacobi* coordinates. The momenta of fragments are symmetric around the origin. A three dimensional momentum picture would be a spherical surface of radius $P = (2mE)^{1/2} \approx 34\text{a.u.}$.

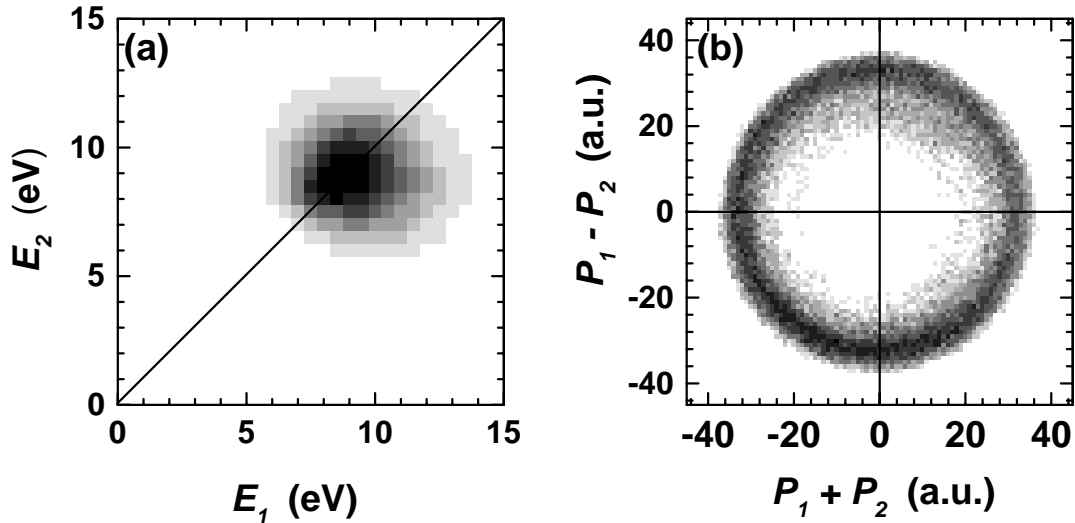


Figure 5.4: (a) The energy sharing, $E_{H^+}^1$ versus $E_{H^+}^1$, between the H^+ for dissociative ionization of H_2 by 25 keV He^{2+} impact. (b) Momentum distribution of the dissociated protons. The Jacobi-coordinates are used.

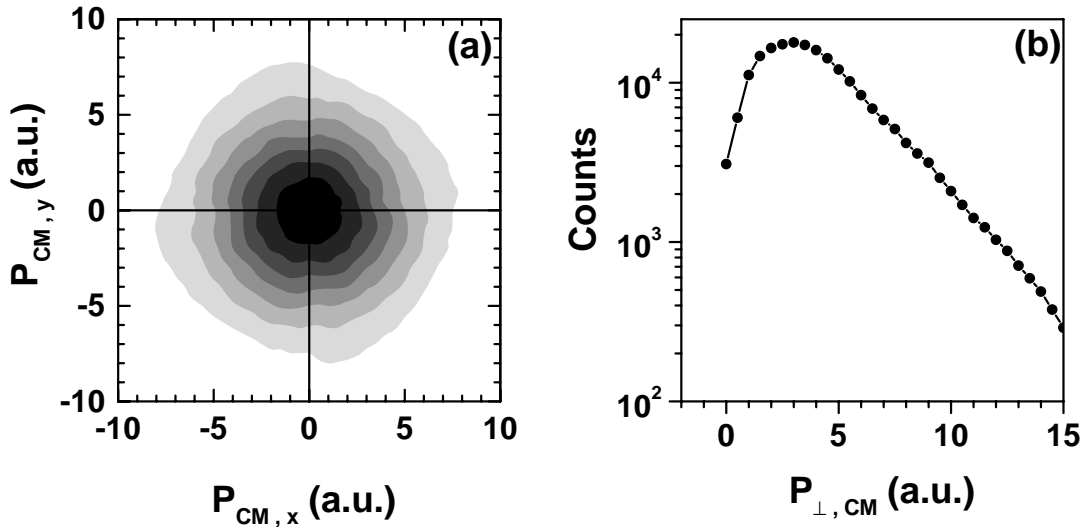


Figure 5.5: (a) Two-dimensional transverse momentum distribution of the center-of-mass of both fragments for 25 keV $He^{2+} + H_2$ collisions. (b) Radial transverse momentum distribution obtained by integrating over all azimuthal angles.

To explore the influence of the projectile on the collision, the momentum vector of the center-of-mass of both fragments is calculated. The 2D-transverse momentum of CM of both fragments is presented in Fig. 5.5(a). It is evident that the projectile exchanges momentum with the molecule. To further demonstrate the interaction between the projectile and both fragments, the radial transverse momentum of the CM has been calculated by integrating over all azimuthal angles. The result is

Figure 5.6: (a) Momentum distribution of the dissociated protons in 25 keV $He^{2+} + H_2$ collision system; Where P_{\parallel} : longitudinal momentum component of fragments and P_{\perp} : transverse momentum component of them. (b) Angular distribution of the dissociated protons in 25 keV $He^{2+} + H_2$ collision system.

presented in Fig. 5.5(b). The distribution exhibits a broad peak around 4 a.u..

For a better understanding of the dynamics of the collision, we have plotted the transverse momenta of the fragments against the corresponding longitudinal momenta of the fragments as in Fig. 5.6(a). we have used a coordinate frame in which p_{\parallel} is defined by the direction of the incident projectile and p_{\perp} is perpendicular to this direction. This spectrum is integrated over all directions and energies of electrons. The fragments show up most probably perpendicular to the beam direction. To determine the orientation dependence of transfer-ionization process of H_2 , the angle of the final-state momentum of the dissociation products with the incident beam direction is determined. This assumes that the rotation of the molecule is much

slower than the collision time. Fig. 5.6(b) shows the angular distribution of H^+ ions. The distribution exhibits a maximum at the perpendicular orientation.

Electronic Motion

The scattering plane used to present the momentum distributions is defined by the beam direction (z -axis) and the momentum vector of CM of both fragments ($-y$ -axis). The singling-out of the scattering plane was done by the selection of ranges of the transverse momentum of the CM of both fragments. Distributions of the electron momentum are generated for two special CM planes: the nuclear scattering plane and the plane perpendicular to it. The former plane produced a "top-view" of the electron momentum distribution. The latter plane produced a "side-view" of the electron momentum distribution.

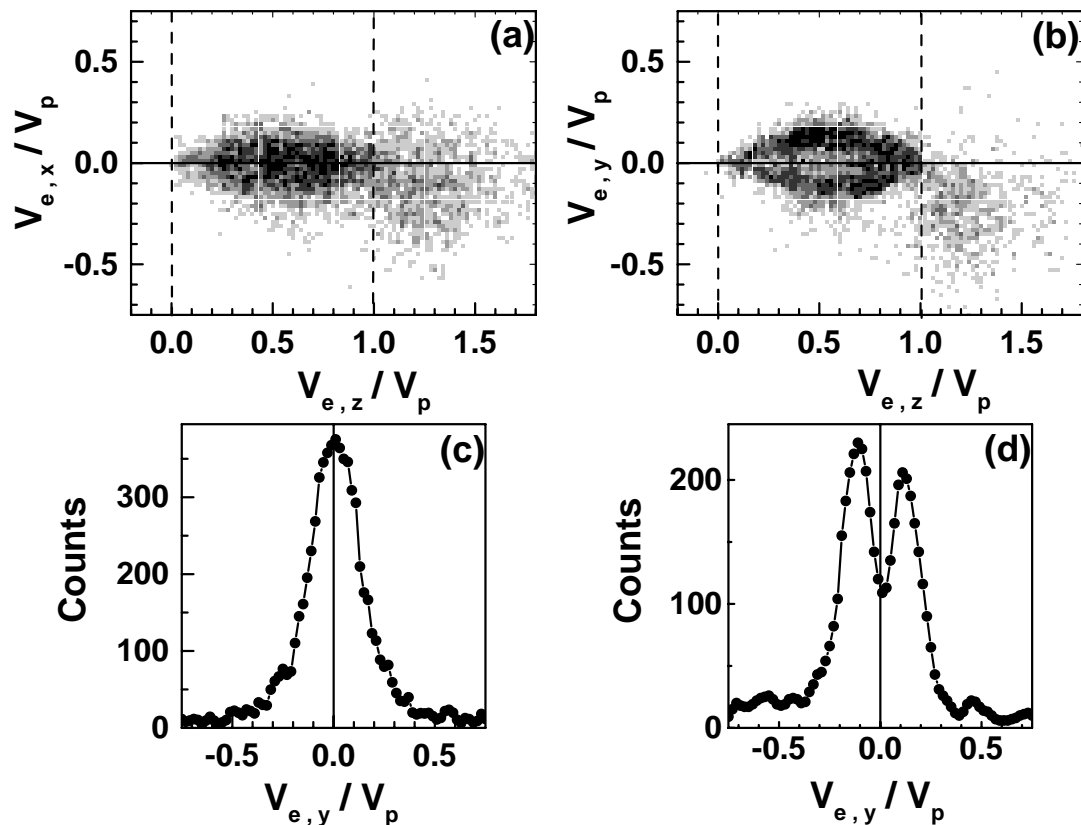


Figure 5.7: (a) Side view of ejected electron momentum distribution in the collision $25 \text{ keV } He^{2+} + H_2$. (b) Top view of ejected electron momentum distribution in the same collision. (c) and (d) are the transverse projections of the distributions in (a) and (b) for a slice centered at $V_{e,z}/V_p = 0.5$. The electron velocity components $V_{e,z}$ and $V_{e,y}$ are scaled by the projectile velocity (V_p).

"Side" and "Top"-views of the ejected electrons are presented in Figs. 5.7(a) and 5.7(b). Note that all horizontal and vertical scales are given in units of v_p to ease comparison. The electrons are seen to be preferentially emitted in the forward

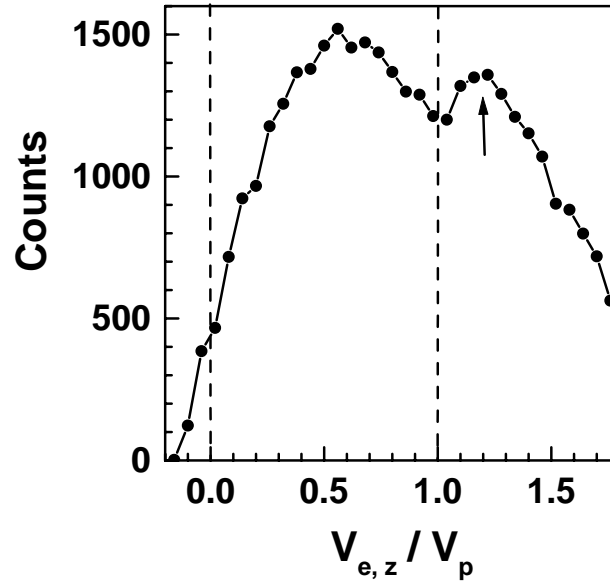


Figure 5.8: Z-component of the velocity of electrons ejected in the collision $25 \text{ keV He}^{2+} + \text{H}_2$ leading to dissociation of H_2 . The electron velocity component is scaled by the projectile velocity (V_p). The arrow points to the fast forward electrons group.

direction. The salient feature of the electron momentum distributions consists in the appearance of two groups of electrons with different structures. The first group consists of electrons emitted with velocities between zero and v_p ; the vicinity of the saddle-point velocity. This group is well known from earlier studies [36, 46, 1, 27]. The other group consists of electrons ejected with velocity greater than the projectile velocity. This group is referred to as the fast forward electrons or mirror image electrons.

Saddle-point electrons

The side-view distribution shows that the saddle-electrons distribution is symmetric around the internuclear axis. It is interesting to see that the distribution is very narrow. This indicates that these electrons are strongly confined to the scattering plane. This can be understood as the ejected electrons try to follow the nuclear motion which is in the scattering plane by definition. A projection of Fig. 5.7(a) near $V_{e,z}/V_p = 0.5$ onto the $V_{e,y}/V_p$ axis is given in Fig. 5.7(c). It shows clearly the collimation of the ejected electrons to the scattering plane.

The "top-view" of the ejected electron momentum distribution given in Fig. 5.7(b) reveals that the saddle-point electrons are emitted in two-jets oriented in the scattering plane in the forward direction and off the projectile-axis. This local minimum and the "two branch" structure can be seen more clearly by making a transverse projection of a slice of the two-dimensional distribution with a width of $0.2V_p$ at $V_{e,z}/V_p = 0.5$. The result of this projection is shown in Fig. 5.7(d). It is

interesting to note that more electrons are emitted away from the C.M. direction. These results represent for the $He^{2+}-H_2$ collision system the first direct experimental observation of the characteristics of the momentum distributions of the electrons emitted in this collision system in the vicinity of the saddle-point velocity.

Fast Forward Electrons: Mirror Image Electrons

The second electron group which has appeared in the electron momentum distributions is the fast forward electrons. These electrons possess a different structure than that shown for the saddle-point electrons. These electrons follow the direction of CM of both fragments as shown in Fig. 5.7(b). To further explore these fast forward electrons, the two-dimensional electron momentum distribution in Fig. 5.7(b) is projected onto the $V_{e,z}$ axis. The projection is given in Fig. 5.8. The figure shows that the fast forward electrons reveal a distinct peak and yield a significant contribution to the cross section of the dissociative transfer ionization of H_2 . It is surprising to see that the distribution exhibits a dip at the projectile velocity where in fast collisions the cusp electrons are found.

Impact-Parameter Dependence of the Electron Momentum Distributions

To study the impact-parameter dependence of the emitted electron momentum distribution in the scattering plane, the electron distribution was gated on different ranges of transverse momentum transfer, i.e., impact parameter. The results are shown in Figs. 5.9(a-c). In these figures, the transverse momentum transfer increases moving from Fig. 5.9(a) to Fig. 5.9(c) and therefore, the impact parameter decreases moving the same way according to the following formula

$$P_{\perp} = \frac{2q_t q_p}{bV_q} \quad (5.3)$$

where q_t and q_p are the effective charges of the target and the projectile, respectively, and b is the impact parameter. The figures show that the distribution exhibits the two fingers for all ranges of impact parameter. However, the distribution becomes more symmetric at smaller impact parameter. This suggests as we will see later that the relative contributions of σ and π amplitudes depend on the impact parameter. At small impact parameters the π orbital is dominant over σ orbital. This leads to symmetric distribution around the nuclear axis as shown in Fig. 5.9(c). At large impact parameters the σ orbital contribution increases relatively, leading to the asymmetry of the distribution as appears in the momentum distribution presented in Fig. 5.9(a).

Concerning the fast forward electrons, the figures show that these electrons are strongly dependent on the impact parameter. For further demonstration of the dependence of the fast forward electrons on the impact parameter, the momentum distributions in Figs. 5.9(a-c) are projected onto $V_{e,z}$ axis. The projections are presented in figures 5.11(a-c). The figures illustrate that these fast forward electrons

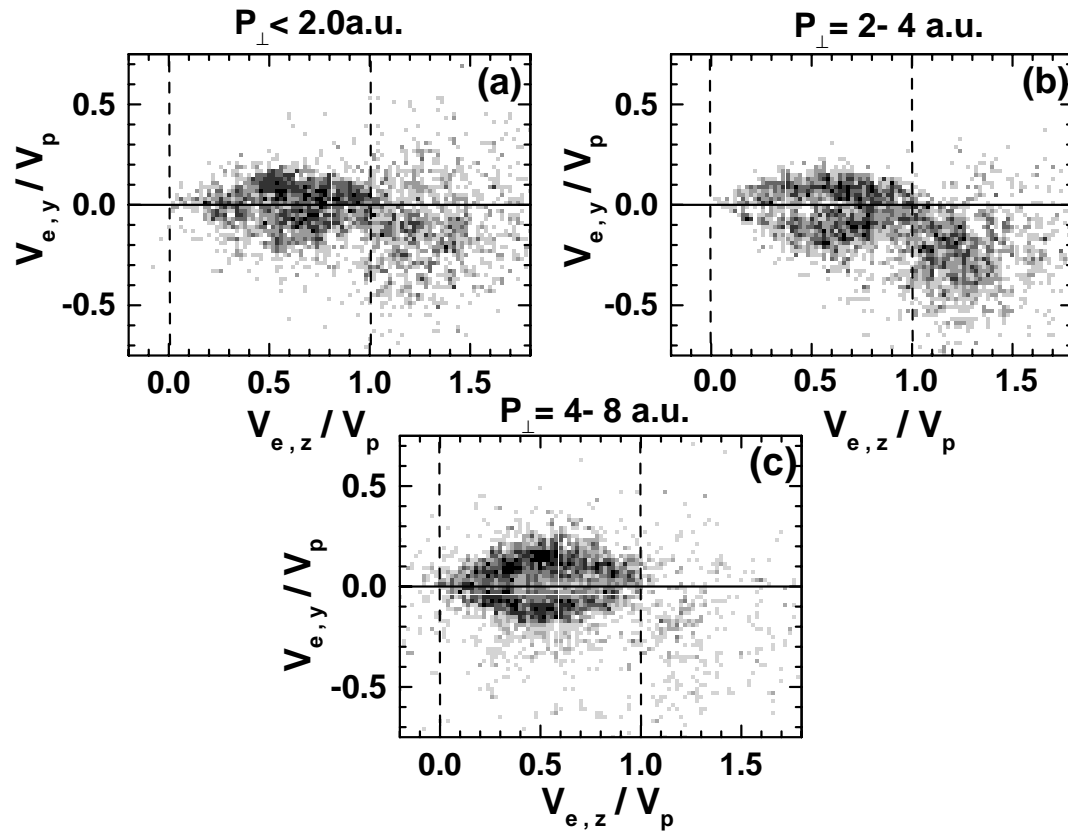


Figure 5.9: Top view of ejected electron momentum distribution in the collision $25 \text{ keV } He^{2+}$ on H_2 leading to dissociative ionization of H_2 generated for different transverse momentum transfer, i.e., different impact parameter. The electron velocity components $V_{e,z}$ and $V_{e,y}$ are scaled by the projectile velocity (V_p). The impact parameter decreases in the figures moving from (a) to (c).

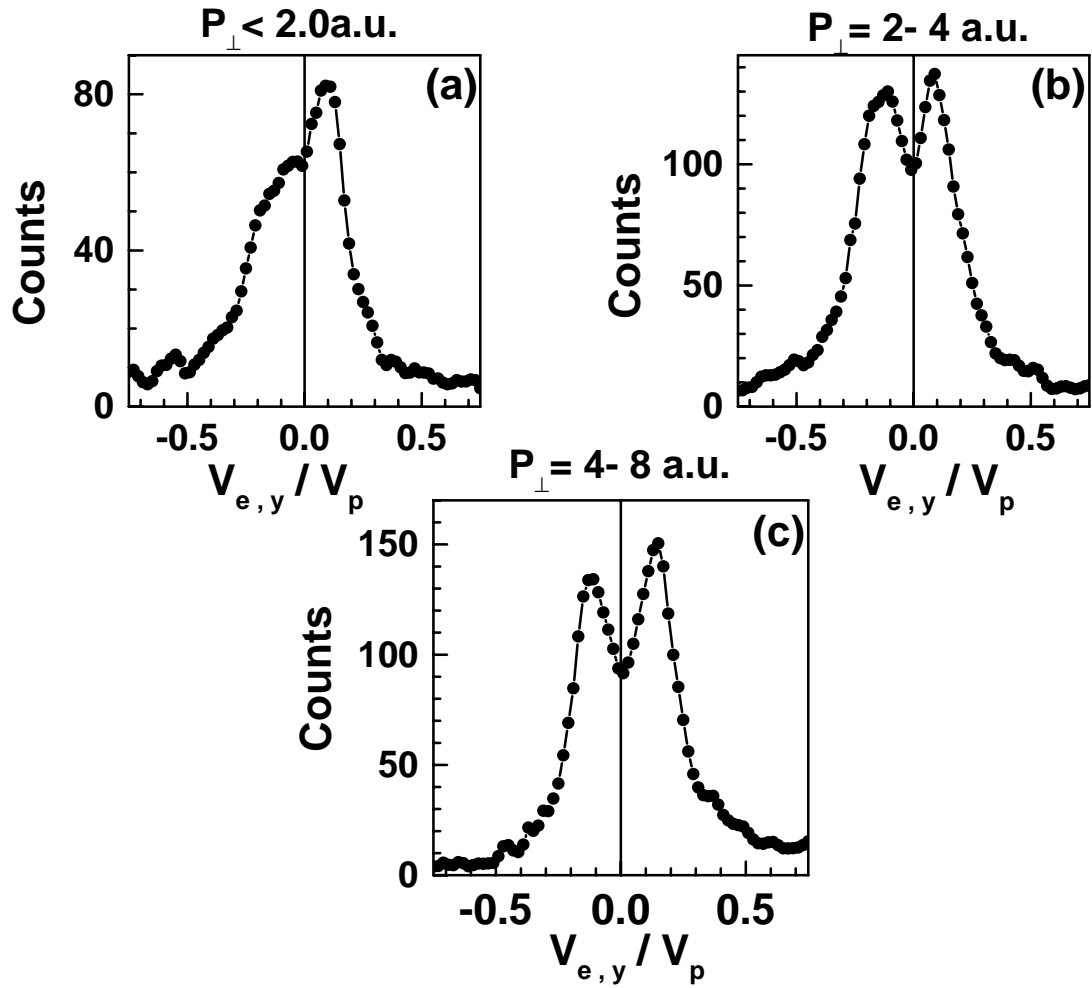


Figure 5.10: (a)-(c) are the projections of the momentum distributions in Figs. 5.9(a)- 5.9(c) near $V_{e,z}/V_p = 0.5$ on the vertical axis ($V_{e,y}$).

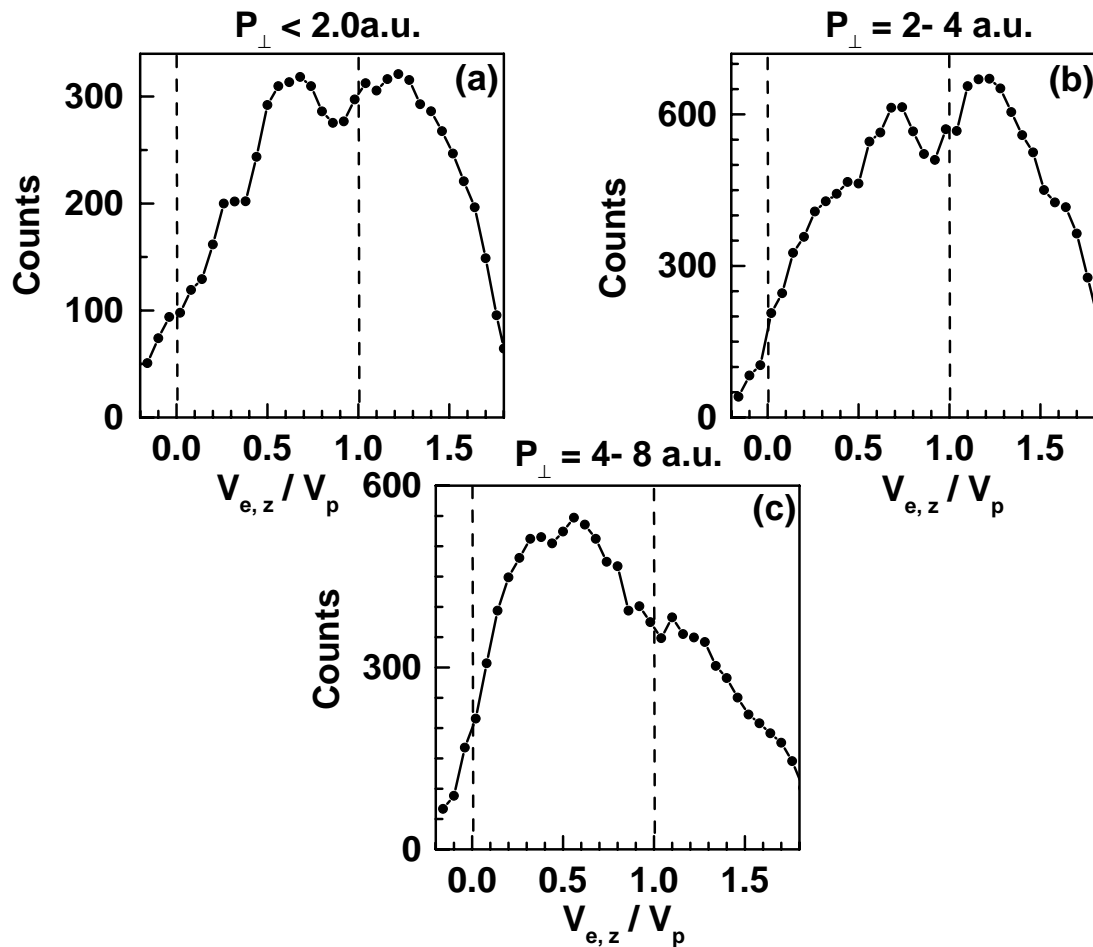


Figure 5.11: (a)-(c) are $V_{e,z}$ of the ejected electrons in the dissociative ionization of H_2 by He^{2+} at $V_p=0.81$ a.u. for different impact parameters. The electron velocity component $V_{e,z}$ is scaled by the projectile velocity (V_p).

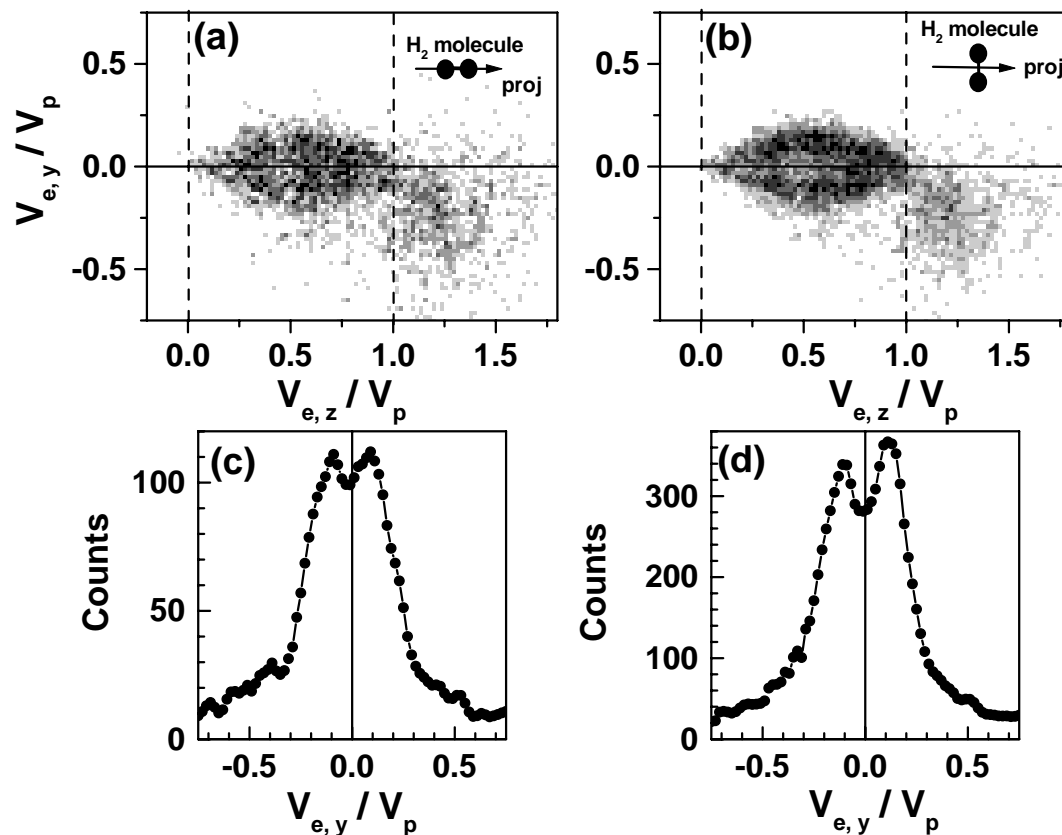


Figure 5.12: Ejected electron momentum distribution in the dissociative ionization of H_2 by $25\text{ keV } He^{2+}$ generated (a) for parallel molecular orientation (i.e. the molecule axis is parallel to the beam direction) and (b) for perpendicular orientation (i.e. perpendicular to the beam direction). (c)-(d) are the projections of the distributions in (a) and (b) near $V_{e,z}/V_p = 0.5$ on the vertical axis ($V_{e,y}$). The electron velocity components $V_{e,z}$ and $V_{e,y}$ are scaled by the projectile velocity (V_p).

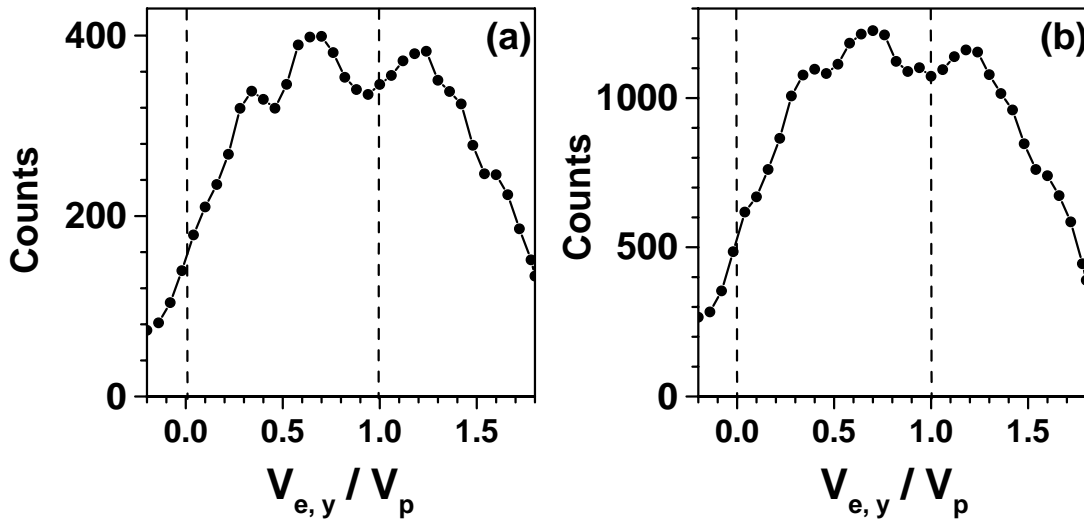


Figure 5.13: (a) and (b) are the projections of distributions in Figs 5.12(a) and 5.12(b) on the horizontal axis ($V_{e,z}$).

result from a narrow range of impact parameters and appear as image saddle in the projectile frame.

Orientation Dependence of the Electron momentum distribution

To study the dependence of the electron momentum distributions on the molecular orientation, the electron momentum distributions are generated for two molecular orientations: parallel to the beam direction and perpendicular to it. The results are given in Figs. 5.12(a) and 5.12(b). The figures show that the electron momentum distribution in the scattering plane exhibits the two fingered structure for both molecular orientation. This can be seen more clearly in the transverse projections of the distributions near $V_{e,z}/V_p = 0.5$. These projections are presented in Fig. 5.12(c) for the parallel orientation and in Fig. 5.12(d) for the perpendicular orientation. It is noted that the distribution is more symmetric in the case of the perpendicular orientation.

Fig. 5.13 shows the projections of momentum distributions in Figs. 5.12(a) and 5.12(b) onto the $V_{e,z}$ axis. In these figures, the fast forward electrons are seen to appear in the electron momentum distributions for both molecular orientations.

5.1.3 Single Ionization of H_2

Ionic Motion

Figure 5.14 shows the recoil-ion transverse momentum distribution for the collision of $He^{2+} + H_2$ at projectile velocity of 0.81 leading to single ionization of H_2^{1+} . This distribution was calculated by integrating over all azimuthal angles. The distribution

exhibits a peak around $P_{\perp} = 1$ a.u.. This suggested that the ionization process in this system happens over a range of impact parameters where the contribution of large impact parameters is dominant.

Electronic Motion

Side and top views for the momentum distributions of electrons liberated in the impact of ${}^3\text{He}e^{2+}$ on H_2 leading to the single ionization are presented in figure 5.15(a) and figure 5.15(b), respectively, using the scattering plane defined by the beam direction (z) and the recoil-ion momentum vector ($-y$). The figures display that the electrons liberated during the collision are emitted in the forward direction. It is also noted that these electrons tend to stay in the scattering plane as observed in the side-view of the electron momentum distribution. The top-view reveals a maximum at the internuclear axis. This suggests that the contribution of the σ orbital in the ionization process is dominant, leading to the concentration of the electrons around the internuclear axis as shown in Fig. 5.16(b). Fig. 5.16(a) displays the Z -component of the electron velocity. It is noted that the contribution of the fast forward electrons to the cross section of the single ionization of H_2 is small comparing to that obtained for the dissociative ionization of H_2 .

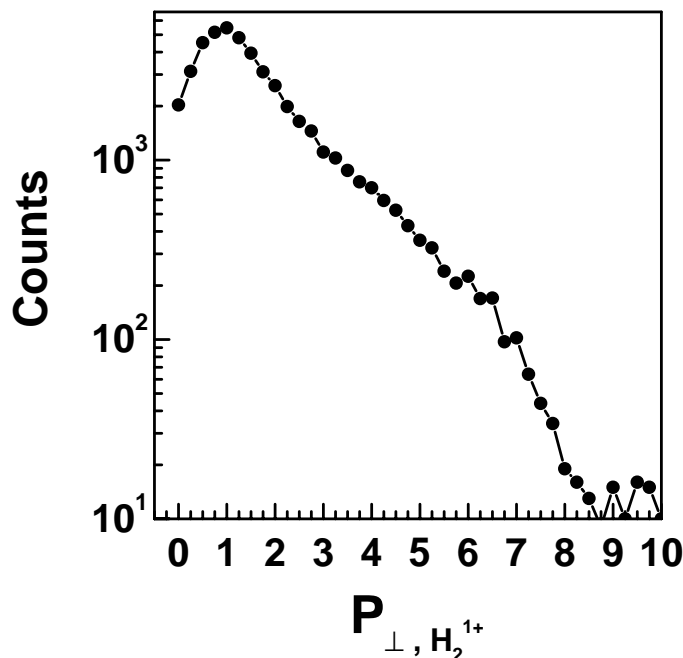


Figure 5.14: Recoil-ion radial transverse momentum distribution in the collision $\text{He}e^{2+} + \text{H}_2$ leading to single ionization of H_2 . The distribution was calculated by integrating over all azimuthal angles.

Impact-Parameter Dependence

The impact-parameter dependence of the emitted electron momentum distribution in the scattering plane is studied by generating the momentum distributions for different ranges of transverse momentum transfer, i.e., impact parameter. The results are presented in Figs. 5.17(a-c). In these figures, the transverse momentum transfer increases moving from figure 5.9(a) to figure 5.9(c) and therefore, the impact parameter decreases moving the same way. The ejected electron momentum distribution begins to concentrate along the projectile beam axis as the impact parameter increases. This indicates that the σ -orbital is dominant over all ranges of impact parameter. To study the impact dependence of the fast forward electrons, the 2D-distributions in Figs. 5.17(a-c) are projected on the Z-axis. These projections are given in Figs. 5.18(a-c). The figures show that fast forward electrons have disappeared at large impact parameters and started to appear at small impact parameters.

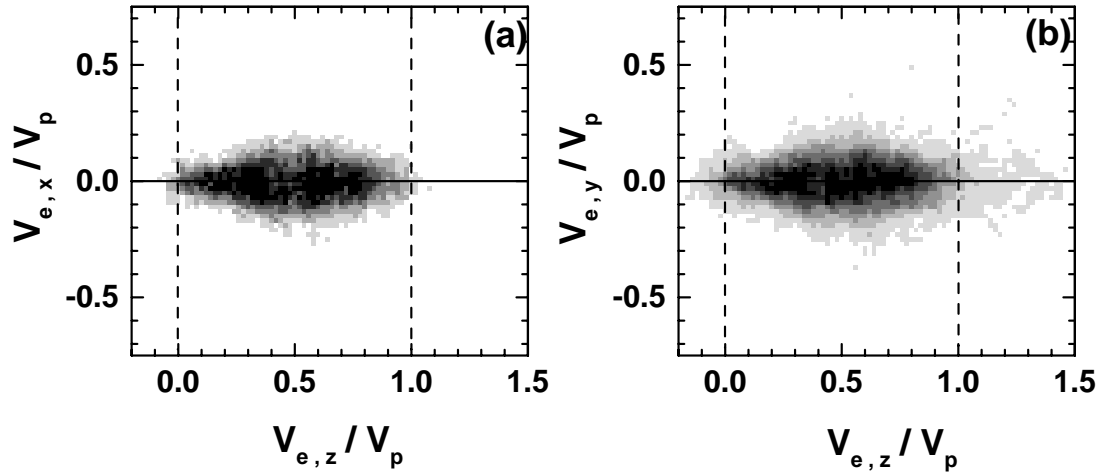


Figure 5.15: (a) Side view of ejected electron momentum distribution in the collision $25 \text{ keV } He^{2+} + H_2$ leading to SI of H_2 . (b) Top view of ejected electron momentum distribution in the same collision. The electron velocity components $V_{e,z}$ and $V_{e,x}$ are scaled by the projectile velocity (V_p).

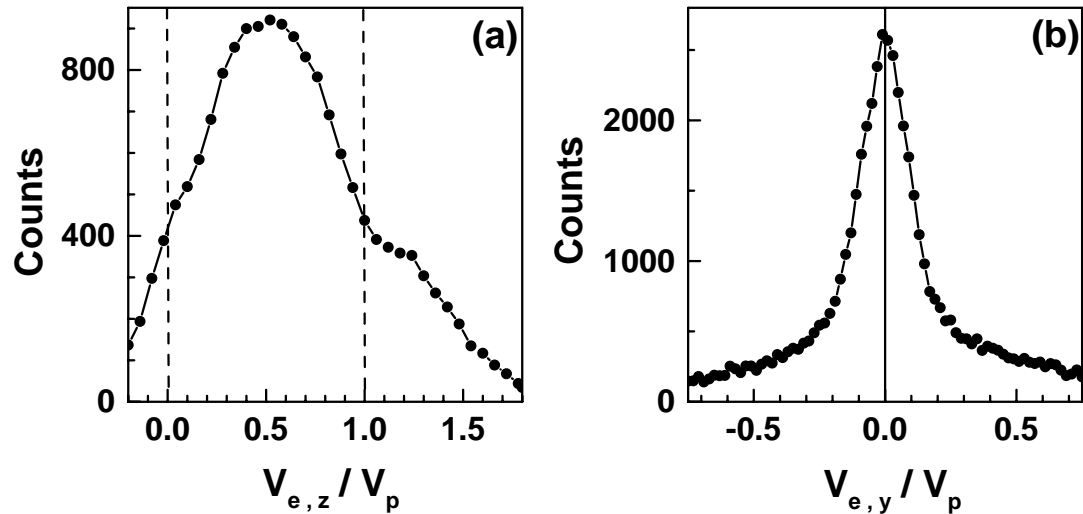


Figure 5.16: (a) Z-component of the velocity of electrons ejected in the collision $25 \text{ keV } He^{2+} + H_2$ leading to SI of H_2 . (b) is the Y-component of the velocity of electrons. The electron velocity components $V_{e,z}$ and $V_{e,x}$ are scaled by the projectile velocity (V_p).

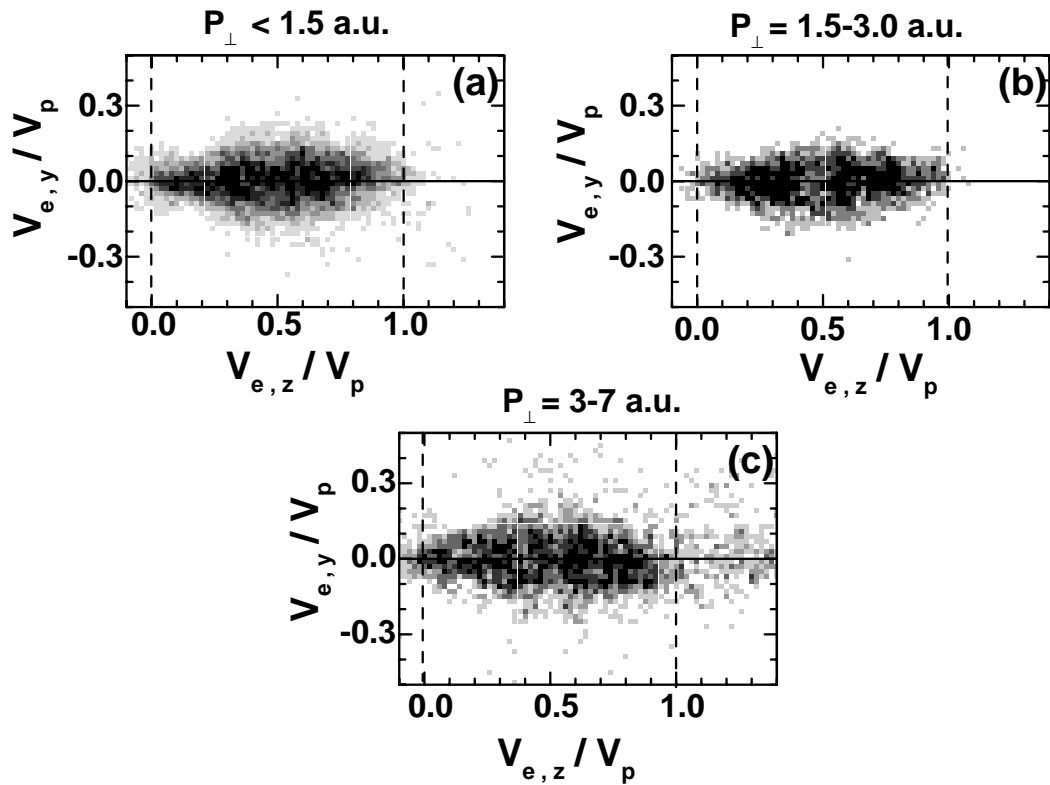


Figure 5.17: (a)-(c) Top view of the ejected electron momentum distribution in the collision 0.81 a.u. He^{2+} on H_2 , leading to SI of H_2 , for different windows on the magnitude of the transverse momentum transfer. The electron velocity components $V_{e,z}$ and $V_{e,y}$ are scaled by the projectile velocity (V_p).

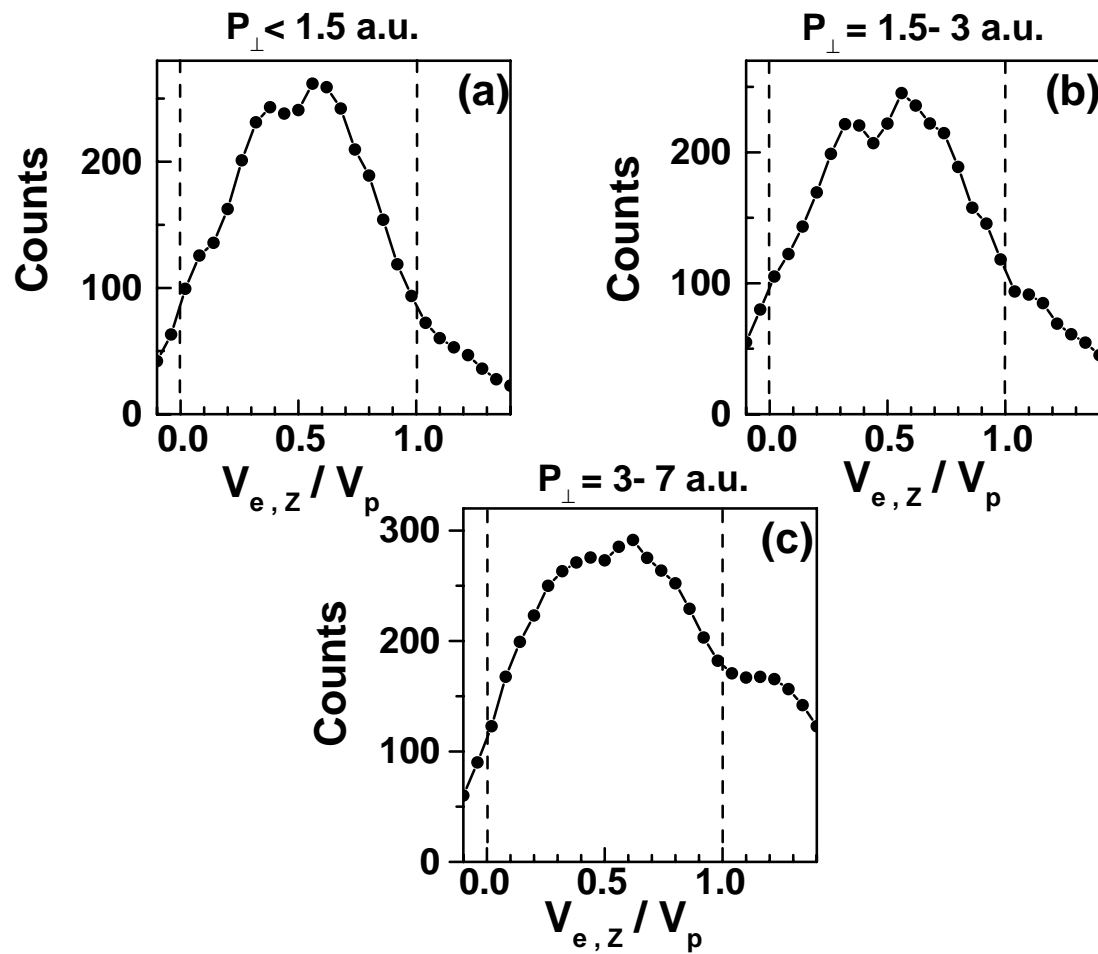
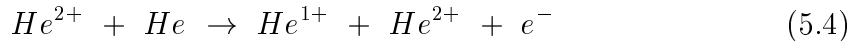


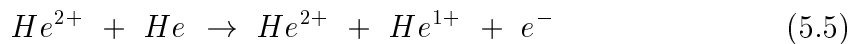
Figure 5.18: (a)-(c) are, respectively, the projections of the 2D-distributions in Fig. 5.17(a-c) on the $V_{e,z}$ axis.

5.1.4 ${}^3\text{He}^{2+}$ - He Collision System

In order to improve our understanding of the results obtained for H_2 target, the same measurements have been carried out for the helium target, the corresponding atomic two-electron system. In this collision system, two types of ionization reactions are investigated: **Transfer Ionization (TI)** and **Single Ionization (SI)**. While, in the transfer ionization of He, one electron is emitted from the target to the continuum and the second electron is captured by the projectile



in the single ionization (SI) of He, only one electron is emitted from the target to the continuum and the other stays in the bound states of the target



The results for two reactions will be presented in the next sections.

Ionic Motion

Fig. 5.19 displays the recoil-ion transverse momentum distribution of the transfer-ionization (**TI**) and the single ionization (**SI**) for the collision of $\text{He}^{2+} + \text{He}$ at a projectile velocity of 0.81a.u.. These distributions were calculated by integrating over all azimuthal angles. In **SI** case, the He^+ distribution exhibits two maxima. The first peak is sharp and centered around $P_{\perp,1} = 1.5$ a.u.. The second peak is a broad peak around $P_{\perp,2} = 9.0$ a.u.. In **TI** case, the He^{2+} distribution possesses a broad peak about $P_{\perp,\text{He}^{2+}} = 4$ a.u.. It is observed that the momentum distribution of **SI** oscillates around the momentum distribution of **TI**. In other words, the broad peak of the **TI** disappears in the momentum distribution of **SI**.

Electronic Motion

To investigate the electronic motion of this collision system, the same coordinate system used to study the $\text{He}^{2+} + H_2$ collision system was adopted. The scattering plane is defined by the incident beam (z) and the direction of the emitted recoil (-y). Distributions of the electron momentum are generated for two special recoil planes; the scattering plane and the plane perpendicular to it. The former plane produced a top-view of the electron momentum distribution. The latter plane produced a side-view of the electron momentum distribution.

Side views of the electron momentum distributions for the single ionization (**SI**) and for the transfer ionization (**TI**) in 0.81 $\text{He}^{2+} + \text{He}$ collision system are given in Figs 5.20(a) and 5.20(b), respectively. In **TI** case, both groups of electrons, the saddle-point electrons and the fast forward electrons, shown in the electron momentum distributions for $\text{He}^{2+} - H_2$ collision system are seen also to emerge for this reaction channel. In contrast to **TI**, while the saddle-point electrons group is shown

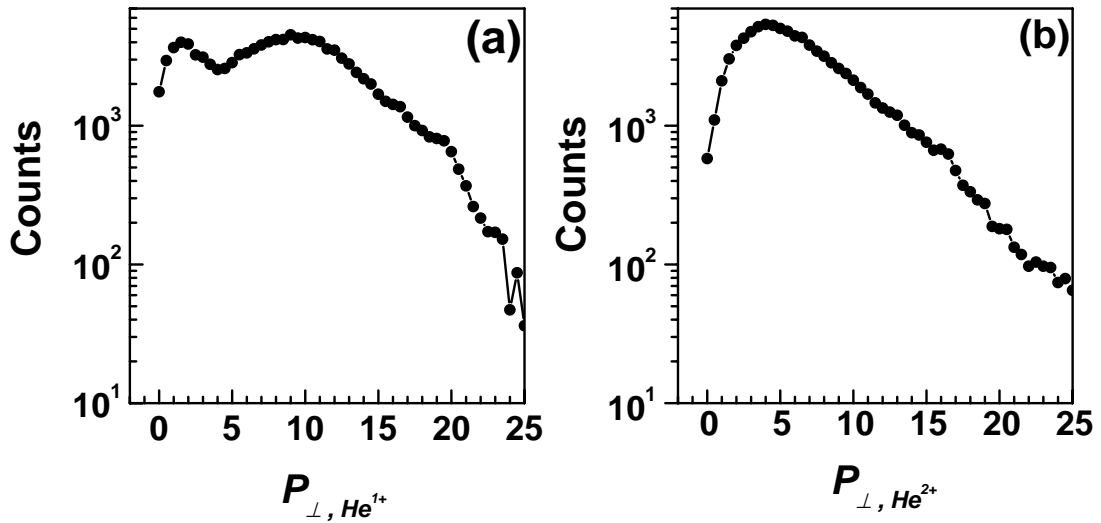


Figure 5.19: (a) Radial transverse momentum distribution of He^{2+} ions in the collision $25\text{ keV } He^{2+}$ on He leading to the transfer-ionization. The distribution is integrated over all azimuthal angles. (b) Radial transverse momentum distribution of He^{1+} ions in the same collision leading to the single ionization.

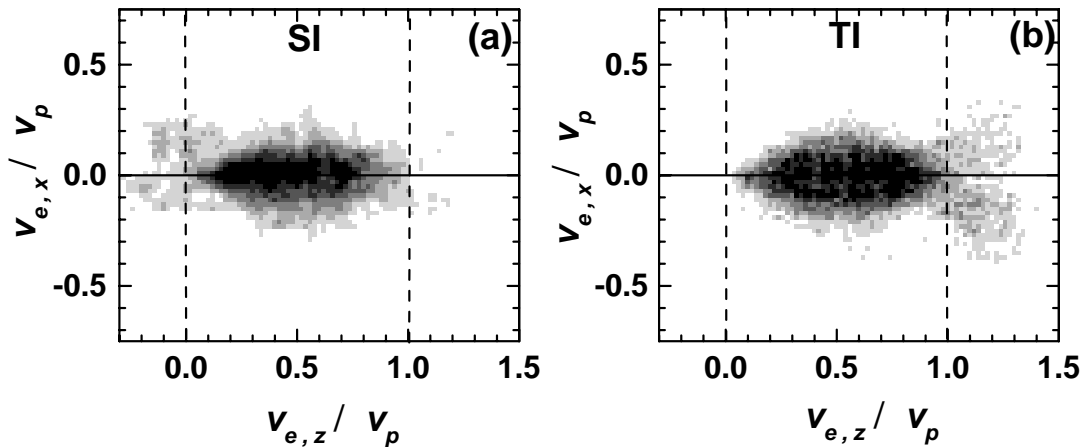


Figure 5.20: (a) Side view of ejected electron momentum distribution in the collision $25\text{ keV } He^{2+} + He$ leading to SI of He . (b) Side view of ejected electron momentum distribution in the same collision leading to TI of He . The electron velocity components $V_{e,x}$ and $V_{e,z}$ are scaled by the projectile velocity (V_p).

in the electron momentum distribution of **SI** (Figs 5.20(a)), the fast forward electrons group disappears in this distribution. However, another group is emerged in the **SI** electron momentum distribution. This group consists of electrons that exhibit a considerable degree of back scattering ($V_{e,z} < 0$). It is referred to as backward

electrons.

Saddle-point electrons

As shown in the side views, the saddle-point electrons are emitted in the forward direction and distributed symmetrically around the internuclear axis. This demonstrates that the electrons prefer to stay in the scattering plane. Electron momentum distributions for top-views for **SI** and **TI** are given in Fig. 5.21(a) and Fig. 5.21(b), respectively. In these figures, the recoil ion is chosen to be ejected in the negative y direction. These figures show that the saddle point electrons in both cases possess the two-fingered structure showing a quasinodal line along the internuclear axis. This structure is similar to that seen for $He^{2+} - H_2$ collision system. This "two-branch" distribution can be seen in a more qualitative way by making a transverse projection of a slice of each two-dimensional distribution near $V_{e,z}/V_p = 0.5$. Such a projection of Fig. 5.21(a) is shown in Fig. 5.22(a). A similar projection of Fig. 5.21(b) is shown in Fig. 5.22(b). In these figures, it is interesting to note that while in **SI** case more electrons are emitted away from the recoil direction, the electrons follow the recoil in **TI** case. A similar kind of structure was reported by Dörner *et al.* [46] for 5, 10, and 15 keV $p + He$. In that work this structure was qualitatively explained in terms of hidden crossing theory. According to this explanation [31, 33], two series of transitions can contribute to the saddle-point ionization mechanism. The first is the so called **T00**-series and involves no angular momentum transfer and thus leads to a σ state with a maximum on the saddle. The second series is **T01**-series which starts with a rotational coupling from $2p\sigma$ to the $2p\pi$ orbital of the quasi-molecule and leads to a π state with a node on the saddle. The two states should add coherently which leads to the observed asymmetry depending on the relative amplitudes of the two states. In this experiment we show that this behavior is not only limited to the atomic targets, but it can be also observed in ion-molecular collision systems.

Fast Forward and Backward Electrons Groups

While the saddle-point electrons are confined to the collision plane, the fast forward electrons in the **TI** case and the backward electrons in the **SI** case exhibit a substantial amount of out-of-plane electron scattering. The backward electrons follow the scattered projectile as shown in Fig. 5.21(a). In contrast, the fast forward electrons are emitted away from the scattered projectile as observed in Fig. 5.21(b). To further explore these electron groups, the two-dimensional electron momentum distributions in Figs 5.21(a) and 5.21(b) are projected on the $V_{e,z}$ axis. The projections are given in Figs 5.23(a) and 5.23(b), respectively. These figures show that, while the fast forward electrons reveal a distinct peak at projectile velocity, the backward electrons possess a broad distribution at the target velocity. In addition, the contribution of the fast forward electrons to the cross section of transfer ionization of He estimated from the momentum distribution is 31.7%. It is observed that this contribution is greater than the contribution of the backward electrons to the cross

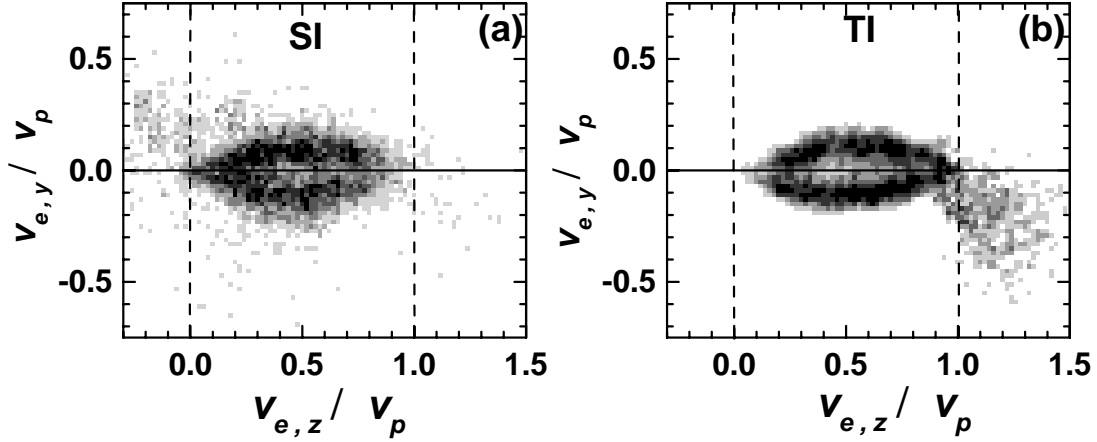


Figure 5.21: Top-view of ejected electron momentum distribution in the collision 25 keV He^{2+} on He (a) leading to **SI** of He and (b) leading to **TI** of He. The electron velocity components $V_{e,y}$ and $V_{e,z}$ are scaled by the projectile velocity V_p .

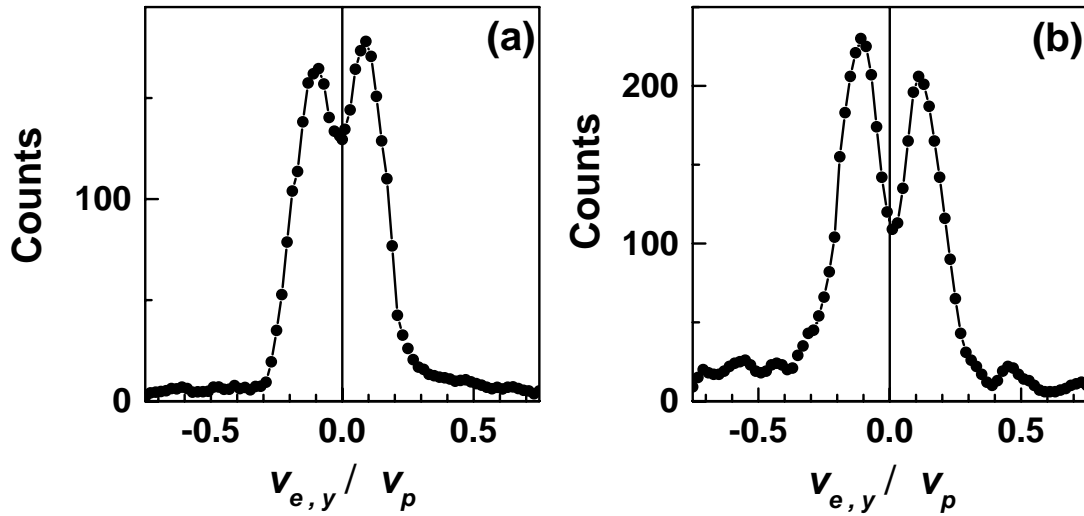


Figure 5.22: Transverse projections of the 2D momentum distributions in 5.21(a) and 5.21(b) near $V_{e,z}/V_p = 0.5$.

section of the single ionization of H_2 which equals 23%.

Impact-Parameter Dependence

To study the impact-parameter dependence of the emitted electron momentum distribution in the scattering plane, the top view of the electron momentum distribution was generated for different windows on the magnitude of the transverse momentum

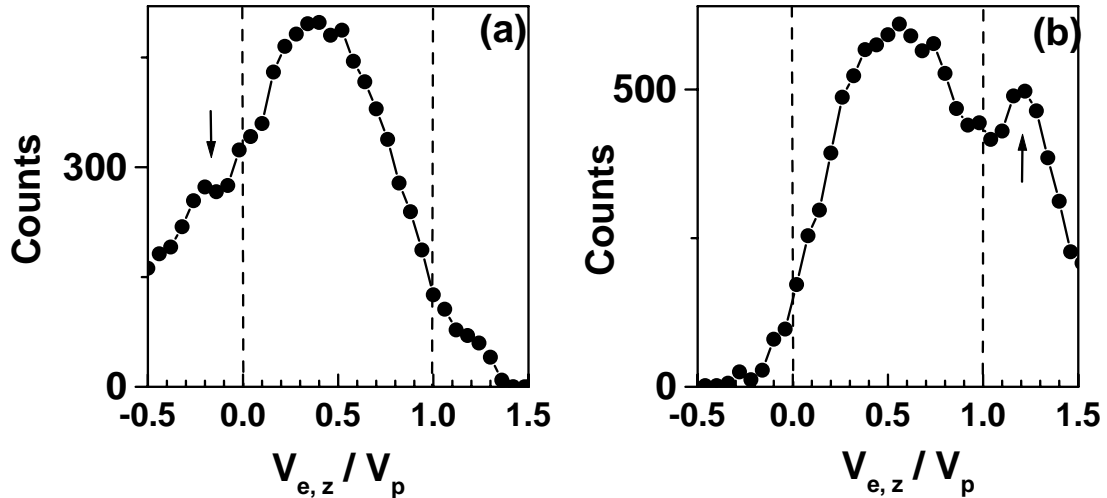


Figure 5.23: Z-component of the velocity of electrons ejected in the collision $25 \text{ keV He}^{2+} + \text{H}_2$ (a) for **SI** and (b) for **TI**. The electron velocity components are scaled by the projectile velocity (V_p). The arrows point to the backward electrons group in (a) and the fast forward electrons group in (b).

transfer, i.e., impact parameter. This was done for both **SI** and **TI** cases. The results are presented in Fig. 5.24 for **SI** and in Fig. 5.26 for **TI**. In Figs. 5.24(a)-(c) of **SI**, the impact parameter decreases from (a) to (c). The corresponding transverse projections of slices from each distribution near $V_{e,z}/V_p = 0.5$ are presented in Figs. 5.25(a)- 5.25(c). The figures show that at large impact parameters the momentum distribution displays a structure which strongly suggests that it is σ state. In this structure, the electrons concentrate on the internuclear axis forming a peak around it as shown in Fig. 5.24(a). At small impact parameters, the two off-axis peaks appear in the momentum distribution. This structure reveals a nodal line along the internuclear axis as seen in Fig. 5.24(c). This nodal line is a signature of the π orbital. The asymmetry in the intensity about this quasinodal line can be interpreted as owing to the interference of the π amplitude with a weaker σ amplitude, which would both produce an asymmetric distribution and weaken the node as seen in Fig. 5.24(b).

The impact parameter dependence of the electron momentum distribution for **TI** is presented in Fig. 5.26. The impact parameter decreases from (a) to (d). The corresponding transverse projections of slices from each distribution near $V_{e,z}/V_p = 0.5$ are given in Figs. 5.27(a)- 5.27(d). The momentum distribution exhibits the two-fingered structure in all ranges of impact parameters. However, the distribution becomes more symmetric at smaller impact parameters (larger recoil-ion transverse momentum). This suggests that the relative contributions of σ and π orbitals depend on the impact parameter. At small impact parameters the π is dominant over σ orbital. This leads to a symmetric distribution around the inter-nuclear axis. At large impact parameters, the σ orbital contribution increases relatively leading to the asymmetry of the distribution.

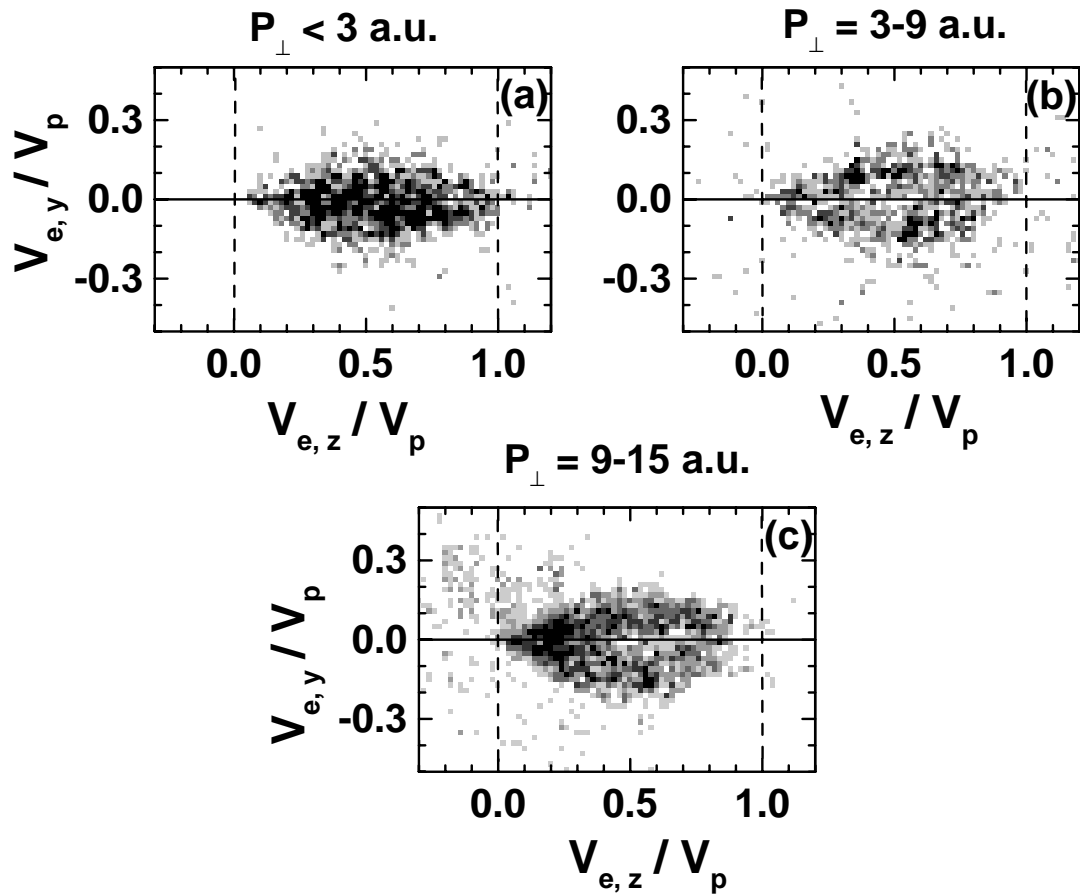


Figure 5.24: Top view of ejected electron momentum distribution for SI in the collision $25 \text{ keV He}^{2+} + \text{He}$ generated for different ranges of impact parameters. The electron velocity components $V_{e,z}$ and $V_{e,y}$ are scaled by the projectile velocity (V_p). The impact parameter decreases in the figures by moving from (a) to (c).

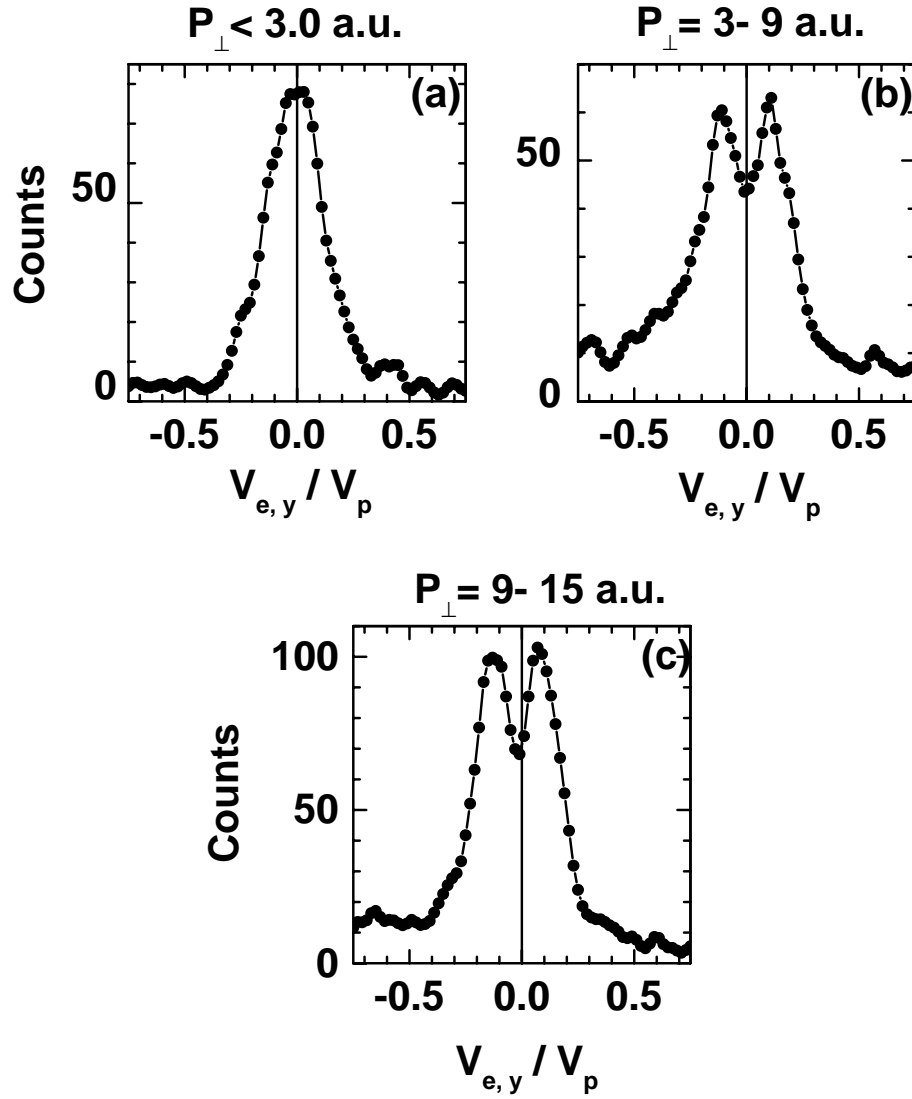


Figure 5.25: Transverse projections of the 2D momentum distributions in Figs. 5.24(a)- 5.24(c) near $V_{e,z}/V_p = 0.5$.

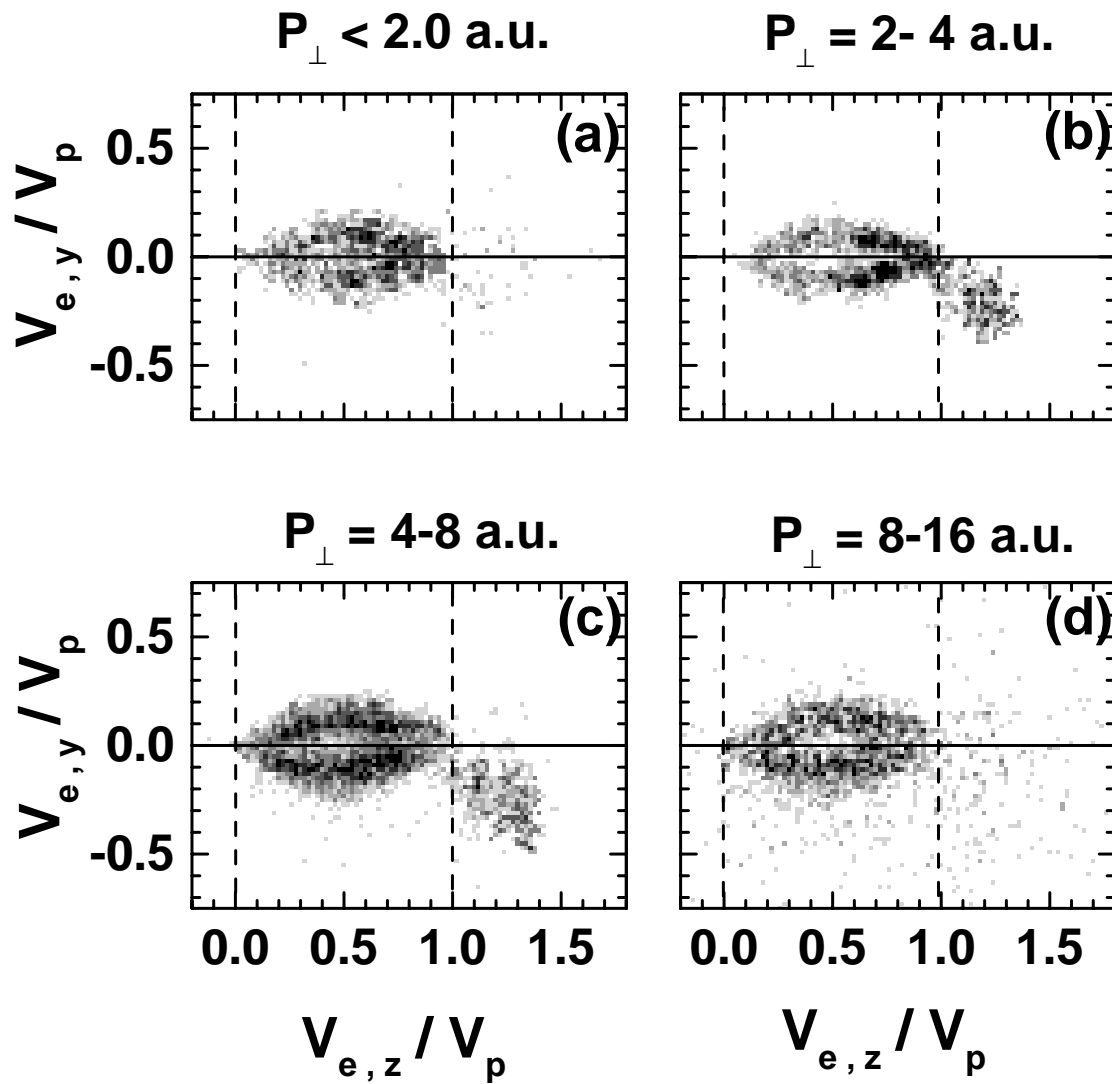


Figure 5.26: Top view of ejected electron momentum distribution in the collision $25 \text{ keV } He^{2+} + He$ leading to **TI** of He generated for different impact parameters. The electron velocity components $V_{e,z}$ and $V_{e,y}$ are scaled by the projectile velocity (V_p). The impact parameter decreases in the figures by moving from (a) to (d).

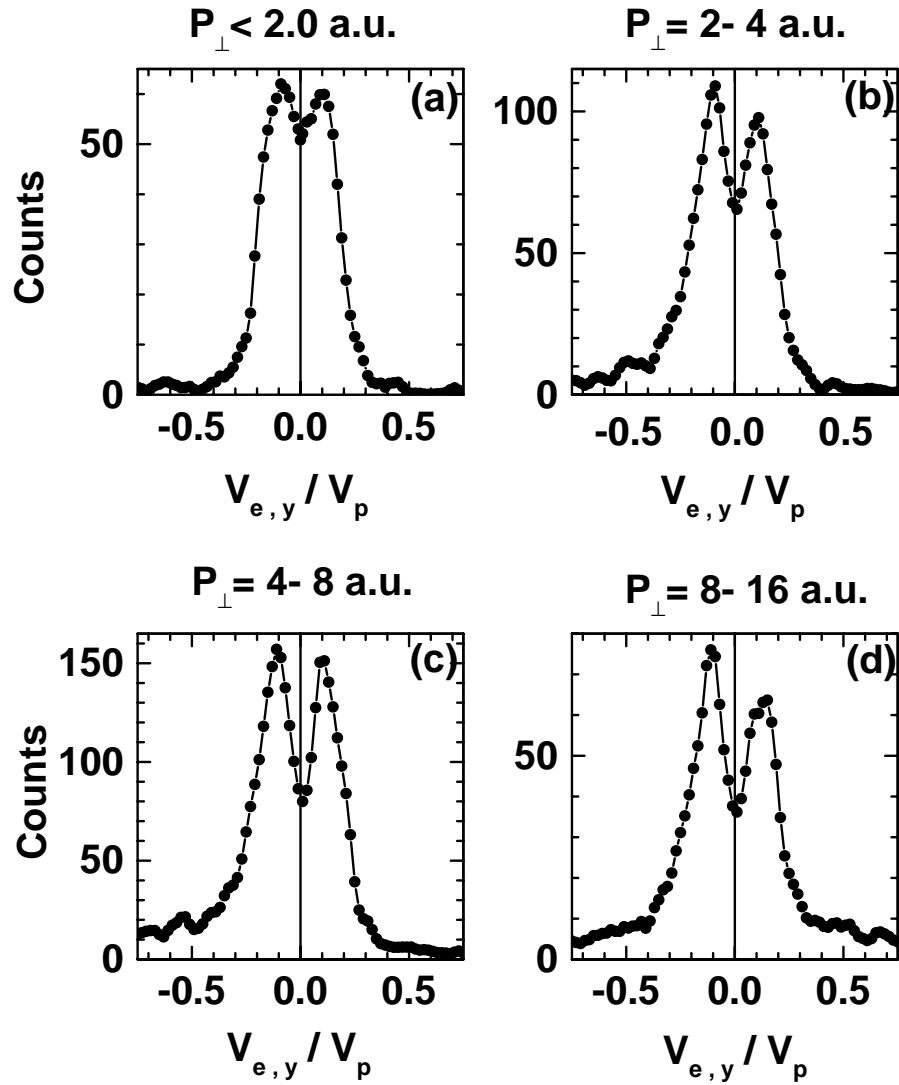


Figure 5.27: Transverse projections of the distributions in Figs. 5.26(a)- 5.26(d) near $V_{e,z}/V_p = 0.5$.

To study the impact parameter dependence of the other two groups, i.e, the backward electrons and the fast forward electrons, the two-dimensional electron momentum distributions are projected onto the $V_{e,z}$ axis for different ranges of impact parameters. The results for **SI** are presented in Figs. 5.28(a)-(c). The figures show that the backward electrons are generated at small impact parameters as seen in Fig 5.28(c). Similar consequences can be observed for the fast forward electrons in **TI** case as appears in Figs. 5.29(a)-(d). These figures display the impact parameter dependence of the fast forward electrons. The figures show that the fast forward electrons result from a narrow range of impact parameters and appear as image saddle in the projectile frame.

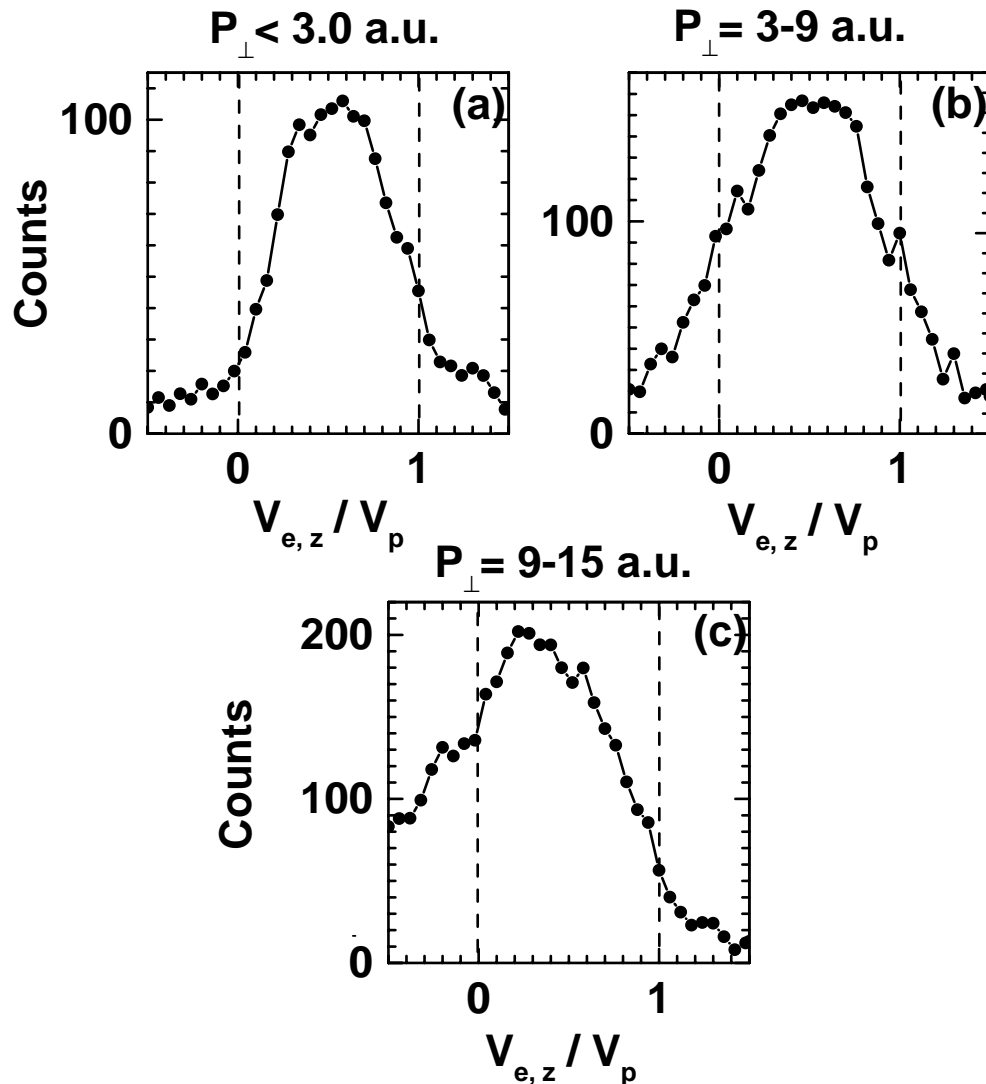


Figure 5.28: Z-component of the velocity of electrons emitted in the single ionization of He by He^{2+} at 25 keV impact energy for different impact parameters.

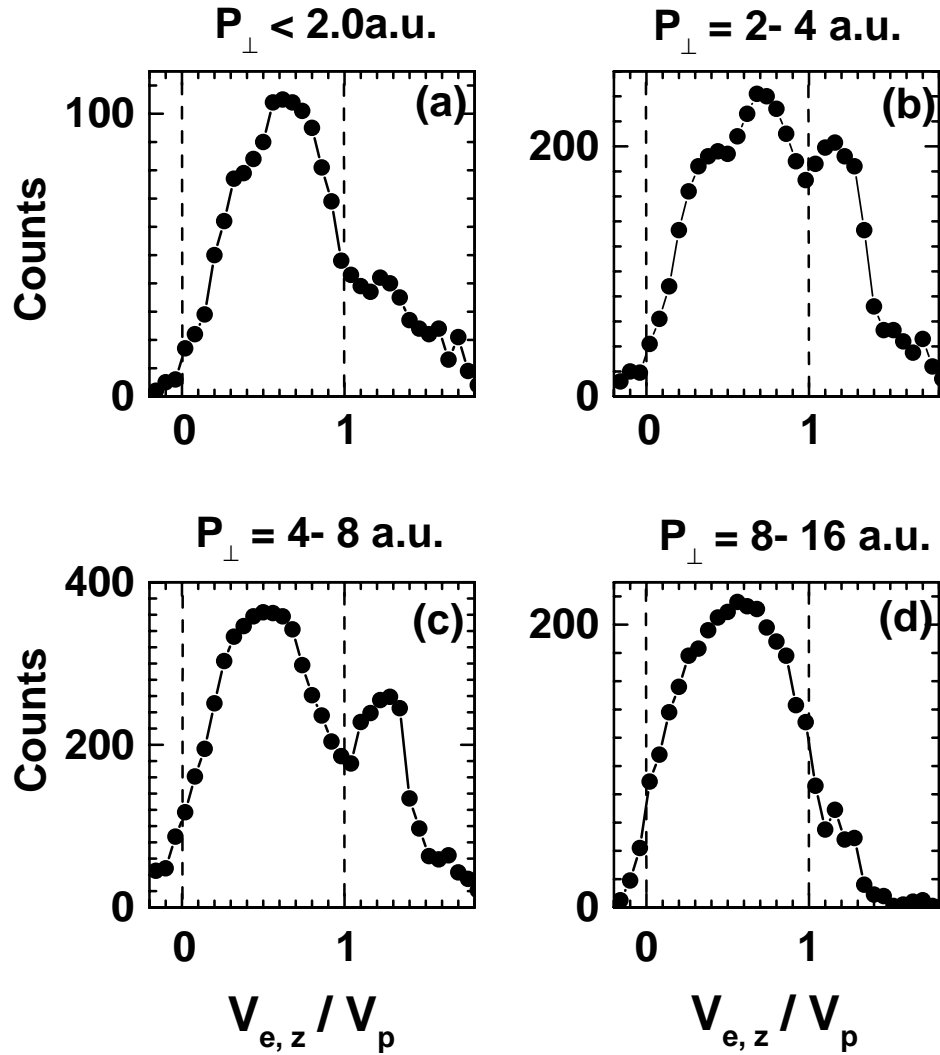


Figure 5.29: Z-component of the velocity of electrons emitted in the transfer ionization of He by He²⁺ at 25 keV impact energy for different impact parameters.

5.2 Discussion and Interpretation

5.2.1 Saddle-point electrons

Since explicit theoretical calculations of the electron momentum distributions as a function of impact parameter have not yet been carried out for the systems investigated in the present work, we can speculate on the major mechanisms which we believe our data reveal. In the saddle point vicinity, two structures have been observed in the measured electron momentum distributions: the maximum on the internuclear axis structure and the two-fingered structure. These structures were interpreted by *Ovichinnikov et al.* [31] and *Macek et al.* [151, 49] within the theory of hidden crossings. The major idea is that one electron (or more) molecular orbital(s) is promoted into the continuum carrying with it the character of that promoted orbital. This character is then revealed in the form of the continuum velocity distribution. Two series of transitions are expected to contribute to the saddle point ionization mechanism. The $T00$ series involves no angular momentum transfer and thus leads to a σ state in the saddle continuum, while the $T01$ series starts with a rotational coupling to the $2p\pi$ orbital of the quasimolecule and leads to a π state. Based on the model suggested by Macek et al. [151], one can write the final electron wave function as a superposition of model σ and π amplitudes. This can be written as

$$\Psi = \alpha|\pi \rangle + \beta e^{i\phi}|\sigma \rangle \quad (5.6)$$

where ϕ is the difference in phase between the two amplitudes and is given by

$$\phi = -Re \int_{t_o}^{\infty} [\epsilon_{\sigma}(R) - \epsilon_{\pi}(R)]dt = -\frac{1}{V_p} Re \int_{R_o}^{\infty} [\epsilon_{\sigma}(R) - \epsilon_{\pi}(R)]dR \quad (5.7)$$

where ϵ_{σ} and ϵ_{π} are the energies of σ and π paths along which the promotion occurs, respectively. t_o and R_o are constants. Fig. 5.30 shows a simple representation of the final electron wave function. In addition, the interference of the π amplitude with σ amplitude which leads to the asymmetry of the electron momentum distribution can also be shown in this figure. It is this different symmetry of σ and π states which, according to the calculations, yields a maximum on the saddle for the $T00$ and a node for the $T01$ series. Such an explanation seems natural for the collision systems studied in this work as well. Therefore, the pattern of double branches, separated by a nodal line, springs from target ionization along a promoted $2p\pi$ molecular orbital. In collisions of He^{2+} with He , the promotion starts via the rotational coupling of the molecular orbital $2p\sigma$ and the molecular orbital $2p\pi$ at small internuclear distances. The $2p\pi$ orbital is then eventually promoted via a series of radial crossings (T -process) into the continuum. This process conserves the π character of the orbital and gives rise to the nodal line along the internuclear axis.

If the above mechanism holds, the impact parameter dependence of the process should be dominated by the enabling rotational coupling process, which transforms

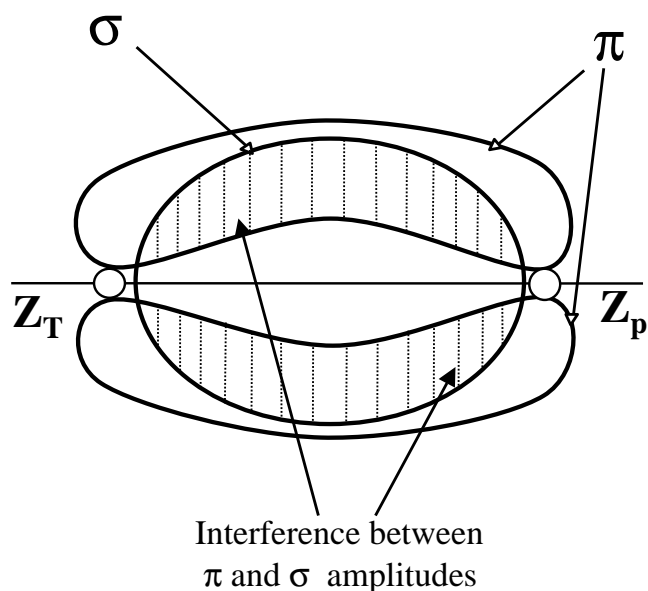


Figure 5.30: A simple representation of the final electron wave function as a superposition of model σ and π amplitudes [151].

the $2p\sigma$ initial orbital into the $2p\pi$ one. The following promotion of the $2p\pi$ orbital into the continuum should subsequently occur at large impact parameters on the way out of the collision. Hence, no strong impact parameter dependence is expected in this second step. This explains the appearance of the two-fingered structure for all ranges of impact parameters in TI reaction as shown in Fig. 5.26. Based on this analogy, we can expect that the probability of the $2p\sigma$ - $2p\pi$ rotational coupling has its maximum at $b=1.23$ a.u. ($P_{\perp} = 4$ a.u.) as determined from the recoil ion transverse momentum distribution shown in Fig. 5.19(b). In contrast to the TI , Both $T00$ and $T01$ transition series can be observed in the electron momentum distributions generated at different impact parameters for SI reaction. At large impact parameters (i.e small transverse momentum transfer), the $T00$ transition series is dominant. This series leads to a maximum on the internuclear as shown in Fig. 5.24(a). At small impact parameters, the $T01$ dominates and leads to the nodal line along the internuclear axis as shown in Fig. 5.24(c). These results agree with that observed in the recoil ion transverse momentum distribution seen in Fig. 5.19(a).

The strong similarity of the electron velocity distributions observed for the helium and the molecular hydrogen target suggests that similar ionization mechanisms are operating for both targets. Since no orientation dependence is observed for the electron momentum distribution for the $He^{2+} - H_2$ collision system, we can expect that the interpretations made for the $He^{2+} - He$ collision system are valid for the $He^{2+} - H_2$ collision system.

5.2.2 Fast Forward Electrons and Backward Electrons

The fast forward electrons measured for the first time in the present work have been overlooked in all experiments so far due to experimental limitations and have not been discussed in the theoretical literature at all. This opens the door to the speculations about the origin of these electrons. An obvious indication of the existence of the fast forward electrons could be seen in the theoretical work of Sidky et al. [169, 3]. They found in classical calculating as well as in using their two center momentum space discretization method (see section 2.2.6) a significant emission of fast forward electrons. Fig. 5.31 shows an example of their calculations. In this Fig. 5.31, the longitudinal electron momentum distributions calculated for the $p-H$ system using the *TCMSD* and *CTMC* methods at impact energies 10, 15, 25, and 50 *keV* and an impact parameter $b= 1.2$ a.u. are presented. The figures show that a number of emitted electrons have a velocity higher than the projectile velocity. To define the ionization more precisely, they have identified the ionized electrons at an internuclear separation of 500 a.u.. The ejected electrons are then propagated backwards to lower internuclear separations to examine the ionization mechanism, specifically, the saddle-point ionization as a function of R . Fig. 5.32 shows a slice of the ejected electron momentum distribution, at $R=30$ for the 15 and 50 *keV* collisions. Each dot, gray or black, represents an electron trajectory that will be in the continuum at $R= 500$. In this figure circles of radius p_{ion} are drawn in about both target and projectile centers. In Fig. 5.32(b), most of the electrons are outside the two circles indicating that electrons which are ejected at $R=500$ a.u. are already in the continuum at $R= 30$ a.u. for collisions at 50 *keV*. In Fig. 5.32(a), there is still a nontrivial fraction of electrons which lies inside the circles. These electrons have $p_{||}$ near $V/2$ as an indication that the potential saddle may play an important role.

To isolate the effect of the saddle potential as the two nuclei recede from each other, they classified the ejected electrons for $t>0$ into two groups at each z , where $z = vt$: (1) "kinetic" electrons- energy is positive with respect to both target and projectile protons, individually, and (2) saddle point electrons- energy is negative with respect to either proton. The kinetic electrons represent any electron that is considered ejected at the current z , and they are represented by gray dots in Fig. 5.32. The saddle point electrons are not free at the current z and require the long-range two-centre interaction to reach the continuum. These electrons are represented by the black dots in the figure. Clearly, this definition includes electrons promoted into the continuum on the internuclear potential saddle and from Fig.5.32(a) these electrons are mostly located near the potential saddle.

Following these definitions, they have evaluated the ratio P_s of saddle-point electrons as a function of z as the two nuclei recede for 5,10,15, and 50 KeV; see Fig.5.33. The curves for 5-15keV exhibit similar behavior. The saddle fraction exhibits a plateau after $z=8$, where the top of the barrier is the same as the average energy of the initial state. Subsequently, as the saddle pushes upward, the saddle-point electrons are promoted to the continuum, and thus the saddle-point fraction decreases monotonically. For low energy collisions this process is stretched out since the electrons entering the saddle region have a low kinetic energy with respect to

the saddle point. Fig. 5.33 shows that the saddle-point mechanism contributes a maximum of 33% to the total ionization probability, decreasing slowly from 5 to 15 keV. On the other hand, the range of saddle-point ionization decreases rapidly with impact energy until finally, at 50 keV, the saddle fraction just drops monotonically to zero. From their analysis of the classical calculations, they have concluded that experimental measurement of the $V/2$ peak in the longitudinal momentum distribution of ejected electrons does not necessarily imply the saddle point mechanism.

Another theoretical model which can be employed in our discussion is the Zero-Ranged Potential Model (see 2.5 for more details). The electron momentum distributions calculated by Macek et al. [188] using this model exhibit peaks in the forward and backward directions. They found that these oscillations are owing to interference between the g and u amplitudes. They have attributed these peaks classically to Fermi acceleration (for more details, see section 2.5).

While the fast forward electrons are observed for the TI of He by He^{2+} , a related feature was noted in the electron momentum distribution measured for the SI of He by He^{2+} . This feature consists in the appearance of backward electrons. A deep comparison between the fast forward electron group and the backward electrons group shows that the electrons in both groups are emitted in the same direction of the He^+ ions in longitudinal direction and in the opposite direction of the He^+ ions in the transverse direction. Based on this comparison, one might speculate that the electrons which are promoted on the saddle for some time during the collision could finally swing around the He^+ ion in the way out of the collision, i.e, either around the projectile in the forward direction in the TI case forming the fast forward electrons or around the recoil ion in the backward direction in the SI case forming the backward electrons. This might be a result of the strong gradient, and hence the large acceleration of the screened He^+ potential.

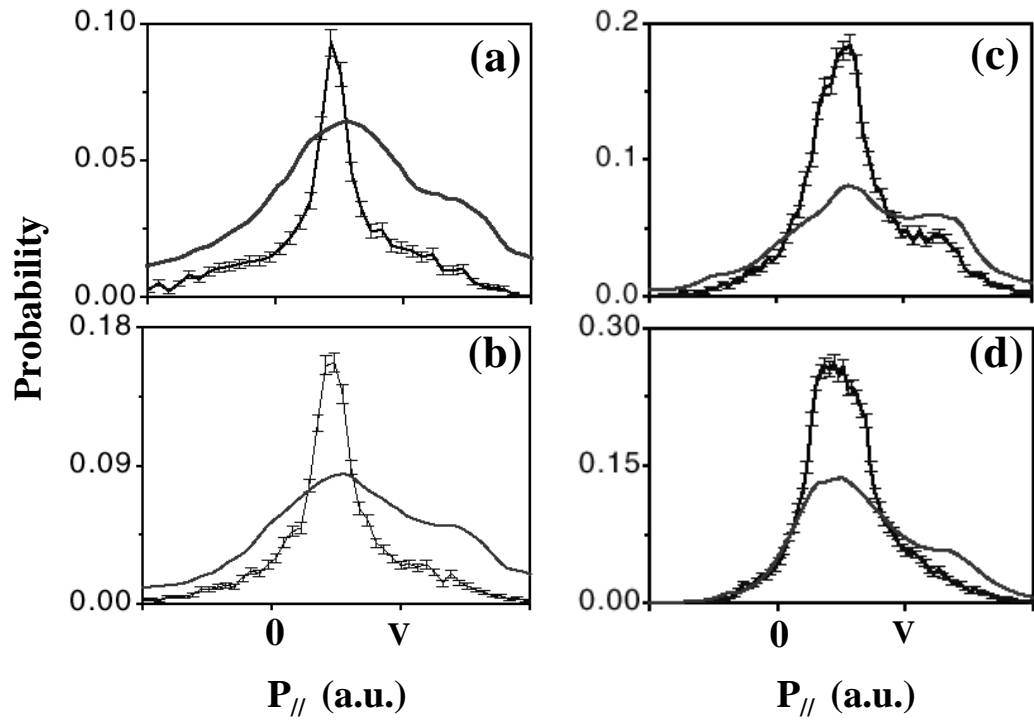


Figure 5.31: Probability distribution of ejected electrons, $P_{||}$ (a.u.) vs. $P_{||}$ (a.u.).

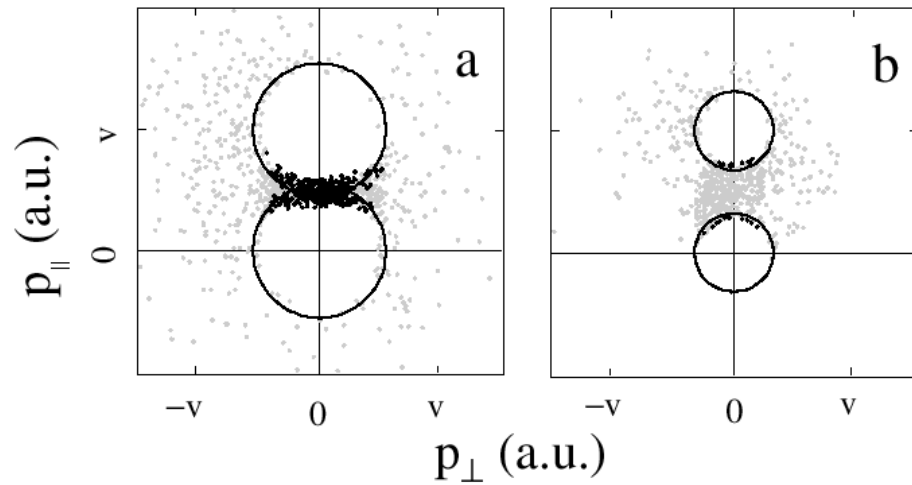


Figure 5.32: Scatter plot of ejected electrons, in momentum space, within 0.1 a.u. of the collision plane. Gray and black dots represent kinetic and saddle electrons, respectively; see text. Circles of radius P_{ion} centered on the target and projectile protons indicate the minimum momentum of ejection based on a free expansion model. (a) 15 keV at $z=30$ a.u. and (b) 50 keV at $z=30$ a.u. (from Sidky et al. [3]).

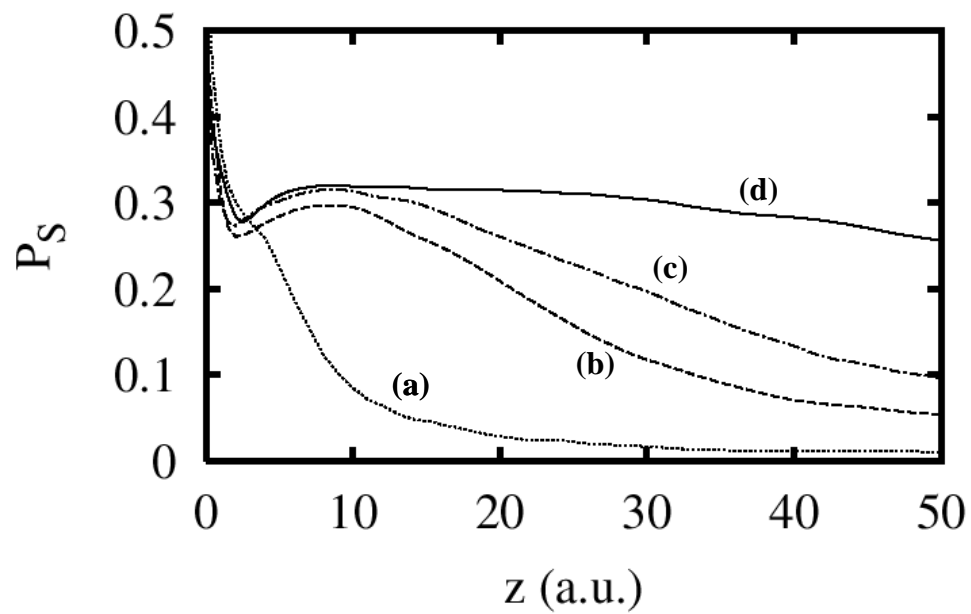


Figure 5.33: Fraction of saddle electrons as a function of z . Curves correspond to impact energies (a) 50 keV, (b) 15 keV, (c) 10 keV and (d) 5 keV (from Sidky et al. [3]).

Chapter 6

Concluding Remarks

The results reported in this thesis were a significant advance in the general comprehending of the ionization processes in the slow ion-atom collisions and in the slow ion-molecule collisions. In general, we employed *COLTRIMS* technique to measure the momentum distribution of emitted electrons for a variety of collision systems, and as the development of our apparatus progressed, we were able to do increasingly detailed measurements. These collision systems studied in this work can be classified as ion-atomic collision systems (He^{2+} on He) and ion-molecular collision systems (He^{2+} on H_2).

In ion-atom collisions, the results presented in this work revealed the appearance of new structures in the ejected electron momentum distributions. In addition to the well-known saddle electrons, the backward electrons and the fast forward electrons appeared. These backward and fast forward electrons have been overlooked in all previous experiments so far owing to experimental limitation and are not discussed in the theoretical literature at all. Side-views of the electron momentum distributions generated for the ion-atom collisions showed that the saddle electrons are emitted in the forward direction and confined to the scattering plane. In contrast, the momentum distributions showed that both backward and fast forward electrons exhibit a degree of out-of-plane scattering.

The in-scattering-plane electron momentum distributions showed that the saddle electrons are emitted in two jets oriented in the scattering plane in the forward direction and off the projectile-axis. This structure is attributed to the promotion of molecular orbitals of π character into the continuum. These results revealed the importance of the quasi-molecular nature of the ionization process. Regarding the backward and fast forward electrons, the in-scattering-plane distributions showed that both groups exhibit a different structure than that of the saddle electrons. The fast forward electrons are ejected in the forward direction with a velocity greater than the projectile velocity and scattered opposite to the scattered projectile. In contrast, the backward electrons are emitted in the backward direction and scattered in the same direction of the scattered projectile.

In ion-molecule collision systems studied in this work, two of the three electrons groups shown in the ion-atom collisions were obtained for the ion-molecule collisions.

They are the saddle electrons group and the fast forward electrons group. The orientation dependence of the electron momentum distribution was studied. The results show no influence of the molecular orientation on the electron momentum distributions. These results represent the first experimental study of the orientation dependence of the continuum electron momentum distribution for a molecular target.

The comparison of the results obtained for H_2 with the results of Helium, the corresponding atomic two-electron system, offered the suitable basis of the interpretation process of the results determined for the H_2 because no orientation dependence of the electron momentum distributions was observed. The comparison showed that the two-fingered structure was appeared for both targets in the saddle vicinity. Concerning the fast forward electrons, the comparison showed that these electrons yielded a significant contribution to total cross-section of the transfer ionization process for both targets. They contributed up to 40.5% to the cross section of the transfer ionization of H_2 . This contribution was greater than the contribution of these electrons to the cross section of the transfer ionization of He which equals 31.7%.

Finally, the impact-parameter dependence of the electron momentum distributions for both kinds of collision systems was investigated. It was observed, in the case of TI of He by He^{2+} , that the two-fingered structure appeared in the saddle vicinity for all ranges of impact parameters. However, at small impact parameters, the momentum distribution became more symmetric around the internuclear axis because of the dominance of π orbital over σ orbital. In the TI of H_2 by He^{2+} , the two fingered structure was seen to appear at small impact parameters. At large impact parameters, the σ orbital contribution increases relatively leading to the asymmetry of the distribution around the internuclear axis. In contrast, the σ orbital was the dominant orbital over all ranges of impact parameters in the case of the SI of H_2 by He^{2+} . In the case of the SI of He by He^{2+} , the two-fingered structure was seen only at a small impact parameters. At large impact parameters a maximum in the saddle was obtained which indicated that the σ orbital was dominant over the π -orbital. The study of the impact-parameter-dependence of the fast forward electrons displayed that these electrons raised from a narrow range of impact parameters and appeared as image saddle in the projectile frame. In the backward electrons case, the study of impact parameter dependence showed that these electrons resulted also from a small range of impact parameters but they appeared as image saddle in the target frame.

Appendix A

Multi-Hit Lecroy 3377 TDC

The 3377-TDC has four separate operating modes. The times are measured with respect to a common hit, which can occur before or after the individual time signal to be measured (common stop or common start mode). The other mode dependent feature is the data format, which can be either single or double word. A summary of the modes is listed below

Mode	Operation	Data Format
0	Common Stop	Single Word
1	Common Start	Single Word
2	Common Stop	Double Word
3	Common Start	Double Word

Table A.1: Operation modes of 3377-TDC

In the present work, the common-stop double-word mode was chosen in the measuring process. In this mode, the output data is in double word format. It consists of a header word, followed by up to 1024 data words. The double-word format can be represented as follows

Header

- bits 0-7 the 8 bit module ID bits
- bits 8-9 the 2 bit resolution value, always 0
- bit 10 the rising/both edge recording
- bit 14 the event serial number
- bit 15 the event serial number

First Data Word

- bits 0-7 8 bit data value

bit 8 1, indicates that the data is the most significant byte
bit 9 identifies the edge, 0= rising, 1= falling
bits 10-14 5 bit channel no.
bit 15 always 0, identifies data word

Second Data Word

bits 0-7 8 bit data value
bit 8 0, indicates that the data is the least significant byte
bit 9 identifies the edge, 0= rising, 1= falling
bits 10-14 5 bit channel no.
bit 15 always 0

The output data includes in addition to the physical information technical information. Therefore, one needs to write a small program to extract the physical information and eliminate the technical information. The following program is written in Fortran language to extract the physical information from the output data for an event consisting of one measured quantity:

```

real*8 ED(1),ED(2),ED(3),ED(4) !! ED(1) is the Header Data
                                !! ED(2) is the First word
                                !! ED(3) is the Second word
                                !! ED(4) is the extracted
                                !! physical information
real*8 CN,CN1,CN2               !! CN is the used channel-TDC no.
                                !! CN1 is the channel no. obtained
                                !! from first word (10-14 bits)
                                !! CN2 is the channel no. obtained
                                !! from second word (10-14 bits)
CN1=mod(ED(2)/1024,32)         !! calculate channel no. from first
                                !! word
CN2=mod(ED(3)/1024,32)         !! calculate channel no. from second
                                !! word

IF(CN1==CN2) then
CN=CN1
ED(4)=mod(ED(2),256.)*256.+mod(ED(3),256.)
Else
Endif

```

Bibliography

- [1] M. Abdallah, C. Cocke, W. Wolff, H. Wolf, S. Kravis, M. Stöckli, and E. Kamber, *Phys. Rev. Lett.* **81**, 3627 (1998).
- [2] M. Abdallah, W. Wolff, H. Wolf, C. Cocke, and M. Stöckli, *Phys. Rev. A* **58**, R3379 (1998).
- [3] E. Y. Sidky, C. Illescas, and C. Lin, *Phys. Rev. Lett.* **85**, 1634 (2000).
- [4] A. Dargarno and S. Lepp, in *"Atomic, Molecular, and Optical Physics Handbook"*, edited by G. W. F. Drake (American Institute of Physics, Woodbury, New York, 1996), p. 919.
- [5] R. K. Janev, in *"Review of Fundamental Processes and Applications of Atoms and Ions"*, edited by C. D. Lin (World Scientific, Singapore, 1993), p. 1.
- [6] J. Weisheit, in *Atomic, Molecular, and Optical Physics Handbook*, edited by G. W. F. Drake (American Institute of Physics, Woodbury, New York, 1996), p. 978.
- [7] J. Burgdörfer, in *"Review of Fundamental Processes and Applications of Atoms and Ions"*, edited by C. D. Lin (World Scientific, Singapore, 1993), p. 517.
- [8] E. T. Jensen, in *"Atomic, Molecular, and Optical Physics Handbook"*, edited by G. W. F. Drake (American Institute of Physics, Woodbury, New York, 1996), p. 1007.
- [9] H. Bichsel, in *"Atomic, Molecular, and Optical Physics Handbook"*, edited by G. W. F. Drake (American Institute of Physics, Woodbury, New York, 1996), p. 1032.
- [10] E. Nikitin and S. Umanskii, *Theory of Slow Atomic Collisions* (Springer-Verlag, Berlin, 1984).
- [11] U. Fano and W. Lichten, *Phys. Rev. Lett.* **14**, 627 (1965).
- [12] W. Lichten, *Phys. Rev.* **164**, 131 (1967).
- [13] J. Brenot, J. Pommier, D. Dhuicq, and M. Barat, *J. Phys. B* **8**, 448 (1975).
- [14] J. Brenot, D. Dhuicq, J. Gauyacq, J. Pommier, V. Sidis, M. Barat, and E. Pollack, *Phys. Rev. A* **11**, 1245 (1975).

- [15] M. Barat, D. Dhuicq, R. Francois, C. Lesech, and R. McCarroll, *J. Phys. B* **6**, 1206 (1973).
- [16] G. Gerber, A. Niehaus, and B. Steffan, *J. Phys. B* **6**, 1836 (1973).
- [17] M. Barat, D. Dhuicq, R. Francois, R. McCarroll, R. D. Piacentini, and A. Slain, *J. Phys. B* **5**, 1343 (1972).
- [18] R. McCarroll and R. D. Piacentini, *J. Phys. B* **4**, 1026 (1971).
- [19] V. Sidis, *J. Phys. B* **6**, 1188 (1971).
- [20] W. Meckbach, P. Focke, A. Goni, S. Suarez, J. Macek, and M. Menendez, *Phys. Rev. Lett.* **57**, 1587 (1986).
- [21] C. Reinhold and R. Olson, *Phys. Rev. A* **39**, 3861 (1989).
- [22] G. Bernardi, S. Suarez, P. Fainstein, C. Garibotti, W. Meckbach, and P. Focke, *Phys. Rev. A* **40**, 6863 (1989).
- [23] P. Fainstein, V. Ponce, and R. Rivarola, *J. Phys. B* **24**, 3091 (1991).
- [24] Y. Wang, V. Rodriguez, C. Lin, C. Cocke, S. Kravis, M. Abdallah, and R. D. rner, *Phys. Rev. A* **53**, 3278 (1995).
- [25] R. E. Olson, *Phys. Rev. A* **27**, 1871 (1983).
- [26] R. E. Olson, *Phys. Rev. A* **33**, 4397 (1986).
- [27] R. E. Olson, T. Gay, H. Berry, E. Hale, and V. Irby, *Phys. Rev. Lett.* **59**, 36 (1987).
- [28] T. Winter and C. Lin, *Phys. Rev. A* **29**, 3071 (1984).
- [29] W. Fite, R. Stebbings, D. Hummer, and R. Brack-mann, *Phys. Rev.* **119**, 663 (1960).
- [30] J. Macek and S. Ovchinnikov, *Phys. Rev. A* **50**, 468 (1994).
- [31] S. Ovchinnikov and J. Macek, *Phys. Rev. Lett.* **75**, 2474 (1995).
- [32] M. Pieksma and S. Ovchinnikov, *J. Phys. B* **25**, L373 (1992).
- [33] M. Pieksma and S. Ovchinnikov, *J. Phys. B* **27**, 4573 (1994).
- [34] E. Solovev, *Phys. Rev. A* **42**, 1331 (1990).
- [35] Bárány and S. Ovchinnikov, *Physica Scripta* **T46**, 243 (1993).
- [36] M. Pieksma, S. Ovchinnikov, J. van Eck, W. Westerveld, and A. Niehaus, *Phys. Rev. Lett.* **73**, 46 (1994).

- [37] V. Irby, T. Gay, J. Edwards, E. Hale, M. McKenzie, and R. Olson, *Phys. Rev. A* **37**, 3612 (1988).
- [38] V. Irby, S. Datz, P. Dittner, N. Jones, H. Krause, and C. Vane, *Phys. Rev. A* **47**, 2957 (1993).
- [39] T. Gay, M. Gealy, and M. Rudd, *J. Phys. B* **23**, L823 (1990).
- [40] G. Bernardi, S. Suarez, P. Fainstein, C. Garibotti, W. Meckbach, and P. Fock, *J. Phys. B* **23**, L829 (1990).
- [41] G. Bernardi, P. Fainstein, C. Garibotti, and S. Suarez, *J. Phys. B* **23**, L139 (1990).
- [42] W. Meckbach, S. Suarez, P. Focke, and G. Bernardi, *J. Phys. B* **24**, 3763 (1991).
- [43] R. DuBois, *Phys. Rev. A* **48**, 1123 (1993).
- [44] R. DuBois, *Phys. Rev. A* **50**, 364 (1994).
- [45] S. Kravis, M. Abdallah, C. Cocke, C. Lin, M. Stöckli, B. Walch, Y. Wang, R. Olson, V. Rodriguez, W. Wu, M. Pieksma, and N. Watanabe, *Phys. Rev. A* **54**, 1394 (1996).
- [46] R. Dörner, H. Khemliche, M. Prior, C. Cocke, J. Gary, R. Olson, V. Mergel, J. Ullrich, and H. Schmidt-Böcking, *Phys. Rev. Lett.* **77**, 4520 (1996).
- [47] J. Ullrich, R. Dörner, V. Mergel, O. Jagutzki, L. Spielberger, and H. Schmidt-Böcking, *Comments At. Mol. Phys.* **30**, 285 (1994).
- [48] R. Moshhammer, M. Unverzagt, W. Schmitt, J. Ullrich, and H. Schmidt-Böcking, *Nucl. Instr. Meth. B* **108**, 425 (1996).
- [49] J. Macek and S. Ovchinnikov, *Phys. Rev. Lett.* **80**, 2298 (1998).
- [50] M. Abdallah, S. Kravis, C. Cocke, Y. Wang, V. Rodriguez, and M. Stöckli, *Phys. Rev. A* **56**, 2000 (1997).
- [51] L. Schmidt, Ph.D. thesis, Universität Frankfurt/Main, 2000.
- [52] L. Meng, R. Olson, H. Folkerts, and R. Hoekstra, *J. Phys. B* **27**, 2269 (1994).
- [53] W. Graham, C. Latimer, R. Browning, and H. Gilbody, *J. Phys. B* **7**, L405 (1974).
- [54] C. Can, T. Gray, S. Varghese, J. Hall, and L. Tunnel, *J. Phys. B* **31**, 72 (1984).
- [55] S. Kravis, H. Saitoh, K. Soejima, M. Kimura, I. Shimamura, Y. Awaya, Y. Kaneko, M. Oura, and N. Shimakura, *Phys. Rev. A* **52**, 1206 (1995).
- [56] L. Errea, J. Gorfinkel, A. Macias, L. Mendez, and A. Riera, *J. Phys. B* **30**, 3855 (1997).

- [57] C. Wood and R. Olson, Phys. Rev. A **59**, 1317 (1998).
- [58] H. Mathur, Physics Reports **225**, 193 (1993).
- [59] O. Orient and S. Srivastava, J. Phys. B **20**, 3924 (1986).
- [60] R. Wood, A. Edwards, M. Steuer, M. Monce, and A. Shah, J. Chem. Phys. **73**, 3709 (1980).
- [61] B. Lindsay, F. Yousif, F. Simpson, and C. Latimer, J. Phys. B **20**, 2759 (1987).
- [62] S. Cheng, C. Cocke, Frohne, E. Kamber, J. McGuire, and Y. Wang, Phys. Rev. A **47**, 3923 (1993).
- [63] I. Ben-Itzhak, S. Ginther, and K. Carnes, Phys. Rev. A **47**, 2827 (1993).
- [64] G. Sampoll, R. Watson, O. Heber, V. Horvat, K. Wohrer, and M. Chabot, Phys. Rev. A **45**, 2903 (1992).
- [65] C. Caraby, L. Adoui, J. Grandin, and A. Cassimi, Eur. Phys. J. D **2**, 53 (1999).
- [66] L. Adoui, J. Grandin, A. Cassimi, D. Lelievre, J. Gardin, and A. DuBois, J. Phys. B **32**, 631 (1999).
- [67] A. Golovin, F. Heiser, C. Quayle, P. Morin, M. Simon, P. Guyon, and Becker, Phys. Rev. Lett. **79**, 4554 (1997).
- [68] T. Tuan and E. Gerjuoy, Phys. Rev. **117**, 756 (1960).
- [69] S. Corchs, H. Busnengo, R. Rivarola, and J. McGuire, Nucl. Instr. Meth. B **117**, 41 (1996).
- [70] S. Cheng, C. Cocke, Frohne, E. Kamber, and S. Varghese, Nucl. Instr. Meth. B **56/57**, 78 (1991).
- [71] R. Ezel, A. Edwards, R. Wood, M. Dittmann, J. Browning, and M. Magnan, Nucl. Instr. Meth. B **56/57**, 292 (1991).
- [72] A. Edwards, R. Wood, M. Magnan, and R. Ezell, Phys. Rev. A **46**, 6970 (1992).
- [73] Y. Wang and J. McGuire, Phys. Rev. A **44**, 367 (1991).
- [74] R. Dörner, H. Bräuning, O. Jagutzki, V. Mergel, M. Achler, R. Moshhammer, J. Feagin, T. Osipov, A. Bräuning-Demian, L. Spielberger, J. McGuire, M. H. Prior, N. Berrah, J. Bozek, C. L. Cocke, and H. Schmidt-Böcking, Phys. Rev. Lett. **81**, 5776 (1998).
- [75] M. Kimura, Phys. Rev. A **32**, 802 (1985).
- [76] M. Kimura, S. Chapman, and N. Lane, Phys. Rev. A **33**, 1619 (1986).
- [77] D. Sural and N. Sil, J. Chem. Phys. **42**, 729 (1965).

- [78] V. Sidis and D. de Bruijn, *J. Chem. Phys.* **85**, 201 (1984).
- [79] F. Ellison, *J. Am. Chem. Soc.* **85**, 3540 (1963).
- [80] J. Tully, *J. Chem. Phys.* **58**, 1396 (1973; **59**, 5122, (1973)).
- [81] H. Brinkman and H. Kramers, *Proc. Acad. Sci. Amsterdam* **33**, 973 (1930).
- [82] N. Deb, A. Jain, and J. McGuire, *Phys. Rev. A* **38**, 3769 (1988).
- [83] Y. Band, *J. Phys. B* **15**, 2055 (1974).
- [84] P. Ray and B. Saha, *Phys. Rev. A* **23**, 1807 (1981).
- [85] L. Meng, C. Reinhold, and R. Olson, *Phys. Rev. A* **40**, 3637 (1989).
- [86] L. Meng, C. Reinhold, and R. Olson, *Phys. Rev. A* **42**, 5286 (1990).
- [87] E. Everhart and Q. Kessel, *Phys. Rev. Lett.* **14**, 247 (1965).
- [88] Q. Kessel and E. Everhart, *Phys. Rev. A* **146**, 16 (1966).
- [89] L. Puckett and D. Martin, *Phys. Rev. A* **5**, 1432 (1976).
- [90] J. McConkey, A. Crowe, and M. Hender, *Phys. Rev. Lett.* **29**, 1 (1972).
- [91] W. Steckelmacher, R. Strong, and M. Lucas, *J. Phys. B* **11**, 1553 (1978).
- [92] J. Levin, R. Short, S. Elston, J. Gibbons, I. Sellin, and H. Schmidt-Böcking, *Phys. Rev. A* **36**, 1649 (1987).
- [93] R. Olson, J. Ullrich, and H. Schmidt-Böcking, *J. Phys. B* **20**, L809 (1987).
- [94] J. Grandin, D. Hennecart, X. Husson, D. Lecler, I. Lesteven-Vaisse, and D. Lisfi, *Euro. Phys. Lett.* **6**, 683 (1988).
- [95] J. Ullrich, Ph.D. thesis, Universität Frankfurt/Main, 1987.
- [96] J. Ullrich and H. Schmidt-Böcking, *Phys. Lett. A* **125**, 193 (1987).
- [97] J. Ullrich, H. Schmidt-Böcking, and C. Kelbch, *Nucl. Instr. Meth. A* **268**, 216 (1988).
- [98] R. Dörner, J. Ullrich, H. Schmidt-Böcking, and R. E. Olson, *J. Phys. B* **28**, 435 (1995).
- [99] J. Ullrich, R. Dörner, S. Lencinas, , O. Jagutzki, and H. Schmidt-Böcking, *Nucl. Instr. Meth. B* **61**, 415 (1991).
- [100] R. ALi, V. Frohne, C. Cock, M. Stöckli, S. Cheng, and L. Raphaelian, *Phys. Rev. Lett.* **69**, 2491 (1992).
- [101] V. Frohne, M. Cheng, R. ALi, L. Raphaelian, C. Cock, and R. Olson, *Phys. Rev. Lett.* **71**, 696 (1993).

- [102] V. Frohne, M. Cheng, R. ALi, M. Raphaelian, C. Cock, and R. Olson, *Phys. Rev. A* **53**, 2407 (1996).
- [103] O. Jagutzki, Ph.D. thesis, Universität Frankfurt/Main, 1995.
- [104] E. Forberich, R. Dörner, J. Ullrich, R. Olson, K. Ullmann, A. Gensmantel, S. Lencinas, O. Jagutzki, and H. Schmidt-Böcking, *J. Phys. B* **24**, 3613 (1991).
- [105] S. Lencinas, J. Ullrich, R. Dörner, R. Olson, W. Wolff, H. Wolff, L. Spielberger, S. H. M. Horbatsch, C. Cock, and H. Schmidt-Böcking, *J. Phys. B* **27**, 287 (1994).
- [106] P. Jadrin, A. Cassimi, J. Grandin, H. Rothard, J. Lemoigne, D. Hennecart, X. Husson, and A. Lepontre, *Nucl. Instr. Meth. B* **107**, 41 (1996).
- [107] V. Mergel, Master's thesis, Universität Frankfurt/Main, 1994.
- [108] V. Mergel, R. Dörner, J. Ullrich, O. Jagutzki, S. Lencinas, S. Nüttgens, L. Spielberger, M. Unverzagt, C. Cock, R. Olson, M. Schulz, U. Buck, E. Zanger, W. Theisinger, M. I. S. Geis, and H. Schmidt-Böcking, *Phys. Rev. Lett.* **74**, 2200 (1995).
- [109] V. Mergel, R. Dörner, J. Ullrich, O. Jagutzki, S. Lencinas, S. Nüttgens, L. Spielberger, M. Unverzagt, C. Cock, R. Olson, M. Schulz, and H. Schmidt-Böcking, *Nucl. Instr. Meth. B* **96**, 593 (1995).
- [110] V. Mergel, Ph.D. thesis, Universität Frankfurt/Main, 1996.
- [111] R. Moshhammer, J. Ullrich, M. Unverzagt, W. Schmitt, P. Jardin, R. Olson, R. Mann, R. Dörner, V. Mergel, U. Buck, and H. Schmidt-Böcking, *Phys. Rev. Lett.* **73**, 3371 (1994).
- [112] R. Dörner, V. Mergel, R. Ali, U. Buck, C. Cock, K. Froschauer, O. Jagutzki, S. Lencinas, W. Meyerhof, S. Nüttgens, R. O. H. Schmidt-Böcking, L. Spielberger, K. Tökesi, J. Ullrich, M. Unverzagt, and W. Wu, *Phys. Rev. Lett.* **72**, 3166 (1994).
- [113] W. Wu, K. Wong, R. ALi, C. Cock, V. Frohne, J. Giese, M. Raphaelian, B. Walch, R. Dörner, V. Mergel, H. Schmidt-Böcking, and W. Meyerhof, *Phys. Rev. Lett.* **72**, 3170 (1994).
- [114] W. Wu, J. Giese, Z. Chen, R. ALi, C. Cock, P. Richard, and M. Stöckli, *Phys. Rev. A* **50**, 502 (1994).
- [115] T. Kambara, J. Tang, Y. Awaya, B. DePoaola, O. Jagutzki, Y. Kanai, M. Kimura, T. Kojima, V. Mergel, Y. Nakai, H. Schmidt-Böcking, and I. Shimamura, *J. Phys. B* **28**, 4593 (1995).
- [116] A. Cassimi, S. Duponchel, X. Flechard, P. Jardin, P. Sortais, D. Hennecart, and R. Olson, *Phys. Rev. Lett.* **76**, 3679 (1996).

- [117] L. Spielberger, O. Jagutzki, R. Dörner, J. Ullrich, U. Meyer, V. Mergel, M. Unverzagt, M. Damrau, T. Vogt, I. Ali, K. Khayyat, D. Bahr, H.-G. Schmidt, R. Frahm, and H. Schmidt-Böcking, *Phys. Rev. Lett.* **74**, 4615 (1995).
- [118] L. Spielberger, O. Jagutzki, B. Krässig, U. Meyer, K. Khayyat, V. Mergel, T. Tschentscher, T. Buslaps, H. Bräuning, R. Dörner, T. Vogt, M. Achler, J. Ullrich, D. Gemmell, and H. Schmidt-Böcking, *Phys. Rev. Lett.* **76**, 4685 (1996).
- [119] R. Moshhammer, J. Ullrich, H. Kollmus, W. Schmitt, M. Unverzagt, O. Jagutzki, V. Mergel, and H. Schmidt-Böcking, *Phys. Rev. Lett.* **77**, 1242 (1996).
- [120] M. Schulz, R. Moshhammer, W. Schmitt, H. Kollmus, R. Mann, S. Hagmann, R. Olson, and J. Ullrich, *Phys. Rev. Lett.* **84**, 863 (2000).
- [121] O. Jagutzki, L. Spielberger, R. Dörner, S. Nüttgen, V. Mergel, H. Schmidt-Böcking, J. Ullrich, and R. Olson, *Zeitschrift für Physik* **D36**, 5 (1996).
- [122] R. Dorn, R. Moshhammer, C. Schröter, T. Zouros, W. Schmitt, H. Kollmus, R. Mann, and J. Ullrich, *Phys. Rev. Lett.* **82**, 2496 (1999).
- [123] R. Dörner, J. Feagin, C. L. Cocke, H. Bräuning, O. Jagutzki, M. Jung, E. Kanter, H. Khemliche, S. Kravis, V. Mergel, H. Schmidt-Böcking, J. Ullrich, M. Unverzagt, and T. Vogt, *Phys. Rev. Lett.* **78**, 2031 (1997).
- [124] R. Dörner, T. Vogt, V. Mergel, H. Khemliche, S. Kravis, C. L. Cocke, J. Ullrich, M. Unverzagt, L. Spielberger, M. Damrau, O. Jagutzki, I. Ali, B. Weaver, K. Ullmann, C. Hsu, M. Jung, E. Kanter, B. Sonntag, M. Prior, E. Rotenberg, J. Denlinger, T. Warwick, S. Manson, and H. Schmidt-Böcking, *Phys. Rev. Lett.* **76**, 2654 (1996).
- [125] R. Dörner, H. Bräuning, J. Feagin, V. Mergel, O. Jagutzki, L. Spielberger, T. Vogt, H. Khemliche, M. Prior, J. Ullrich, C. Cocke, and H. Schmidt-Böcking, *Phys. Rev. A* **57**, 1074 (1998).
- [126] H. Bräuning, R. Dörner, C. Cock, M. Prior, B. Krässig, A. Bräuning-Demian, K. Carnes, S. Dreuil, V. M. P. Richard, J. Ullrich, and H. Schmidt-Böcking, *J. Phys. B* **30**, L649 (1997).
- [127] H. Bräuning, R. Dörner, C. Cock, M. Prior, B. Krässig, A. Kheifets, I. Bray, A. Bräuning-Demian, K. Carnes, S. Dreuil, V. M. P. Richard, J. Ullrich, and H. Schmidt-Böcking, *J. Phys. B* **31**, 5149 (1998).
- [128] V. Mergel, M. Achler, R. Dörner, K. Khayyat, T. Kambara, Y. Awaya, V. Zoran, B. Nyström, L. Spielberger, J. McGuire, J. Feagin, J. B. Y. Azuma, and H. Schmidt-Böcking, *Phys. Rev. Lett.* **80**, 5301 (1998).

- [129] L. Spielberger, H. Bräuning, A. Muthig, J. Tang, J. Wang, Y. Qui, R. Dörner, O. Jagutzki, T. Tschentscher, V. Honkimäki, V. Mergel, M. Achler, T. Weber, K. Khayyat, J. Burgdörfer, J. McGuire, and H. Schmidt-Böcking, *Phys. Rev. A* **59**, 371 (1999).
- [130] R. Moshhammer, J. Ullrich, W. Schmitt, H. Kollmus, A. Cassimi, R. Dörner, O. Jagutzki, S. Keller, H. J. Lüdde, R. Mann, V. Mergel, R. Olson, T. Prinz, and H. Schmidt-Böcking, *Phys. Rev. Lett.* **79**, 3621 (1997).
- [131] V. Mergel, R. Dörner, M. Achler, K. Khayyat, S. Lencinas, J. Euler, O. Jagutzki, S. Nüttgens, L. Spielberger, M. Unverzagt, L. Spielberger, W. Wu, R. Ali, J. Ullrich, H. Cederquist, A. Salin, R. Olson, D. Belkić, and H. Schmidt-Böcking, *Phys. Rev. Lett.* **79**, 387 (1997).
- [132] R. Dörner, V. Mergel, O. Jagutzki, L. Spielberger, J. Ullrich, R. Moshhammer, and H. Schmidt-Böcking, *Physics Reports* **330**, 95 (2000).
- [133] R. Zare, *J. Chem. Phys.* **47**, 204 (1967).
- [134] J. Bayfield and G. Khayarallah, *Phys. Rev. A* **11**, 920 (1975).
- [135] R. Abrines and I. Percival, *Proc. Phys. Soc. London* **88**, 861 (1966).
- [136] R. Abrines and I. Percival, *Proc. Phys. Soc. London* **88**, 873 (1966).
- [137] C. Reinhold and R. E. Olson, *Phys. Rev. A* **39**, 3861 (1989).
- [138] H. Folkerts, F. Blied, L. Meng, R. Olson, R. Morgenstern, M. von Hellermann, H. Summers, and R. Hoekstra, *J. Phys. B* **27**, 3475 (1994).
- [139] K. Tökesi and G. Hock, *J. Phys. B* **29**, L119 (1996).
- [140] R. E. Olson, C. Feeler, C. Wood, C. Cocke, R. Dörner, V. Mergel, H. Schmidt-Böcking, R. Moshhammer, and J. Ullrich, *Nucl. Instr. Meth. B* **124**, 249 (1997).
- [141] J. Hansteen and O. Mosebekk, *Phys. Rev. Lett.* **29**, 1361 (1972).
- [142] J. McGuire and L. Weaver, *Phys. Rev. A* **16**, 41 (1977).
- [143] D. Schultz, C. Reinhold, and R. Olson, *Phys. Rev. A* **40**, 4947 (1989).
- [144] V. Montemayor and G. Schiwietz, *Phys. Rev. A* **40**, 6223 (1989).
- [145] C. Cocke and R. Olson, *Physics Reports* **205**, 153 (1991).
- [146] G. Bandarage and R. Parson, *Phys. Rev. A* **41**, 5878 (1990).
- [147] M. Born and J. Oppenheimer, *Ann. Physik* **84**, 457 (1927).
- [148] D. Bates and R. McCarroll, *Proc. R. Soc. A* **245**, 175 (1958).
- [149] M. Kimura and W. Thorson, *Phys. Rev. A* **24**, 1870 (1981).

- [150] J. Houver, J. Phys. B **7**, 1358 (1974).
- [151] J. Macek, Nucl. Instr. Meth. B **124**, 191 (1997).
- [152] E. Solovev, Sov. Phys. Usp. **32**, 228 (1989).
- [153] S. Ovchinnikov and E. Solov'ev, Sov. Phys. JETP **63**, 538 (1986).
- [154] M. Pieksma, Ph.D. thesis, University of Utrecht, 1993.
- [155] V. Maruhn-Rezwani, N. Grun, and W. Scheid, Phys. Rev. Lett. **43**, 512 (1979).
- [156] C. Bottcher, Phys. Rev. Lett. **48**, 85 (1982).
- [157] K. Kulander, K. S. Devi, and S. Koonin, Phys. Rev. A **25**, 2968 (1982).
- [158] C. Bottcher, G. Bottrell, and M. Strayer, Comput. Phys. Commun. **63**, 63 (1991).
- [159] N. Kwong, K. Schaudte, and J. Garcia, Comput. Phys. Commun. **63**, 171 (1991).
- [160] M. Chassid and M. Horbatsch, J. Phys. B **31**, 515 (1998).
- [161] A. Kolakowska, M. Pindzola, F. Roicheaux, D. Schultz, and J. Wells, Phys. Rev. A **58**, 2872 (1998).
- [162] J. Wells, D. Schultz, P. Gavras, and M. Pindzola, Phys. Rev. A **54**, 593 (1996).
- [163] D. Schultz, M. Strayer, and J. Wells, Phys. Rev. Lett. **82**, 3976 (1999).
- [164] K. S. Devi and J. Garcia, J. Phys. B **16**, 2837 (1983).
- [165] W. Stich, J. Lüdde, and R. Dreizler, J. Phys. B **18**, 1195 (1985).
- [166] K. Schaudt, N. Kwong, and J. Garcia, Phys. Rev. A **43**, 2294 (1991).
- [167] E. Y. S. anf C.D. Lin, J. Phys. B **31**, 2949 (1998).
- [168] F. Brau and C. Semay, J. Comput. Phys. **139**, 127 (1998).
- [169] E. S. anf C.D. Lin, Phys. Rev. A **60**, 377 (1999).
- [170] J. Frank, Trans. Farady Soc. **21**, 536 (1925).
- [171] E. Condon, Phys. Rev. **32**, 858 (1928).
- [172] M. Weissbluth, "*Atoms and Molecules*" (Academic Press, New York, 1978).
- [173] A. Coolidge, H. James, and R. Present, J. Chem. Phys. **4**, 193 (1936).
- [174] T. Sharp, At. Data **2**, 119 (1971).
- [175] R. Wood, A. Edwards, and M. Steuer, Phys. Rev. A **15**, 1433 (1977).

- [176] J. Tellinghuisen, in *"Advances in Chemical Physics"*, edited by K. Lawley (Wiley-Interscience, New York, 1985), pp. 229–369.
- [177] R. Zare, *Mol. Photochem.* **4**, 1 (1972).
- [178] J. Dehmer and D. Dill, *Phys. Rev. A* **18**, 164 (1978).
- [179] G. Dunn and L. Kiefer, *Phys. Rev.* **132**, 2109 (1963).
- [180] R. Zare and D. Herschbach, *Proc. IEEE* **51**, 173 (1963).
- [181] R. Schingal and C. Lin, *Phys. Rev. A* **40**, 1302 (1989).
- [182] C. Wood and R. Olson, *Phys. Rev. A* **59**, 1317 (1998).
- [183] G. Herzberg, *"Molecular Spectra and Molecular Structure", I. Spectra of Diatomic Molecules* (Van Nostrand, New York, 1939).
- [184] J. Burgdörfer, J. Wang, and A. Bárány, *Phys. Rev. A* **38**, 4919 (1988).
- [185] J. Wang, J. Burgdörfer, and A. Bárány, *Phys. Rev. A* **43**, 4036 (1991).
- [186] Y. N. Demkov, *"Zero-range Potentials and their Applications in Atomic Physics"* (Plenum, New York, 1988).
- [187] E. Fermi, *Phys. Rev.* **75**, 1169 (1949).
- [188] J. Macek, S. Ovchinnikov, and E. Solov'ev, *Phys. Rev. A* **60**, 1140 (1998).
- [189] K. Stiebing, D. Hofmann, H. Schmidt-Böcking, K. Bethge, H. Streit, A. Schempp, G. Zschornack, and C. Lyneis, *Rev. Sci. Instruments* **63**, 2897 (1992).
- [190] A. Kantrowitz and Grey, *Rev. Sci. Instruments* **22**, 328 (1951).
- [191] D. A. Dahl, *SIMION 3D Version 6.0 User's Manual*, Idaho National Engineering Laboratory, 1995.
- [192] S. Sobottka and M. Williams, *IEEE Trans. Nucl. Sci.* **35**, 348 (1988).
- [193] K. Ullmann-Pfleger, Roentdek G.m.b.H., software@roentdek.com, 1999.

Acknowledgements

First and foremost, I would like to express my thanks to all who have contributed to the success of this work.

I would like to express my deepest gratitude and appreciation to Prof. Dr. Horst Schmidt-Böcking for his supervision, encouragement and guidance throughout all stages of this work. Working with *Horst* made me confident in my abilities and love the experimental research. He is the role model I will endeavour to imitate in my future career. Thanks *Horst*, for quite everything.

My special thanks are extended to Dr. Reinhard Dörner for his precious discussions and continuous advice to overcome many obstacles.

My thanks are due to Dr. Kurt Stiebing for his endurance during the long beamtime hours. I would like also to thank all members of the *ECR* group, especially Lothar Schmidt, for their help in preparing and tuning the *ECR* beam.

My great thanks are for Dr. Ottmar Jagutzki for his assistance in building and operating the detectors. Thanks also go to Dr. Klaus Ullmann-Pfleger for providing help in the laboratory computer network and data acquisition system.

I convey my appreciation to all of my group members who have been generous with encouragement, cooperation, and supportive working atmosphere throughout the work.

Thanks to the accelerator staff for all their help and friendship particularly Herr Schneider who was ready with solutions to a divers of problems. Many thanks also go to the mechanical and electronic workshop crew for their technical support which was important in the success of our experimental work, especially Herr Zanger and Herr Rüschemann. Also, I must give thanks to all members of the *IKF* administration.

In this opportunity I would like to extend my appreciation and thanks to Prof. Dr. K-Ontjes Groeneveld for his profound scientific discussions and his readiness to support me with recommendation letters for the extension of my scholarship.

Special thanks and gratitudes go to the *DAAD* (Deutscher Akademischer Austauschdienst) for their financial support.

I also forward my thanks to Prof. Dr. Stock for my admittance to the *IKF*.

Finally, my thanks go to my parents for their love, support and the faith they raised me on. Everything I accomplished or will accomplish in my life is the fruit

of their work and patience. My deepest thanks and gratitude go to my wife for the cozy atmosphere and continuous love which helped in the success of this work. Thanks to my troubling little daughter for waking up so early to help me go on my data analysis. My thanks are due to my brothers and sisters for their support and love.

CURRICULUM VITAE

Personal Information:

Name : Feras Afaneh
Date and Place of Birth : 22.05.1969 – Tripoli
Marital Status : Married, one Child.

Education:

B.Sc. Physics : University of Jordan, Amman, Jordan, May, 1990.
M.Sc. Physics : University of Jordan, Amman, Jordan, August, 1994.
Thesis title: A Study of The Initial Magnetic Susceptibility of Some Rocks.
Ph.D. : Frankfurt University, Institute of Nuclear Physics, Germany, Since Oct. 1997.

Employment Profile:

10/93 – 3/97 : Teacher for physics, UNRWA- Schools, United Nations, Amman, Jordan.
09/94 – 3/97 : Service Engineer, Electronic Designers Company, Amman, Jordan.
9/91 – 6/94 : Teaching and Research Assistant, Physics Department, University of Jordan, Amman , Jordan.